THESIS FOR THE DEGREE OF DOCTOR OF PHILOSOPHY

FUNCTIONALIZING DNA NANOSTRUCTURES

FROM SURFACE ASSEMBLY TO LIGHT HARVESTING

JAKOB G. WOLLER

Department of Chemical and Biological Engineering

CHALMERS UNIVERSITY OF TECHNOLOGY

Gothenburg, Sweden 2014

Functionalizing DNA Nanostructures

From Surface Assembly to Light Harvesting

Jakob G. Woller

Department of Chemical and Biological Engineering

Chalmers University of Technology

SE-412 96 Gothenburg

Sweden

Telephone +46 (0)31 772 1000

Cover picture:

Examples of functionalized DNA structures used in this thesis. (**Top Left**) DNA origami light harvesting structure, with DNA in gray, light harvesting dyes in green and energy accepting dyes in red. (**Bottom Left**) DNA-porphyrin wire light harvesting structure bound to lipid bilayer, with DNA in black and light harvesting dyes in red. The funnel and arrows represent the migration of excitation energy. (**Top Right**) DNA-bis-porphyrin binding pocket and coordinated ligand. (**Bottom Right**) Hexagonal DNA-porphyrin structure with protruding arms.

FUNCTIONALIZING DNA NANOSTRUCTURES
FROM SURFACE ASSEMBLY TO LIGHT HARVESTING

JAKOB G. WOLLER

Department of Chemical and Biological Engineering

CHALMERS UNIVERSITY OF TECHNOLOGY

Abstract

DNA is emerging as a versatile structural material at the nanoscale due to predictable formation of Watson-Crick base-pairs and the ability to form branched constructs. Using these principles, constructs ranging in size from tens to thousands of base-pairs are routinely formed in solution with predictable structure in two or even three dimensions. Most DNA construction is done in buffered solution where the DNA is in a native state, able to assemble spontaneously and disassemble through external stimuli such as temperature. Here we explore both the reversible formation of DNA functionalized to bind to lipid bilayers and the light harvesting properties of DNA functionalized with light absorbing dyes.

In the first part of this thesis the reversible formation of DNA constructs anchored to lipid bilayers is considered. The anchoring is provided by a covalently attached porphyrin moiety which leaves the DNA in solution while also being in close proximity to the bilayer. We show that this anchoring strategy allows hybridization of an anchored DNA strand in a supported lipid bilayer, at the lipid/aqueous interface, to a strand in solution with 100 % efficiency creating a 39mer duplex. The duplex is readily denatured by heating above its melting temperature, leaving the anchoring strand attached to the bilayer. The reversible assembly of larger DNA constructs consisting of 9 individual strands with a total of 197 base-pairs on liposome surfaces is also studied. Here we show that the reversible assembly depends on the density of DNA structures per liposome and on the total concentration of liposomes in solution. The number of anchoring porphyrins is varied between 1 and 3 per structure revealing that 3 anchor points are necessary to align the construct with a bilayer surface. We show that the diffusion of anchored constructs on supported lipid bilayers depends on the number of porphyrin anchors, with triple anchored constructs showing slowest diffusion. We also show a sequential assembly and disassembly of constructs; one construct can be adsorbed to the bilayer, denatured leaving its anchoring strands in the bilayer, and new constructs can subsequently be formed using the same anchor strands.

In the second part of the thesis photosynthetic light harvesting is mimicked using DNA as a scaffold for placing many small organic dyes. We show that the excitation energy transfer process from a number of donor dyes to a single covalently attached acceptor is efficient and largely dependent on homo-FRET between the donor dyes. By employing large scaffolds consisting of ~7000 base-pairs the excitation of a single acceptor dye attached to the DNA is increased 30 fold due to the presence of the donor dyes. In this case, the absorbing power per acceptor matched natural light harvesting systems grown under high light conditions showing that DNA based systems can potentially reach efficiencies matching those found in nature.

Keywords: DNA Nanotechnology, Membrane Anchoring, Electron Transfer, Light Harvesting, Lipid Bilayer

LIST OF PUBLICATIONS

This thesis is based on the following publications and manuscript, referred to in the text as:

Paper 1

Jakob G. Woller, Karl Börjesson, Sofia Svedhem and Bo Albinsson
Reversible Hybridization of DNA Anchored to a Lipid Membrane via Porphyrin
Langmuir, **2012**, *28* (4), 1944-1953

Paper 2

Karl Börjesson, Erik P. Lundberg, Jakob G. Woller, Bengt Nordén and Bo Albinsson
Soft-Surface DNA Nanotechnology: DNA Constructs Anchored and Aligned to Lipid Membrane
Angew. Chem. Int. Edit., **2011**, *50* (36), 8312-8315

Paper 3

Jakob G. Woller, Jonas K. Hannestad, and Bo Albinsson
Self-Assembled Nanoscale DNA–Porphyrin Complex for Artificial Light Harvesting
JACS, **2013**. *135*(7), p. 2759-2768.

Paper 4

Jakob G. Woller, Mehrnaz Shaali, Patrik G. Johansson, Jonas K. Hannestad, Tom Brown, Aldo Jesorka, and Bo Albinsson
Photonic Islands Assembled from DNA Origami on Nanoscale Teflon AF Patterns
MANUSCRIPT

Paper 5

Karl Börjesson, Jakob G. Woller, Elham Parsa, Jerker Mårtensson and Bo Albinsson
A Bioinspired Self Assembled Dimeric Porphyrin Pocket that Binds Electron Accepting Ligands
Chem. Commun., **2012**, *48* (12), 1793-1795

CONTRIBUTION REPORT

Paper 1

Designed and performed experiments. Performed interpretation and analysis of results. Main author of the paper.

Paper 2

Designed and performed experiments on supported lipid bilayers. Performed interpretation and analysis of these results.

Paper 3

Designed and performed experiments. Performed interpretation and analysis of steady-state fluorescence results. Main author of the paper.

Paper 4

Designed and performed experiments. Performed interpretation and analysis of steady-state fluorescence results. Implemented and analyzed energy transfer simulations. MS fabricated Teflon surfaces. PJ analyzed fluorescence microscopy results. Main author of the paper along with MS.

Paper 5

Performed all experiments. Performed interpretation and analysis of time-resolved fluorescence results. KB analyzed steady-state fluorescence results and wrote the paper.

TABLE OF CONTENTS

1 INTRODUCTION: NANOTECHNOLOGY AND DNA

> *"Nanotechnology is the understanding and control of matter at dimensions between approximately 1 and 100 nanometers, where unique phenomena enable novel applications. Encompassing nanoscale science, engineering, and technology, nanotechnology involves imaging, measuring, modeling, and manipulating matter at this length scale."*

The above quote is from the National Nanoscience Initiative, a U.S. federal research and development program established in 2000 under President Clinton, and is this author's preferred definition of the field of nanotechnology. The definition is broad yet is still a good starting point to discuss the work presented in this thesis, which concerns the use of DNA as a nanoscale construction material. A commonality in a lot of current nanotechnological research is the bridging of scientific fields which have traditionally been more separated. In this way many researchers envision synergistic effects fostering new approaches to research and application. Bridging of traditional fields is also important for the work presented in this thesis, where components from biology, physics and chemistry are represented.

The combination of physics, chemistry and biology at the nanoscale is a natural one. These fields have all been progressing towards the nano length scale in recent years, and this is therefore a natural place to bridge them. From the physics side, the miniaturization of components, particularly for computation, has evolved from minimum feature sizes of 1 μm in 1990, to roughly 30 nm in 2011.[1] This form of nanotechnology is known as top-down, a term coined by Richard Feynman in an inspirational talk from 1960,[2] since bulk materials are cut, etched and milled to nanoscale dimensions. Opposing this method of nano construction is the bottom-up approach where small components, such as atoms or molecules, are brought together to form nanostructures. Synthetic organic chemistry is a prime example of bottom-up construction, and the synthesis of ever larger structures has taken this field to nano scales, as exemplified through dendrimers, which are large branching molecules.[3] However, synthesis of extremely large target molecules is a time consuming process, and achieving a desired structure is often impossible. Nanochemistry instead often relies on the principle of molecular recognition to form large nanoscale structures. In this approach, small components are created with specific functionalities allowing them to assemble on their own in solution. Such self-assembly approaches are to a large extent inspired by biological molecules such as DNA which assembles based on the sequence of four deoxyribonucleotides. The size of DNA with a width of only 2 nm and a variable length also makes it an interesting nanoscale component in its own right. It is also in the realm of biology that truly magnificent systems of bottom-up construction are found. Cellular mechanisms are largely governed by proteins, which are self-assembled components with typical nanoscale dimensions. Bionanotechnology in general, attempts to use biological components for novel applications, or to mimic biological systems.

The components used in this thesis which are inspired from traditional fields of research are presented in Figure 1, and will be introduced in the following text. The most important of these is DNA which is used as a structural material in all the work presented in this thesis. The use of DNA in this way, far removed from its biological origin is the realm of DNA nanotechnology. The thesis consists of two parts related to original work in DNA nanotechnology; the first brings the assembly of DNA nanostructures from solution to surfaces and the second uses DNA as a component in a mimic of photosynthetic light harvesting.
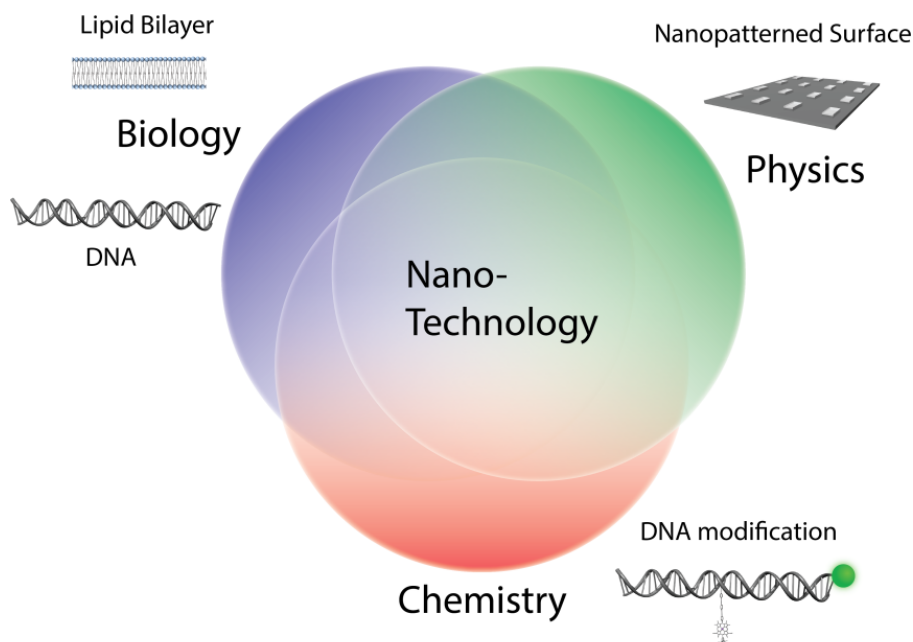
Figure 1. A schematic drawing showing the realm of nanotechnology emerging from the cross-disciplinarity of the traditional fields of biology, chemistry, and physics. From biology comes the most important molecule in this thesis, DNA. Also lipid bilayers are bioinspired components which appear throughout this work. The self-assembled attachment of DNA to lipid bilayers in this work uses covalent porphyrin modifications of the DNA. This is an example of chemical DNA modification which is also used to fluorescently label DNA. The porphyrin modification also allows DNA structures to bind to hydrophobic surfaces, nano-patterned with electron beams, a typical tool in physics research.

The field of DNA nanotechnology has mostly been concerned with the assembly of elaborate shapes in solution.[4] Surfaces have been used in the construction of repetitive 2D DNA crystals or for irreversible attachment of DNA. The approach investigated in this thesis considers the *reversible* assembly of DNA structures on surfaces as presented in papers 1 and 2, an area which is poorly studied. For this to be possible the DNA needs to be in as similar environment as possible to solution, while still being attached to the surface. To overcome this contradiction a hydrophobic anchor is covalently attached to the DNA. The anchor adds a self-assembling functionality to the DNA, allowing it to attach to a range of hydrophobic surfaces. The surface we mainly employ

is the lipid bilayer, both in the form of liposomes and supported lipid bilayers, an example of a bio-inspired component with nanoscale dimensions. The bilayer is soft and allows the DNA to reversibly assemble on the surface, while the porphyrin partitions into the hydrophobic layer. The mobility of individual lipids in the bilayer also allows the attached DNA constructs to diffuse, which may have implications for mobile nano systems. This is studied using fluorescently labeled DNA. It is also shown that several anchors are needed to align 2D DNA structures with the bilayer surface. Such alignment is required for many potential surface based applications involving DNA.

Currently, a great deal of research within the field of DNA nanotechnology aims to functionalize DNA structures for novel applications. In the second part of this thesis functionalization of DNA using fluorescent dyes is used in the construction of DNA based constructs which mimic natural photosynthetic components, with a focus on light harvesting antenna systems as presented in papers 3 and 4. Here, the inspiration from biology is self-evident. Photosynthesis is the conversion of energy from sunlight into chemical energy which can be used by the cells of photosynthetic organisms. A major component in this machinery absorbs sunlight and shuttles it to a specific reaction center. In natural systems proteins act as scaffolds for light harvesting dyes. Many approaches exist which aim to mimic the light harvesting process, yet DNA offers a novel route by playing the part of the scaffold. The scaffold is functionalized using DNA binding dyes, which rely on self-assembly to form the desired DNA-dye construct. In terms of dye spacing these novel DNA constructs are remarkably similar to the natural systems. This part of the thesis concerns the characterization of their function, and it is seen that these DNA based systems can harvest light on par with natural systems. Also surface attachment of the light harvesting DNA structures is briefly investigated, where the constructs are attached to nano-patterned surfaces via a hydrophobic porphyrin anchor. It is interesting to note that light harvesting relies on excitation energy transfer. This is a quantum mechanical process relying on the close spacing of the dyes. In this sense the work is a prime example of nanotechnology *"where unique phenomena enable novel applications"*.

In natural systems the energy is harnessed at the reaction center through electron transfer reactions. This process is mimicked in paper 5 by using two porphyrin anchors which bind a third molecule between them through self-assembly. Inspiration for this work is also drawn from enzymes which bind a particular substrate at functional sites and subsequently catalyze a reaction. The two porphyrins can also be viewed as such a binding pocket, where the enzymatic activity is provided by photoinduced reduction of the ligand.

The thesis is divided into four main sections. The first section introduces the methodology and fundamental concepts which provide a framework for understanding the novel work presented and the techniques used. This is followed by a section which aims to demonstrate how many of the components used in this work rely on self-assembly to form, and how different components also self-assemble through molecular interactions. This section will provide the reader with an overview of all the components used to build various functional structures, how they function, and most importantly how they self-assemble. It will also provide the reader with background

information pertaining to previous research that is related to the work presented in this thesis. Following this, a section on light harvesting is presented. This will provide the reader with fundamental knowledge of the process that is mimicked in papers 3 and 4, and will also provide examples of DNA constructs that rely on principles from light harvesting, which have previously been constructed. The final section will present the novel work and papers which this thesis is based on. It will start with the work concerning the reversible assembly of DNA structures on lipid bilayer surfaces, followed by work which mimics biological light harvesting and charge separation.

2 METHODOLOGY AND FUNDAMENTAL CONCEPTS

In this section the interaction between light and molecules which leads to absorption and fluorescence will be considered. Closely related to this is the concept of energy transfer, where excited state energy located on one molecule is transferred to another in close proximity. The instrumentation used to measure absorption, steady-state fluorescence, and time-resolved fluorescence will briefly be discussed. This will be followed by a brief description of confocal and total internal reflection fluorescence microscopy (TIRF-M) setups used for measuring diffusion of porphyrin- anchored DNA constructs on supported lipid bilayers and number of DNA origami adsorbed to hydrophobic surfaces, respectively. Finally, the quartz crystal microbalance with dissipation monitoring (QCM-D) technique is introduced. QCM-D was used to probe the binding density and viscoelastic properties of porphyrin- anchored DNA constructs on supported lipid bilayers, and to investigate the reversible assembly properties of the DNA attached in this manner.

2.1 MOLECULES, LIGHT, AND ENERGY

Central to the work presented in this thesis is the use of optical spectroscopy to study the environment and properties of various DNA constructs and their associated modifications. Such measurements can also reveal information about the characteristics of energy transfer in artificial photosynthetic systems. This section will start with a basic theoretical introduction to interactions between light and molecules, focusing on absorption and fluorescence, and then move on to a description of the instrumentation and techniques used. For the theoretical treatment, light will be considered classically whereas the molecule will be considered quantum mechanically. This treatment will in turn naturally lead to a simple representation of the phenomenon of energy transfer which is important for photosynthetic light harvesting and is closely related to absorption/fluorescence of light. The similarities between the two processes will be highlighted. Focus will be put on the important parameters which influence the various processes, instead of a thorough quantum mechanical treatment. These sections are based on several books on fluorescence and molecular spectroscopy.[5, 6]

2.2 ABSORPTION OF LIGHT

The light that we see is just a portion of the electromagnetic spectrum, specifically with wavelengths between 400 and 700 nm. Humans have evolved to observe these wavelengths since our sun has its peak output in this energy region. Consequently, it is no surprise that visible light is also extremely important for photosynthetic organisms which use the suns energy to create chemical bonds and thereby store it for later use. Conjugated organic molecules generally absorb light in the visible range, and small organic dyes are responsible for light absorption in natural photosynthesis. For the work presented in this thesis, organic dyes are used in artificial light harvesting complexes and as fluorescent probes.

To understand how light can interact with small organic molecules such as those which are responsible for light harvesting in photosynthesis, it is convenient to consider electromagnetic radiation as waves characterized by electric and magnetic fields oscillating perpendicularly to each other both in time and in space, transverse to the direction of propagation. The electric field component can interact strongly with charged particles, such as the loosely bonded electrons in conjugated organic molecules. To understand this interaction, let us start by considering some of the important results from a quantum mechanical treatment of organic molecules. For a qualitative description of the interaction it is useful to employ the Born-Oppenheimer (BO) approximation wherein the electronic, nuclear, and spin components of the overall molecular wavefunction are separated. Solving the Schrödinger equation results in a description of the molecule as a series of stationary electronic states with discrete energy (see the Jablonski energy level diagram[7] in Figure 2). As the size of a conjugated system increases, the spacing between electronic levels decreases as does the lowest energy transition between states. This is exemplified in Figure 4 for some of the dyes used in this thesis. The nuclear parts of the molecular wave function result in vibrational sublevels associated with each electronic state.

At room temperature a molecule in solution will generally occupy the lowest energy electronic state, known as the ground state. Furthermore, the lowest energy vibrational state will also be primarily occupied based on Boltzmann statistics; for a lowest excited vibrational state energy of 1400 cm^{-1} only ~1/1000 molecules are in a vibrationally excited state at room temperature. Therefore, absorption in Figure 2 starts at the lowest vibrational level of the electronic ground state (S_0). However, a molecule can be excited to higher energy electronic configurations, and it is the light induced transition between the ground state and these *excited* states which we will consider below. This transition generally results in a molecule being both vibrationally and electronically excited, and is therefore termed a vibronic transition. For simplicity we can consider the excitation as the promotion of a single electron from a low energy occupied orbital to a higher energy unoccupied orbital. Excitation then results in two un-paired electrons, giving rise to spin-singlet excited states ($S_{n>0}$) where the two un-paired spins are anti-parallel and spin-triplet states ($T_{n>0}$) where the spins are parallel.

Quantum mechanically, to induce transitions between stationary states, a time-dependent perturbation is needed. The influence of an electric field on a molecule is exactly such a perturbation, and can be treated through time-dependent perturbation theory. The electric field is assumed to be weak enough that the energies of the stationary molecular states are not altered, and this is generally a good approximation. Since both the ground and excited states have discrete energies it is no surprise that one result from such a treatment is that that the energy of the electric wave must match a possible transition between stationary states in the molecule for absorption to occur. This is known as the Einstein-Bohr frequency (or resonance) condition and the process is shown below,

$$A + h\nu \rightarrow A^* \tag{1}$$

$$\Delta E = h\nu = \frac{hc}{\lambda} \tag{2}$$

where A is the molecule in its ground state, $h\nu$ is the energy of the light (Planck's constant, h, multiplied by the frequency of the light, ν. Equation 2 thereby relates the energy difference between two molecular vibronic states, ΔE, to the wavelength of the light, λ, and the speed of light, c .
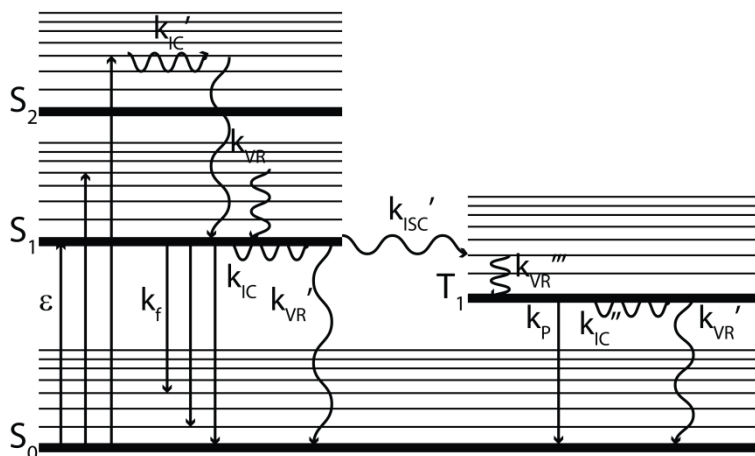

Figure 2. Jablonski energy level diagram showing processes which occur due to the interaction of light and molecules. Each process in the diagram is represented by its accompanying rate constant k_i, where i denotes the process. Radiative transitions are displayed as straight lines and non-radiative transitions are waves. Absorption (ε) promotes the molecule from the lowest vibrational level of the ground state (S_0) to an excited vibronic singlet state. Internal conversion (IC) followed by vibrational relaxation (VR) results in the molecule quickly occupying the zero vibrational level of S_1. From here the excitation energy is released through fluorescence (f), IC, or transfer to a triplet state through intersystem crossing (ISC). From the lowest vibrational level of the triplet state the energy is dissipated through ISC to the ground state followed by vibrational energy to the lowest vibrational level, or through the radiative transition of phosphorescence (P).

As spectroscopists we are interested not only in the wavelength of a transition as given through the resonance condition, but also in its magnitude (or strength). The strength of a transition is directly proportional to its transition rate, and it is useful to consider which factors yield high absorption strengths, as this is desirable in many contexts. In the realm of time-dependent perturbation theory the transition rate of a process, $R_{i \to f}$, from an initial state, Ψ_i, to a final state, Ψ_f, can be found through the use of Fermi's golden rule, first derived by P.A.M. Dirac,[8]

$$R_{i \to f} = \frac{2\pi}{\hbar} \rho \left| \langle \Psi_f | \hat{H}' | \Psi_i \rangle \right|^2 \tag{3}$$

where $\hbar$ is Planck's constant divided by 2π, ρ is the density distribution of final states and $\hat{H}'$ is the perturbation Hamiltonian.

For the special case where the perturbation is caused by an electric field in the form of light, $\hat{H}'$ can be approximated by the scalar product between the electric field and the dipole operator for the molecule

$$\hat{H}' = -\vec{E}(t) \cdot \hat{\mu} \tag{4}$$

where $\hat{\mu}$ is the dipole operator,

$$\hat{\mu} = \sum_j \vec{r_j} q_j \tag{5}$$

and is a sum over all charges in the molecule, q_j, multiplied by their positions, $\vec{r_j}$. By combining equations 3 and 4, $R_{i \to f}$ for a light induced transition may be written as

$$R_{i \to f} = \frac{\left(\vec{E_0} \cdot \vec{\mu}_{fi}\right)^2}{\hbar^2} \rho_\nu\left(\nu_{fi}\right) \tag{6}$$

where $\rho_\nu\left(\nu_{fi}\right)$ is the number of modes of oscillation of the electric field per unit frequency interval in the frequency region of the transition, ν_{fi}, $\vec{E_0}$ is the amplitude of the oscillating electric field, and $\vec{\mu}_{fi}$ (equation 7) is known as the electronic transition dipole,[9] where ψ_f and ψ_i are electronic wave functions.

$$\vec{\mu}_{fi} = \langle \psi_f | \hat{\mu} | \psi_i \rangle \tag{7}$$

The contribution from the different vibronic transitions between vibrational state *m* of the ground state and *n* of the final state on the rate of absorption depends on the square of the transition moment, which for an allowed electronic transition is

$$\left|\vec{\mu}_{fi,nm}\right|^2 = \left|\vec{\mu}_{fi}\right|^2 \left|\langle \chi_{f,n} | \chi_{i,m} \rangle\right|^2 \tag{8}$$

where $\chi_{f,n}$ is the wavefunction related to state *n* of the excited electronic state and $\chi_{i,m}$ is the wavefunction related to state *m* of the electronic ground state. The square of the vibrational overlap integrals in equation 8 are known as Franck-Condon factors for the different vibronic transitions, and must be non-zero for a given vibronic transition to be allowed.[10, 11]. It should be noted that the vibrational wavefunctions constitute an orthonormal set, so that the Franck-Condon factors sum to 1 for the complete transition and therefore do not appear in equation 7.

The transition dipole has both a magnitude as well as a direction which in turn is related to the net movement of charge during the transition. It is important to note the dot product in equation 6 which ensures that for a polarized electric field the probability of a transition is strongest if the electric field is parallel to the transition dipole moment. From equation 6 we see that the main molecular component which determines the strength of the transition is the square of the transition dipole, often called the dipole strength and written D_{fi}.

2.3   UV/VIS ABSORPTION SPECTROSCOPY

Although the transition rate $R_{i \to f}$ presented above is a useful quantity for a conceptual description of the strength of light absorption, it is not directly accessible through experiment. Instead, the absorbing ability of a molecule is found through its molar

absorption coefficient $\varepsilon(\lambda)$ (units of $M^{-1}cm^{-1}$), which is found through the use of the Lambert-Beer law relating absorbance, A, to concentration, c, and light path through the sample, l,

$$A(\lambda) = -log\frac{I(\lambda)}{I_0(\lambda)} = \varepsilon(\lambda)cl \qquad (9)$$

Measurements of absorption are performed using a spectrophotometer where a lamp shines light through a cuvette with a dilute sample of the molecule or system being studied. The intensity of the light before reaching the sample, I_0, is measured and compared to the intensity of light after passing through the sample, I (see Figure 3). A monochromator is used to select the wavelength of the incoming light. The absorbance is subsequently evaluated over a range of wavelengths, using equation 9, yielding a full absorption spectrum of the molecule, generally taken in the wavelength interval between 200 and 800 nm, from the ultra-violet to the near-infrared.
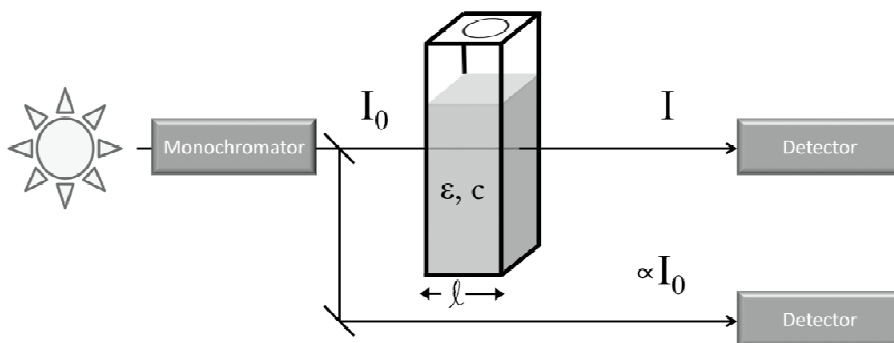

Figure 3. Main components of an absorption spectrometer. The wavelength of excitation is selected with a monochromator and the light is subsequently split to allow measurement of the initial intensity I_0. Light passes through the sample with absorption coefficient ε, concentration c, and light-path l, and is recorded as I on a detector.

An absorption spectrum will consist of peaks at wavelengths where the molecule being measured absorbs, and valleys where light passes through the sample and the sample is transparent. By studying absorption spectra of photosynthetic systems it is easy to see why they are colored as they are. For example, the main light harvesting molecules (chromophores) in the leaves of green plants are chlorophylls and to a lesser extent carotenoids. The chlorophylls absorb in the UV at around 400 nm (blue light) and have a lower energy transition at around 650-800 nm (red light). This leaves the green light unabsorbed, and this is therefore the color we observe.

The absorption coefficient ε is the experimental quantity which defines the strength of the vibronic transitions. This value can be related to the quantum mechanical dipole strength through equation 10 where the integral is over all frequencies, ν, of the full electronic transition,

$$D_{fi} = K_1\left(\frac{n}{f^2}\right)\int\frac{\varepsilon}{\nu}d\nu \qquad (10)$$

where f is the local field correction factor which appears due to differences in polarizability of the molecule and the surrounding medium, n is the refractive index of the medium in which the molecule or system is dissolved, and K_f is a constant.

It should be noted that molecular size (specifically the extent of the conjugation) is an important factor for the maximum strength of an electronic transition, since the D_{fi} is related to the net movement of charge during the transition. An example of this is found by considering the fully allowed lowest energy transitions of some of the small conjugated organic molecules encountered later on in this thesis (Figure 4). The relatively small DNA bases have strongly allowed transitions with the pyrimidines displaying an absorption coefficient of 6-8000 M^{-1}cm^{-1}, whereas the slightly larger ring structures of the purines display absorption coefficients of 12-15000 M^{-1}cm^{-1} (section 3.1.1). The DNA binding dye YO (section 3.2.1) has an absorption coefficient of 50 000 M^{-1}cm^{-1} and the dye Cy5 (section 3.2.2) displays the highest absorption coefficient at 250 000 M^{-1}cm^{-1}.

Cytosine	Adenine	YO	Cy5
λ_{max} = 270 nm	λ_{max} = 260 nm	λ_{max} = 480 nm	λ_{max} = 649 nm
ε = 6000 M^{-1}cm^{-1}	ε = 13 000 M^{-1}cm^{-1}	ε = 60 000 M^{-1}cm^{-1}	ε = 250 000 M^{-1}cm^{-1}
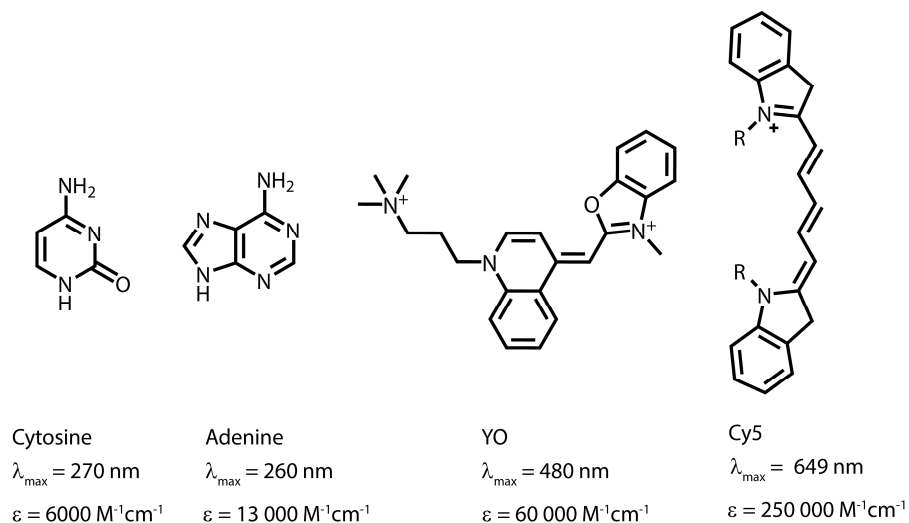
Figure 4. Examples of conjugated organic dyes which appear in this thesis showing that the extent of conjugation affects both the wavelength of the lowest energy transition and the absorption coefficient accompanying the transition. Cytosine and adenine are DNA bases, YO is a DNA binding dye, and Cy5 is a fluorescent label often used with DNA.

2.4   PROCESSES IN THE EXCITED STATE

The excited state is not stable, and many rapid pathways exist which serve to deactivate it. It is convenient to treat these different processes in terms of their related rate constants, k_i, where i is a designation of a particular process. This section will start by considering fluorescence and then move on to competing deactivation pathways in media with several chromophores in close proximity, namely energy and electron transfer.

2.4.1   FLUORESCENCE

Immediately after excitation the molecule is in a specific vibronic level (see Figure 2). In solution energy is quickly dissipated through internal conversion (IC) to lower electronic states followed by vibrational relaxation (VR) due to collision with solvent molecules. Internal conversion between the lowest excited singlet state and the ground state is slower and will in many cases compete with fluorescence and intersystem crossing to the lowest triplet state (T_1). Therefore it is from the lowest vibrational level of S_1 that most excited state processes start.[12]

Fluorescence is the process of spontaneous emission of a photon from an excited molecule, without a change in spin multiplicity. Interestingly fluorescence is intimately related to the process of absorption, in the sense that a high rate constant of absorption in turn gives a high rate constant of fluorescence, k_f, as derived by Strickler and Berg among others (equation 11),[13-15] based on the original work by Einstein relating the transition rates for absorption, stimulated emission, and spontaneous emission. In other words, it is the dipole strength (equation 6) which determines the rate constant of the fluorescence process.

$$k_f = 2.880 \times 10^{-9} n^2 \frac{g_i}{g_f} \langle \nu_f^{-3} \rangle^{-1} \int \frac{\varepsilon(\nu)}{\nu} \, \mathrm{d}\nu \qquad (11)$$

In the above equation g_i and g_f are the degeneracies of the electronic states i and f, respectively, and ν_f is the frequency of the emission.[16]

Although large dipole strengths yield large fluorescence rate constants, a high rate constant of fluorescence does not guarantee that a molecule has a high probability to fluoresce. This can be understood by considering the other processes that can deactivate the excited state. For this discussion it is useful to consider the Jablonski diagram in Figure 2 to visualize the various deactivation pathways of the excited state. Every excited state process has an associated rate constant and the probability that a given process will deactivate the excited state is given through equation 12,

$$\Phi_i = \frac{k_i}{\sum_j k_j} \qquad (12)$$

where Φ_i is the quantum yield/efficiency of the process, k_i is the rate constant for the process and the sum in the denominator is over all the rate constants which deactivate the state including i itself.

There are particularly two experimental quantities which together yield the rate constants of fluorescence and the sum of the non-radiative decays. These are presented in equations 13 and 14 and are called the fluorescence quantum yield, Φ_f, and lifetime, τ_f, respectively. The quantum yield is the ratio of emitted photons to absorbed photons. Equation 15 relates the experimental quantities of the fluorescence quantum yield and lifetime to the fluorescence rate constant k_f, and non-radiative rate $k_{nr} = k_{ic} + k_{isc}$.

$$\Phi_f = \frac{\text{\# photons emitted}}{\text{\# photons absorbed}} = \frac{k_f}{k_f + k_{ic} + k_{isc}} \qquad (13)$$

$$\tau_f = \frac{1}{k_f + k_{ic} + k_{isc}} \qquad (14)$$

$$k_f = \frac{\Phi_f}{\tau}, \qquad k_{nr} = \tau^{-1} - \frac{\Phi_f}{\tau} \qquad (15)$$

2.4.2   FLUORESCENCE SPECROSCOPY

Fluorescence is generally measured either at steady-state, with constant illumination of the sample, or in a time-resolved regime where a light pulse is used to excite a population of molecules and the decay is studied. Steady-state measurements are used to calculate the quantum yields of molecules and time-resolved measurements can yield the lifetime.

2.4.2.1   STEADY-STATE FLUORESCENCE

Steady-state fluorescence spectra are recorded on a spectrofluorimeter, and the main components are shown in Figure 5. A monochromator before the sample selects the excitation wavelength, and generally fluorescence is measured at right angles to the excitation in order to avoid the excitation light entering the detector. After the sample a second monochromator selects the emission wavelength. In this way an emission spectrum is obtained by fixing the excitation monochromator and scanning the wavelength of emission, and an excitation spectrum is obtained by scanning the wavelength of excitation with a fixed emission wavelength.

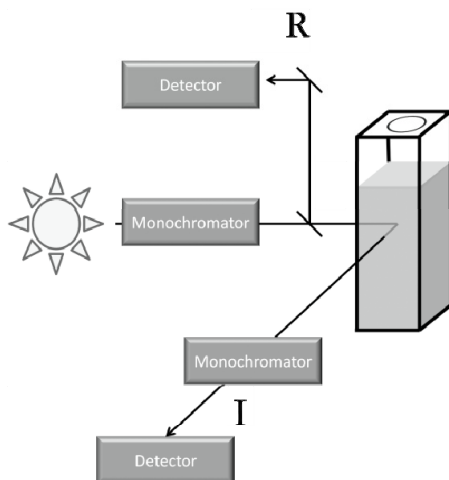Figure 5. Main components in a spectrofluorimeter. A monochromator selects the wavelength of excitation, and a signal (R) proportional to the excitation intensity is collected to allow for correction of variations in lamp intensity. The emission wavelength is selected with a second monochromator and collected at right angles to the excitation beam and the intensity *I* collected at the detector.

If the initial intensity of fluorescence at time 0 is I_0, a first order rate equation can often be used to describe the time dependence $I(t)$ of the fluorescence intensity if the sample is homogeneous and contains a single chromophore species, yielding a mono-exponential decay.

$$I(t) = I_0 e^{-t \sum_i k_i} = I_0 e^{-t/\tau} \tag{16}$$

The steady-state fluorescence intensity I_{ss} is given by equation 17, obtained through integration of equation 16.

$$I_{ss} = \int_0^\infty I_0 e^{-t/\tau} dt = I_0 \tau \tag{17}$$

The value I_0 depends not only on the intensity of the excitation source, but also on the concentration of emitting molecules as well as instrumental parameters. Therefore, a steady state measurement does not yield τ directly. However, by correcting for the lamp intensity and wavelength dependence in the detector sensitivity, a corrected emission spectrum is obtained. The integrated corrected fluorescence spectrum is then proportional to the quantum yield of fluorescence, Φ_f, which can be determined by comparing the fluorescence intensity with a molecule of known quantum yield,

$$\Phi_f = \Phi_{f,R} \cdot \frac{I}{I_R} \frac{(1-10^{-A_R})}{(1-10^{-A})} \frac{n^2}{n_R^2} \tag{18}$$

where I is the integrated fluorescence intensity, A is the absorbance at the wavelength of excitation and n is the refractive index of the medium, R denotes the reference sample.

2.4.2.2   TIME-RESOLVED FLUORESCECE

To gain information on the lifetime of a molecule, time-resolved fluorescence is necessary. It should be mentioned that the simple monoexponential decay described in equation 16 is often insufficient to describe the decay of fluorescence in complex samples. In these cases several exponential functions may be necessary to describe the decay. In some cases, for example when energy transfer is present and the distance between two chromophores varies, a distribution of decays is necessary.[17]

In this thesis the method of time-correlated single photon counting (TCSPC) is used for measurements of fluorescence lifetime. As the name suggests both counting and timing of emitted photons is conducted. A sample is excited by a pulse of light and the time from excitation to the first photon hits the detector is recorded. This procedure is repeated numerous times and the passage time of the first photon is in this way collected in a histogram (see Figure 6). Generally at least 10 000 counts are collected in the peak channel to obtain good statistics. In this way the shape of the fluorescence decay is recreated, but is convolved with the instrument response function (*irf*) of the detection system and the pulse,

$$R(t) = irf(t) \otimes I(t) = \int_{-\infty}^t irf(t') \cdot I(t-t') \, dt' \tag{19}$$

where $R(t)$ is the recorded histogram, $irf(t)$ is the time evolution of the instrument response function and $I(t)$ is the true decay of the sample. The lifetime is commonly found by convolving a guess decay consisting of a sum of exponential functions with the *irf* and fitting this to the measured data using a least squares algorithm.
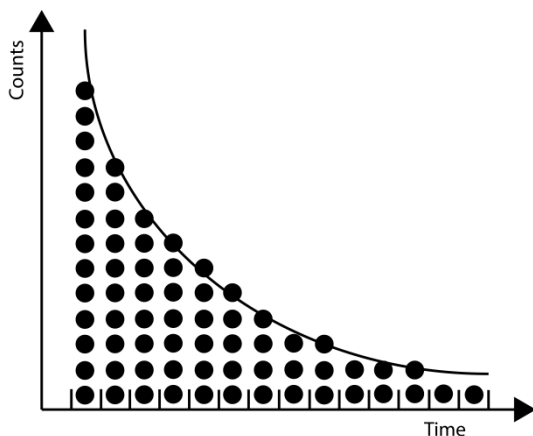

Figure 6. Schematic representation of the histogram of the number of counts in each time interval. For a real measurement ~10 000 counts are collected in the top channel and the time axis is divided into ~2000-8000 channels.

2.4.3   ENERGY TRANSFER (FRET)

Until now only isolated molecules have been considered. However, in systems such as photosynthetic light harvesting complexes, many molecules are present in close proximity. In such cases, interactions between the molecules must be taken into account. This interaction can allow excited state energy on one chromophore to transfer to another. It is to a large degree the distance between the chromophores which determines the type and magnitude of these interactions. At very short distances where the molecular orbitals of the chromophores overlap, energy transfer is possible via an electron exchange mechanism where the two chromophores formally swap two electrons.[18] At longer inter-chromophore distances the dominating interaction is Coulombic in nature. For the systems we study in this thesis and for the chlorophyll dyes found in natural light harvesting systems which both have strongly allowed transitions, the Coulombic interaction is much larger than the electron exchange interaction, and electron exchange can be ignored. We will be considering the effect on molecules which are only weakly electronically coupled to one another where the interaction between the two chromophores can be modeled as the interaction between two point dipoles situated at the centers of each chromophore. The weak coupling also ensures that the vibrational states of the excited chromophores have reached thermal equilibrium before the transfer occurs. This is equivalent to the statement that excited state processes originate (mostly) in the lowest vibrational level of S_1 (section 2.4.1). The process of energy transfer under the above conditions is called Förster resonance energy transfer (FRET).[19, 20] However, when the electronic coupling is larger, the vibrational modes are not in thermal equilibrium and coherent transfer processes can

occur. These will not be considered in this thesis and likely are not important for the artificial systems we study, but may play an important role in natural light harvesting.[21-25]

In the weak coupling regime the chromophores do not interact in their ground states. However, when a molecule is excited it produces an electric field which can interact with neighboring molecules in a similar manner to electromagnetic radiation. The initially excited molecule (energy donor) returns to its ground state, while the energy accepting molecule goes from a ground state to an excited state. For such a transfer of energy to be possible a resonance condition must be fulfilled meaning that the upward and downward transitions must be equal in energy. This resonance condition is analogous to the one for the interaction between electromagnetic radiation and molecules, and gives the name *resonance* energy transfer to the process.

As with the other excited state processes that have been described until now, energy transfer in the weak coupling regime predominantly starts from the lowest vibrational level of S_1. It therefore constitutes a competing process with the other deactivation pathways, and should be considered as such. To evaluate the efficiency of energy transfer in a system, the rate constant is needed, as shown in equation 12. One of the most powerful traits of Förster theory is that the quantum mechanical rate constant for excitation energy transfer, k_{EET}, can be related to experimentally accessible spectroscopic properties of the donor and acceptor. To understand this, some of Förster's main results which lead from a quantum mechanical description to a description which uses the fluorescence spectrum, quantum yield, and lifetime of the donor and the absorption spectrum of the acceptor will be shown.

For this discussion the donor is designated molecule 1 and the acceptor is designated molecule 2. Since the electronic coupling is weak, perturbation theory is applicable and the rate constant for excitation energy transfer can be written using equation 3, Fermi's golden rule. In solution all molecules are interacting in a slightly different manner with their surroundings and some are in vibrationally excited states. This results in many different donor and acceptor transition energies. For each donor transition energy, all acceptor transition energies must be considered, to see if they match the resonance condition. The density of acceptor states with transition energies in the range of the donor emission energy, $\rho_{s2}(E_1)$, therefore appears in the expression (equation 20). This is the density of final states appearing in equation 3. To take into account all the possible donor transition energies an integral is taken over the density of donor energies, $\rho_{s1}(E_1)$,.

$$k_{EET} = \frac{2\pi}{\hbar} \int_{-\infty}^{\infty} |H_{21}|^2 \, \rho_{s2}(E_1)\rho_{s1}(E_1)\mathrm{d}E_1 \tag{20}$$

The matrix element H_{21} can, under the Born-Oppenheimer approximation where it is assumed that the energy transfer is much faster than the movement of nuclei, be written as the product of an electronic matrix element and two nuclear overlap integrals

$$H_{21} = H_{21(el)}\langle\chi_{1i}|\chi_{1f}\rangle\langle\chi_{2f}|\chi_{2i}\rangle \tag{21}$$

The nuclear overlap integrals relate to any of the possible initial and final vibrational wavefunctions of the two chromophores. All of these nuclear overlaps must be considered and they must be weighted with their appropriate Boltzmann factors. The electronic interaction matrix element $H_{21(el)}$ for point dipole interaction is given in equation 22,

$$H_{21(el)} = (f^2/n^2)\sqrt{D_{fi(1)}}\sqrt{D_{fi(2)}}\kappa\left|\vec{R}_{21}\right|^{-3} \tag{22}$$

where $D_{fi(1)}$ is the donor dipole strength, $D_{fi(2)}$ is the acceptor dipole strength, and $\vec{R}_{21}$ is the distance between the two point dipoles. Energy transfer between two different types of molecules is known as hetero-FRET, and energy transfer is also possible between two identical molecules, and is known as homo-FRET where $D_{fi(2)}$ is replaced with $D_{fi(1)}$. κ is an orientation factor between the two transition dipoles given as

$$\kappa = \cos\theta - 3\cos\alpha\cos\beta \tag{23}$$

where θ is the angle between the two transition dipoles, and α and β are the two angles the transition dipoles make with $\vec{R}_{21}$.

By combining equations 20-22, k_{EET} becomes

$$k_{EET} = \frac{2\pi}{\hbar}\left(\frac{f^4}{n^4}\kappa^2\left|\vec{R}_{21}\right|^{-6}\right)\int D_{fi(1)}X_1(E_1)\,\rho_{s1}(v)D_{fi(2)}X_2(E_1)\rho_{s2}(v)\mathrm{d}E_1 \tag{24}$$

where $X_1(E_1)$ is a thermally weighted Franck-Condon factor for emission with energy $E_1=hv$, $X_2(E_1)$ is a thermally weighted Franck-Condon factor for absorption with energy $E=hv$. It is important to take note of the $(\vec{R}_{21})^{-6}$ dependence on distance for the rate constant, which ensure that the rate of energy transfer quickly decreases with inter-chromophore distance.

From equation 24 we see that there are terms within the integral over transition energies (E_1) that are the dipole strength, thermally weighted Franck-Condon factor, and energy density around the transition frequency for both the donor and acceptor. These factors are therefore expected to be related to the absorption spectrum of the acceptor and the fluorescence rate constant of the donor, based on equations 8, 10, and 11. Indeed, it is possible to rewrite these equations to incorporate these exact parameters,

$$\varepsilon(v) = v \cdot D_{fi}X_{abs}(E)\frac{\rho(v)}{h} \tag{25}$$

where D_{fi} is the dipole strength of the transition, $\rho(v)$ is the density of excited states around v, and $X_{abs}(E)$ is a thermally weighted Franck-Condon factor for absorption with energy $E=hv$.

The rate constant for fluorescence can be written in terms of a rate constant which is dependent on frequency, $F(v)$, analogous to $\varepsilon(v)$ for absorption,

$$k_f = \int F(\nu) \mathrm{d}\nu = K \cdot \int \nu^3 D_{fi} X_{em}(E) \rho(\nu) \mathrm{d}\nu \tag{26}$$

where D_{fi} is the electronic dipole strength of the transition, $\rho(\nu)$ is the density of excited states around ν, $X_{em}(E)$ is a thermally weighted Franck-Condon factor for emission with energy $E = h\nu$, and K is a constant. We see in this equation that it is $F(\nu)$, not k_f, which is directly related to the terms within the integral in equation 24.

Equation 24 can now be combined with equations 25 and 26 to yield Förster's equation for resonance energy transfer, including an overlap integral, J, over the emission spectrum of the donor and absorption spectrum of the acceptor.

$$k_{EET}(r) = 8.79 \times 10^{-5} \left(\frac{\Phi_{f,1}}{\tau_{f,1}} \kappa^2 n^{-4} J \left| \vec{R}_{21} \right|^{-6} \right) \tag{27}$$

$$J = \frac{\int_0^\infty F_1(\lambda) \varepsilon_2(\lambda) \lambda^2 \mathrm{d}\lambda}{\int_0^\infty F_1(\lambda) \lambda^{-2} \mathrm{d}\lambda} \tag{28}$$

written on the wavelength scale as this is the common units obtained from spectrophotometers. Notice that the overlap integral contains the term $F_D(\lambda)$ as expected, yet also an integral in the denominator. This is because $F(\nu)$ is not directly measureable through experiment, but the *shape* of the emission spectrum is obtained by normalizing with the integrated emission spectrum of the donor, $\int_0^\infty F_1(\nu) \mathrm{d}\nu$, which requires the concomitant multiplication by this same factor. Notice from equation 26 that this normalizing integral is the rate constant of fluorescence $k_{f,1}$. This factor therefore appears outside the overlap integral J in equation 27, as the donor quantum yield divided by donor lifetime (equation 11). The two factors of λ^2 and λ^{-2} in J may appear slightly confusing, since a factor ν^{-1} in the numerator is expected from equation 25 and a factor of ν^{-3} is expected from equation 26. The reason is that $\mathrm{d}\nu = -\lambda^{-2} \mathrm{d}\lambda$, thereby yielding equation 28.

In cases where the orientation factor is known the rate constant can be calculated exactly, and it is useful to relate the rate constant to the parameter $\bar{R}_0$, which is the dynamically averaged Förster distance; the donor-acceptor distance where 50 % of the excited state energy is transferred to the acceptor assuming random orientation between the two dyes.

$$k_{EET}(R_{21}) = \frac{3\kappa^2}{2} \frac{1}{\tau_D} \left(\frac{\bar{R}_0}{R_{21}} \right)^6 \tag{29}$$

$$\bar{R}_0 = 0.141 \left(n^{-4} \Phi_{f,D} J(\lambda) \right)^{1/6} \tag{30}$$

The efficiency of the energy transfer, E, is calculated from equation 12, as shown in equation 31, and can be obtained experimentally by recording the quenching of the donor fluorescence. This can be found either from emission quenching or from lifetime quenching.

$$E = \frac{k_{EET}}{k_{EET}+(\tau_D)^{-1}} = \frac{1}{1+(2/3)\kappa^{-2}(R_{21}/R_0)^6} = 1 - \frac{F_{DA}}{F_D} = 1 - \frac{\tau_{DA}}{\tau_D} \tag{31}$$

where F_{DA} is the fluorescence intensity of the donor with the acceptor present, F_D is the donor fluorescence intensity without the acceptor present, τ_{DA} is the lifetime of the donor in the presence of the acceptor, and τ_D is the donor lifetime without the acceptor present.

It is worthwhile to consider the highest rates possible for FRET. Let us take chlorophylls from light harvesting complexes as an example and compare the maximum rates of FRET with the other processes which can deactivate the excited state. R_0 values for FRET between two chlorophylls is in the range of 80 Å, and taking a distance of 20 Å between them where Förster theory is applicable, $k_T(20 \text{ Å}) = (k_f + k_{ic} + k_{isc}) \times 4 \times 10^3$, 4000 times higher than the sum of the other rates!

2.4.4   FRET IN MULTI-CHROMOPHORE SYSTEMS

Until now we have only considered energy transfer between a pair of molecules. However, in multi-chromophore systems there are many chromophores in close proximity and electronic interaction between all chromophores must be considered. The probability that a given transfer from a specific excited donor to a specific acceptor will take place must thus be considered against transfer from the donor to all other possible acceptors in the system, as well as the usual deactivation pathways of fluorescence and non-radiative return to the ground state. For the next part it will be useful to separate the probability of energy transfer to all possible acceptors in the system from the probability that the excitation energy will be dissipated. This yields two probability expressions where Förster theory is used to calculate energy transfer rate constants,

$$p_{ij} = \frac{k_{ij}}{\tau_i^{-1}+\sum_{i\neq l} k_{il}} \tag{32}$$

$$p_{i,out} = \frac{\tau_i^{-1}}{\tau_i^{-1}+\sum_{i\neq l} k_{il}} \tag{33}$$

where p_{ij} is the probability of transfer from excited chromophore i to chromophore j, $p_{i,out}$ is the probability that excited state i will return to the ground state through another process than energy transfer, k_{ij} is the Förster energy transfer rate between excited chromophore i and chromophore j given by equation 29, τ_i^{-1} is the sum of the radiative and non-radiative decay rates of chromophore i (the lifetime of chromophore i in the absence of energy transfer), and the summations in equation 32 and 33 are over all energy transfer rates from chromophore i to all other chromophores in the system. For chromophores which are energy acceptors, and have no emission overlap with the donors, $p_{i,out}$ is 1 and p_{ij} is zero for all j, since energy transfer from these chromophores is not possible.

In systems where the orientation factor between fluorophores is known, the FRET rate constant can be calculated, yielding all possible transfer probabilities from all possible

excited dyes. This information can be used to construct a Markov chain model of the energy transfer process, where the probabilities of the excitation energy being located on each individual dye in the system are evaluated after each transfer step.

This model has been used to simulate fluorescence depolarization in DNA based multi-chromophoric systems capable of homo-transfer. A detailed description of the model is given by Albinsson *et al* where it is used to describe fluorescence depolarization of intercalated YO.[26] Here we present a basic outline with our modifications to the main model.

For a DNA system with N_d donor chromophores and N_a acceptor chromophores there are N_d+N_a different chromophore positions. The distribution of excitation energy after a discrete number of steps (transfers) n is described by a vector ($\vec{v}_n$). By combining the initial distribution of excitation energies ($\vec{v}_0$) with a matrix ($\mathbf{M}$) consisting of the energy transfer and emission/non-radiate decay probabilities described above, the energy distribution after an arbitrary number of steps can be described.

$$\vec{v}_n = \vec{v}_{n-1} \cdot \mathbf{M} = \cdots = \vec{v}_0 \cdot \mathbf{M}^n \tag{34}$$

The matrix $\mathbf{M}$ can be divided into four $(N_a + N_d) \times (N_a + N_d)$ submatrices

$$\mathbf{M} = \begin{bmatrix} \mathbf{A} & \mathbf{D} \\ \mathbf{0} & \mathbf{I} \end{bmatrix} \tag{35}$$

where $\mathbf{0}$ and $\mathbf{I}$ are the zero and unity matrices, respectively, $\mathbf{A}$ has a zero diagonal with the other elements equal to p_{ij}, and $\mathbf{D}$ is a diagonal matrix containing $p_{i,out}$ as diagonal elements.

The limit of the matrix $\mathbf{M}$ to the power of n when n goes to infinity is

$$\lim_{n\to\infty} \mathbf{M}^n = \begin{bmatrix} \mathbf{0} & (\mathbf{I} - \mathbf{A})^{-1}\mathbf{D} \\ \mathbf{0} & \mathbf{I} \end{bmatrix} \tag{36}$$

The steady state distribution of energy is described by the limiting value after an infinite number of steps:

$$\vec{v}_\infty = \vec{v}_0 \cdot \lim_{n\to\infty} \mathbf{M}^n \tag{37}$$

The $\vec{v}_\infty$ row matrix will consist of the steady-state probabilities of energy transfer being located on each dye in the system, given an initial distribution of excitation $\vec{v}_0$. By monitoring the elements in $\vec{v}_\infty$ which constitute acceptor dye positions, the overall transfer efficiency, E, is obtained as the sum of the probabilities of excitation energy being located on any of the acceptors.

A detailed description of the implementation of the model to DNA light harvesting systems, including the number of dyes, structure of the DNA scaffold, and dyes orientations are given in the text describing the original work presented in this thesis, section 5.2.1.

2.4.5   PARAMETERS OF LIGHT HARVESTING

Light harvesting systems will be considered in section 4. Here a short description of parameters used in this thesis to quantify the efficiency of light harvesting systems will be given. Briefly, light harvesting systems consist of a group of initial light absorbers which can transfer their excitation energy via homo- and hetero-FRET transfer to a specific acceptor or group of acceptors. Three main parameters are used to quantify the light harvesting process; the overall transfer efficiency, E, the antenna effect, AE, and the effective absorption coefficient ε_{eff}.

The overall transfer efficiency, E, is simply the ratio between the amount of energy transferred to the acceptor(s) and the amount of energy absorbed by the donors. The overall transfer efficiency can be found using the quenching of donor fluorescence exactly as for a single donor-acceptor pair using equation 31, either monitoring intensity or lifetime quenching. Sometimes it is difficult to obtain samples of the donor alone and donor-acceptor complexes with equal concentration. If fluorescence from both the donor and acceptor are clearly observed another option is possible.[27] Here the emission spectrum is decomposed into two components; one for the donor and one for the acceptor. E is then given by,

$$E = \frac{F_A/\Phi_A}{(F_A/\Phi_A + F_D/\Phi_D)} \tag{38}$$

where F_A is the integrated spectral component of the acceptor emission, F_D is the integrated spectral component of the donor emission, Φ_A is the unquenched donor fluorescence quantum yield and Φ_D is the unquenched acceptor fluorescence quantum yield.

The antenna effect is a measure of the increase in excitation of the acceptors as a consequence of the presence of the donors. If the donors fluoresce sufficiently to be measured one can find AE by first exciting the acceptor directly in its absorption peak and measuring the fluorescence intensity. This value is then divided by the acceptor emission obtained upon excitation of the donors to yield AE as shown in equation 39. AE is thereby the number of donors in a construct, n_D, multiplied by the donor absorption coefficient, ε_D, and overall transfer efficiency; E, divided by the number of acceptors, n_A and the acceptor absorption coefficient, ε_A.

$$AE = \frac{I_{A(ex,D)}}{I_{A(ex,A)}} = \frac{n_D \cdot \varepsilon_D \cdot E}{n_A \cdot \varepsilon_A} \tag{39}$$

In the above equations $I_{A(ex,D)}$ is the acceptor emission upon excitation of the donors at their peak absorption wavelength and $I_{A(ex,A)}$ is the acceptor emission upon direct excitation of the acceptors at their peak absorption wavelength. The formula assumes that the direct excitation of acceptors at the excitation wavelength of the donors is negligible. When this is not the case, the intensity due to direct excitation of acceptors must be subtracted from $I_{A(ex,D)}$.

AE is a good measure of the increased absorption the acceptor experiences due to the donors. However, it is not a measure of the amount of energy transferred to the

acceptor(s). Such a measure is desirable because it can be compared between different systems and yields the number of acceptor excitations due to the antenna under given light conditions. What we are interested in is the effective absorption coefficient of the acceptors due to energy transfer from excited donors. This parameter is obtained by multiplying AE by the acceptor absorption coefficient as shown in equation 40.

$$\varepsilon_{eff} = AE \cdot \varepsilon_A = \frac{n_D \cdot \varepsilon_D \cdot E}{n_A} \tag{40}$$

2.4.6   ELECTRON TRANSFER

In section 2.4.4 the notion of energy transfer between two chromophores in orbital contact through the formal exchange of two electrons between the donor and acceptor was briefly mentioned. When chromophores are in orbital contact also a photoinduced single electron transfer reaction can occur resulting in an oxidized donor and reduced acceptor. Also the reverse process is possible, resulting in a reduced donor and oxidized acceptor is possible, but is not relevant for the work presented in this thesis. In section 5.2.2 a supramolecular system is described, consisting of a binding pocket of two zinc-porphyrins and a bidentate ligand situated between them, coordinated to each zinc atom (P-L-P). In this work quenching of the porphyrin fluorescence due to photoinduced electron transfer to the ligand is studied, as shown in equation 41 where the excitation results in the excited state P*-L-P which can result in the oxidized/reduced state P$^+$-L$^-$-P.

$$P - L - P \xrightarrow{h\nu} P^* - L - P \rightarrow P^+ - L^- - P \tag{41}$$
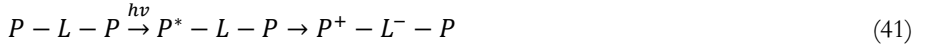
Different ligands are used with varying reduction potentials to study this effect on the quenching of the porphyrin fluorescence. Photoinduced electron transfer is expected if the free energy change (driving force) of the process is negative, $\Delta_{ET}G^0 < 0$. A simple equation was used to estimate $\Delta_{ET}G^0$ based on the excitation energy of the electron donor and the redox potentials of the electron transfer pair,[28]

$$\Delta_{ET}G^0 = e\left(E(D^{+\cdot}/D) - E(A/A^{-\cdot})\right) - E_{00} + \frac{e^2}{4\pi\varepsilon_0 r}\left(\frac{1}{\varepsilon_s} - \frac{1}{\varepsilon_s^{ref}}\right) - \frac{e^2}{4\pi\varepsilon_0\varepsilon_s R_{DA}} \tag{42}$$

where ε_s is the relative dielectric constant of the solvent used in the fluorescence measurements, ε_s^{ref} is the dielectric constant of the solvent used in the electrochemistry measurements, r is the average radius of the donor and acceptor, R_{DA} the donor-acceptor distance, E_{00} the excitation energy of the donor, $E(D^{+\cdot}/D)$ is the oxidation potential of the donor, and $E(A/A^{-\cdot})$ is the reduction potential of the acceptor.

The photoinduced electron transfer process is shown schematically in Figure 7 using the potential energy surfaces of the three states of P-L-P. The process of electron transfer will compete with the other excited state deactivation pathways. However, it does not result in a return to the ground state. Instead, a new charge separated species is formed. The process of charge recombination is generally thermodynamically allowed, and is in many cases also kinetically favorable (as seen in Figure 7). If charge

recombination is rapid, the system returns to the ground state donor-acceptor complex, and the charge separated species is only transient.
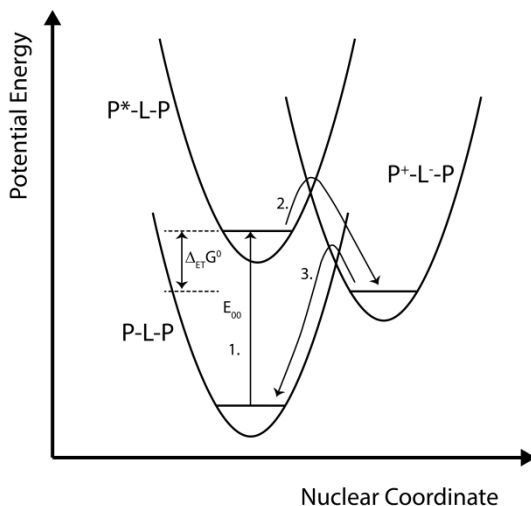

Figure 7. Potential energy diagram of the electron transfer process. (1.) The photoexcitation of the P-L-P complex resulting in P*-L-P, where the transition between the zero vibrational levels of the ground and excited state is shown. (2.) The electron transfer from the excited complex P*-L-P to the reduced ligand/oxidized porphyrin state P^+L^--P. (3.) Charge recombination resulting in the initial state P-L-P.

2.5   FLUORESCENCE MICROSCOPY TECHNIQUES

Fluorescence microscopy can be a very useful technique for investigating surface bound molecules/systems. However, the number of molecules which are being measured is much lower than in a bulk measurement. Therefore, all photons leaving the sample are commonly collected at the detector, as opposed to measuring an emission spectrum, in order to obtain a decent signal to noise ratio. Two microscope setups relying on confocal and total inter reflection fluorescence (TIRF) were used for the work presented in this thesis, and schematic diagrams of their optical setups are shown in Figure 8. Both aim to increase the resolution of the microscope by getting rid of light which is not in the plane of focus, compared to traditional fluorescence microscopy techniques. This decreases the background noise and increases the resolution of the microscope. The method of achieving this background reduction is fundamentally different for the two techniques, and will be presented below.
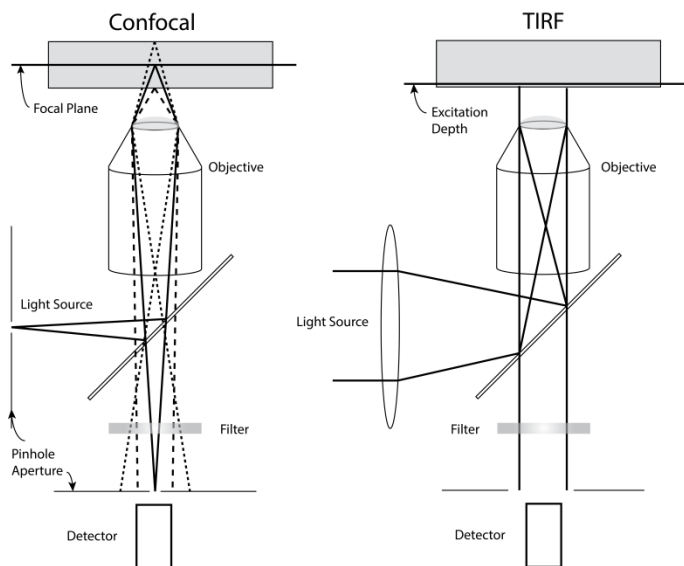
Figure 8. Schematic diagram of the optical setups used in Confocal and TIRF microscopy. For confocal microscopy a spot with smallest possible dimensions is illuminated. A pinhole aperture located in front of the detector ensures that mainly fluorescence from the focal plane is measured. In this way out of focus fluorescence is removed (as shown by dotted and striped lines). An image is generated by rastering the spot across the focal plane. For TIRF microscopy a large area is illuminated under total internal reflection conditions. In this way an evanescent wave is created at the interface between the oil from the objective and the substrate. This ensures that only fluorophores in close proximity to the surface are illuminated.

2.5.1   CONFOCAL MICROSCOPY

There are two key features which allow for the increased resolution for laser scanning confocal microscopy (LSCM). These are two pinhole apertures, placed before and after the sample. The laser path and optical setup is shown in Figure 8. Laser light passes through the first aperture and illuminates a very small volume of the sample, preferably near the diffraction limit. The fluorescence will originate mainly from the aforementioned volume, but the laser beam will also excite some molecules outside this volume. Since one wishes to only measure fluorescence from the confocal volume, the second aperture is used to again remove out-of-focus light. The confocal volume is then scanned in a plane, yielding a 2D intensity histogram or micrograph. The setup often allows easy movement of the setup in z direction, yielding the possibility of taking many plane micrographs and collecting them into a 3D image.

2.5.1.1   OBTAINING DIFFUSION COEFFICIENTS

Confocal microscopy is used in this thesis to study the diffusion of fluorescently labeled DNA constructs anchored to supported lipid bilayers via porphyrin moieties (papers 1 and 2). The laser is used to bleach a circular area of the micrograph, and the return of fluorescence to the bleached spot is related to the diffusion coefficient through Fick's second law.[29] To analyze the results a procedure termed the Hankel

transform is used and is implemented in a freely available Matlab™ program.[30] Briefly, this method has three steps. Firstly, uneven illumination is corrected for by flattening the illumination profile. Noise in the 2D image is then reduced by circular averaging around the center of the bleached spot, yielding a 1D intensity profile originating at the bleached area and projecting outwards. Finally, the intensity data as a function of distance from the bleached spot is converted to the spatial frequency domain using the Hankel transform, and fitted using the following equation,

$$F(k,t) = F(k,0)\exp(-4\pi^2 Dk^2 t) \tag{43}$$

where *F(k,t)* is the Hankel transformed data at time *t*, *F(k,0)* is the Hankel transformed at *t* = 0, *D* is the diffusion constant *k* is the spatial frequency and *t* is time.

2.5.2 TOTAL INTERNAL REFLECTION FLUORESCENCE MICROSCOPY

The operating principle of total internal reflection fluorescence microscopy (TIRFM) is fundamentally different from the LSCM technique (see Figure 8 for the optical setup). Firstly the whole image is collected simultaneously using a high-speed digital camera. A wide laser spot is reflected on the glass surface of the sample under total internal reflection conditions. This produces an evanescent field which penetrates around 200 nm into the sample. It is this field which is the excitation source. Since the evanescent field only penetrates a short distance above the surface, only molecules extremely close to the surface are excited. In effect, no background fluorescence originates from the rest of the sample. There are several ways to obtain the total internal reflection condition. For the work presented in this thesis, the objective is itself used to satisfy the TIRF condition. In general the sensitivity of TIRFM is greater than LSCM allowing for single molecule detection.

2.5.2.1 SUB-DIFFRACTION IMAGING

In this thesis TIRFM is used to study the number of single DNA origami constructs anchored to hydrophobic surfaces via porphyrin moieties (paper 4). The constructs displayed strong binding to the surface allowing an analysis of the relative positions of several fluorescent dyes on the origami, below the diffraction limit of the microscope. This information could subsequently be compared to the expected distances between the fluorophores as obtained from a model of the origami generated by the SARSE program.[31] The method employed for sub-diffraction imaging is termed direct stochastic optical reconstruction microscopy (dSTORM).[32, 33] The method requires that only a single fluorophore per construct is emitting at a time. If this is the case the point spread function generated by an emitting fluorophore can be fit to a Gaussian profile, and the peak position recorded. This procedure is repeated multiple times, where the emitting fluorophore can vary between each pass, and the peak positions are recorded in a 2D histogram. The histogram will contain peaks where the positions obtained from the Gaussian fitting are similar. If the number of events and signal to noise ratio is large enough the 2D histogram will reveal the relative positions of the fluorophores as peaks. To obtain the exact position the histogram data is also fitted to 2D Gaussian functions.

2.6   SURFACE ANALYTICAL TECHNIQUE: QCM-D

Although detection of the fluorescence from single molecules on a surface is possible, and even performed in this work, it is difficult to measure accurate fluorescence spectra of surface bound molecules. Instead, microscopy techniques are most useful for detecting the presence and position of surface bound molecules, but not their environment or number. To study surface bound DNA structures in greater detail we instead turned to surface analytical techniques and quartz crystal microbalance with dissipation monitoring in particular (QCM-D). QCM-D is a gravimetric technique which can yield the adsorbed surface mass as well as information on the viscoelastic properties of the formed surface films, through the real-time measurement of two parameters as shown in Figure 9.[34-36] A QCM-D system consists of an AT-cut quartz crystal between two gold electrodes. The quartz is a piezo-electric material and when an alternating potential field is applied over the electrodes, the crystal will deform in the shear mode. The resonance frequencies of the different overtones of shear mode oscillation are given in equation 44,

$$f_n = \frac{nv_q}{2t_q} \tag{44}$$

where n is the overtone number and only odd overtones produce standing waves, v_q is the speed of sound in the crystal and t_q is the crystal thickness.
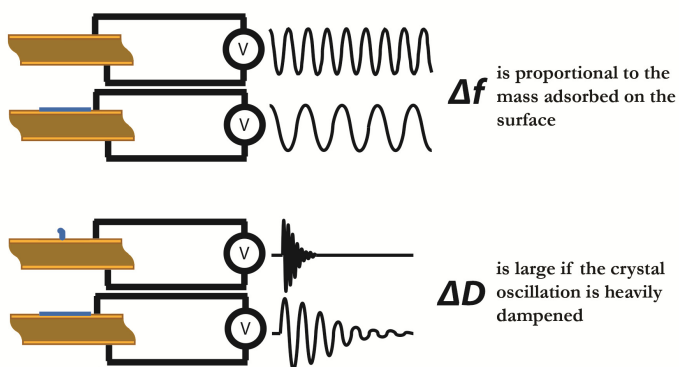

Figure 9. Illustration of the operating principle of QCM-D. The top panel shows that the resonance frequency of the crystal decreases ($\Delta f < 0$) as mass adsorbs to the sensor surface. The bottom panel shows that adsorbed films which couple weakly to the oscillation rapidly dissipate energy (high values of ΔD) when the alternating voltage is switched off, whereas films which couple strongly to the oscillatory motion dissipate energy slower (low ΔD values). Adapted with permission from Laura DeBattice.

For the QCM-D measurements performed in the work presented in this thesis one of the gold faces is coated with a layer of SiO_2 allowing for the formation of supported lipid bilayers on the surface (see section 3.3). Formation of supported bilayers or subsequent attachment of anchored DNA constructs results in shifts in the resonance frequency of the quartz crystal. This frequency shift is linearly proportional to the

change in mass adsorbed on the surface for the measurements performed in this thesis, as related through the Sauerbrey equation,[37]

$$\Delta f = -\frac{f_n}{n \cdot t_q \rho_q} \Delta m = -\xi \Delta m \qquad (45)$$

where Δf is the frequency change, ρ_q is the density of quartz, Δm is the adsorbed mass, and ξ is known as the mass sensitivity constant and has the value $17.7\ Hz \cdot cm^2/ng$ for quartz.

It should be noted that the SiO_2 face is immersed in aqueous solution for all the experiments performed in the work presented. Water molecules associated with the bilayer, and more importantly with DNA constructs, will also be affected by the oscillatory motion of the crystal. They will therefore also contribute to the measured adsorbed mass. For DNA the effect from such coupled water is very large, and ~90 % of the signal measured will be associated water.[35] There is an advantage to this hydration in that it eases detection by increasing the measured frequency-change signal 10-fold, thereby increasing the sensitivity. This is an important factor since QCM-D generally has poorer mass sensitivity than other surface analytical techniques such as surface plasmon resonance (SPR) or dual beam interferometry (DPI) which both rely on changes in refractive index of the surface upon adsorption.[38, 39]

To probe viscoelastic properties of surface films in addition to adsorbed mass, the second parameter measured using QCM-D, the dissipation (D), is needed.

$$D = \frac{1}{\pi f_n \tau} = \frac{E_{lost}}{2\pi \cdot E_{stored}} \qquad (46)$$

where τ is the dampened decay constant of the oscillation, E_{lost} is the energy lost during one oscillation cycle and E_{stored} is the total energy stored in the oscillation. Experimentally D is obtained by switching off the alternating potential over the crystal and measuring the decay of the oscillation.

D is not directly related to the viscoelasticity of the film, but the ratio $-\Delta D/\Delta f$, sometimes referred to as the acoustic ratio, can be used to evaluate the viscoelastic properties in a qualitative sense,[36, 40] and this qualitative approach is used in this thesis. Generally a high value of $-\Delta D/\Delta f$ yields a low modeled effective viscosity of the layer, if a Voigt based viscoelastic model is used.[41] For viscoelastic films, i.e. films with a high value of $-\Delta D/\Delta f$, the linear relationship between Δm and Δf breaks down, and the mass becomes underestimated. In these cases viscoelastic modeling is necessary to get an accurate estimate of the bound mass. To qualitatively compare the viscoelastic properties of adsorbed films using QCM-D, a plot of ΔD vs. Δf can be made, termed a ΔD - Δf plot in his thesis. In this way the dissipation change is followed as the frequency changes. Viscoelastic differences in the two films will manifest in different values of dissipation change as the frequency changes.

To illustrate the use of the acoustic ratio we can consider the formation of supported lipid bilayers on SiO_2 surfaces. To distinguish a layer of adsorbed liposomes from a correctly formed supported bilayer is notoriously difficult using optical mass-sensitive

techniques such as SPR. However, large differences in acoustic ratio are obtained using QCM-D since the supported bilayer is a relatively stiff film which couples well to the motion of the crystal. It therefore displays a low dissipation, whereas the liposomes are soft deformable spheres which couple poorly to the crystal motion and rapidly dissipate energy.

3   SELF-ASSEMBLED COMPONENTS

In this section the various structural components used in the work presented in this thesis are introduced. A common theme for these is that self-assembly determines their interactions and structure in buffered solution. DNA itself is a self-assembling molecule, and functionalization can be achieved through covalent bonding and non-covalent interactions. Non-covalent interactions are themselves a form of self-assembly, and the covalent modifications can bestow further self-assembled surface binding properties to the DNA. These aspects will be presented followed by a description of phospholipid bilayers, the surface we have mainly employed for the attachment of DNA, and a beautiful example of self-assembly in its own right. Finally, work on the attachment of DNA to lipid bilayers is presented, focusing on previous work from our group using a porphyrin anchor. This work directly leads to the original work presented in this thesis.

3.1   DNA

"As with any craft material, the structural applications of DNA are limited only by the imagination" – Nadrian C. Seeman

To utilize the full potential of DNA as a structural material as suggested above by the founder of the field of DNA nanotechnology, a detailed understanding of the structure of DNA itself is necessary. This section will start by considering the structure and components of DNA, and how these have been exploited in the field of DNA nanotechnology. This will be followed by considering how DNA is functionalized for the work presented in this thesis.

3.1.1   DNA STRUCUTURE

The double helical structure of DNA, as shown in Figure 10B and C, has been known since the pioneering work by Watson and Crick,[42, 43] making DNA one of the most recognizable molecules known to the public. With a diameter of ~2 nm and a length between 2 nm (a few base-pairs) and 230 m (670 billion base-pairs from *Polychaos dubium*),[44] DNA is truly a remarkable versatile molecule. A duplex is composed of two single strands connected by hydrogen bonds (see Figure 10A and B). Each of the single strands consists of a repeating negatively charged sugar-phosphate backbone and attached deoxyribonucleoside bases which are positioned perpendicular to the backbone direction. Each nucleobase attaches to its neighbor from the 5' position of its adjoining ribose sugar, to the 3' position of the neighboring ribose via a phosphodiester bond (Figure 10A). Single stranded DNA thereby has an inherent direction, and the sequences of DNA bases in a strand are generally written from the 5' to 3' ends.

There are four naturally occurring DNA bases; guanine (G), cytosine (C), adenine (A) and thymine (T), each displaying a unique hydrogen bond pattern (see Figure 10A). In this way G on one strand can pair with C on a complementary strand through 3 hydrogen bonds, and A can pair with T through 2 hydrogen bonds. For two single

strands of equal length to form a stable duplex, two requirements have to be met. The first is that the hydrogen bonding pattern of one strand must match the other. The second is that the direction of each strand must be anti-parallel to each other, meaning that the sequence 5'-GCAT-3' will pair with the sequence 5'-ATGC-3'.
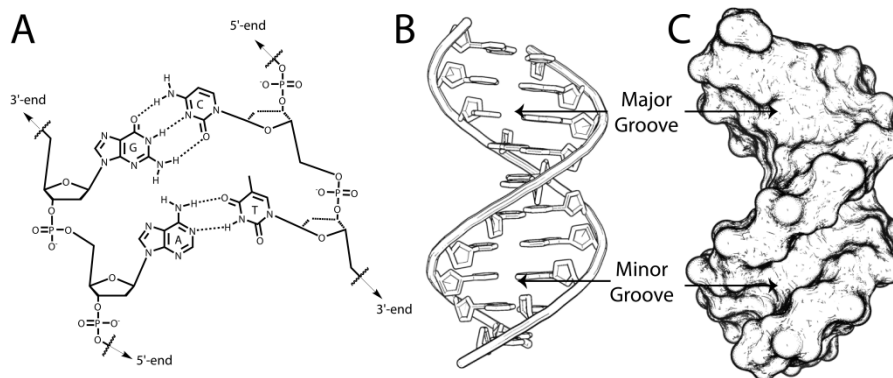

Figure 10. (A) Hydrogen bonding pattern of the DNA nucleobases and backbone attachment stereochemistry. (B) Schematic representation of B-DNA helix conformation including backbone and bases, with the major and minor grooves highlighted. (C) Schematic diagram of the surface of DNA where the grooves are more evident.

Under physiological conditions, duplex DNA adopts what is known as a B-form conformation, a right-handed helix with a helical pitch of 10.5 bases (number of bases needed for a complete turn), a helical twist of 36° per base, and a rise of 3.4 Å (distance between neighboring base-pairs).[45-47] Once formed, a DNA duplex displays two groves, due to asymmetry in the two backbone positions. The emergence of the grooves is best visualized by looking at a single base-pair of DNA along the long axis of the duplex, so that the DNA resembles a circle. The angle between the two backbone attachment points of the bases is then not 180°, but rather ~110° on one side and 250° on the other. The larger of the two angles forms the major groove, which is 11 Å wide, with a depth of 4 Å, whereas the minor groove is only 6 Å wide, with a similar depth of 5 Å, as shown in Figure 10C.[48]

There are large differences between the structural properties of DNA in single and double stranded form. Duplex DNA is relatively stiff, with a persistence length of roughly 50 nm,[49, 50] whereas the persistence length of single stranded DNA is only a few nanometers.[51] The stiffness of duplex DNA makes it ideal as a structural material. The thermodynamic stability of DNA duplexes is governed by the ability of the two single strand components to form hydrogen bonds. Therefore, matching sequences are much more stable than sequences with mismatched bases. Longer sequences also tend to be more stable, since the number of hydrogen bonds increases. This factor is also present in the content of the bases. DNA with higher GC content is more stable due to more hydrogen bonds. Duplex stability is further governed by the presence of positively charged ions in solution. The ions reduce the Coulombic repulsion between the two negatively charged backbones, with divalent ions showing markedly higher stabilization than monovalent ions. Hydrophobic and π-π stacking interactions

between neighboring base-pairs, known as base stacking, also increase the stability of the duplex. The stability of a DNA duplex can be measured through its melting temperature, defined as the temperature at which half of the duplexes have denatured into single strands. This characteristic is accessible through UV absorption melting curves.

3.1.2   STRUCTURAL DNA NANOTECHNOLOGY

The field of structural DNA nanotechnology aims to use DNA as a structural material, utilizing insights gained from a detailed knowledge of DNA structure. The field started in the early 1980s as thought experiments on how to use DNA to form repetitive crystals in order to co-crystallize proteins.[52-56] This would in turn allow for the structural determination of the proteins using X-ray diffraction. This motivation, and how it helped to evolve the field into what it has become- a field with a myriad of DNA building blocks of various shapes, sizes and functionalities- is a good starting point for understanding the use of DNA nanotechnology in this thesis. In particular it will lead to structural aspects of DNA origami, which is employed in paper 4. There are several excellent reviews of the field available, and a few are listed here for the interested reader.[4, 57-63]

There are two key features of DNA which instigated the advent of DNA nanotechnology. The first is that DNA does not need to be a simple linear molecule as described in section 3.1.1. During genetic recombination, in which two identical DNA duplexes swap single strands, the four-branched Holliday junction structure is found as an intermediate.[64] Since the four strands of a Holliday junction are pair-wise identical, the crossover point can freely move (called branch migration), while still keeping the same number of base-pairs. However, a stable crossover as a building block in DNA nanotechnology can be designed using four unique single strands, as shown in Figure 11A, creating a junction with four protruding duplexes. The bases of the four strands have been color coded so that complementary stretches have the same color. The second feature is the principle of "sticky-end" cohesion, which is used to couple DNA components together (Figure 11B).[65] This simple principle relies on the hybridization of matching single-stranded overhangs, one on each of the structures one wishes to join together. An overhang is created if two strands of a duplex have differing lengths. An important detail of this principle is that the joined overhangs also adopt a B-form helical structure.

It was quickly realized that a single crossover between two DNA duplexes, as found in the Holliday junction lacks the stability necessary to act as a building block for repetitive patterns. Instead, several crossovers were included to rigidify the structure. A wide range of such strongly coupled duplexes were created, [66-69] and many were shown to form 2D repeated patterns on surfaces.[70, 71] The difference between the various structures is a consequence of the number and positioning of crossovers, the number of coupled duplexes, and the relative direction of coupled duplexes. For example, to couple two DNA duplexes placed side by side, crossovers can be placed wherever two backbones from opposing duplexes meet (see Figure 11C and D). Furthermore, each double-helical domain has a direction, as shown in the figure where the strand ends

have been colored to denote direction. It was shown that crossovers between anti-parallel duplexes were more stable than their parallel counterparts.[72] There are five isomers of DNA double crossovers, two for anti-parallel helices and three for parallel helices. For DNA, possible crossovers will appear every half turn of the helix, which translates to every 5.25 base-pairs. To reach an integer number of base-pairs between the two duplexes, crossovers could be placed with a spacing of 21 base-pairs (4 half turns of DNA) to minimize torsional stress in the structure.
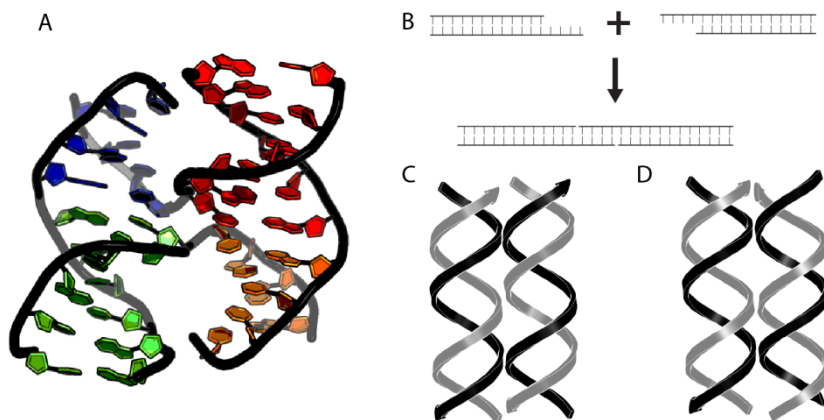

Figure 11. (A) Schematic drawing of a stable Holliday junction in solution. Bases which hydrogen bond to each other have been given the same color. Made using pdb file 3IGT. The solution structure is not tetrahedral as one might expect, but rather resembles two parallel helices with a crossover. (B) Schematic diagram of DNA "sticky-end" end cohesion. Two DNA duplexes with complementary single stranded overhangs hybridize to form a single structure. (C) Two anti-parallel duplexes in close contact, possible crossover points appear every half turn of the DNA helix. (D) Two parallel duplexes, possible crossover points appear every half turn of the DNA helix. In (C) and (D) the strand directions are marked by arrows.

Parallel to the attempts at creating large repetitive arrays of DNA tiles was the idea of building small unique structures of DNA which could subsequently join to form larger *non*-repetitive structures. Many small structures were attempted, including the design and characterization of a DNA hexagon with 6 unique sides of 10 base-pairs length each (see Figure 12).[73-75] This structure is used as a component in paper 2. For such a structure there are more than 1 million unique sides possible (4^{10}), and each can in principle be addressed.[76] However, measurements and calculations revealed that connecting several such components into larger structures requires extreme control of single strand stoichiometry and sample purity, and is not feasible.[77, 78] Instead DNA origami emerged as a viable alternative for creating relatively large non-repetitive structures.
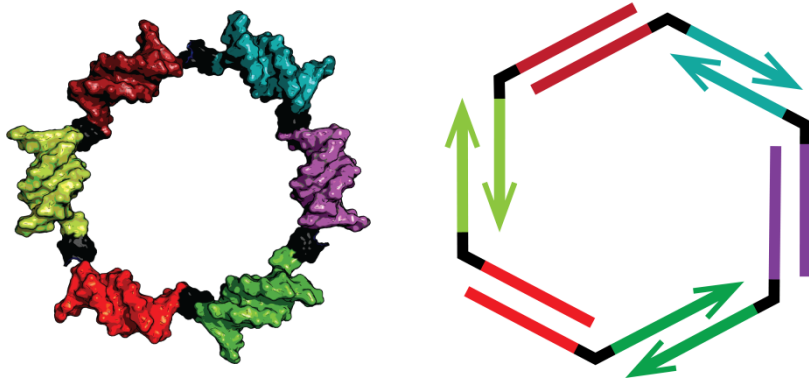
Figure 12 DNA hexagon motif used in an attempt to build large DNA structures from smaller unique modules.[73-75] Each side of the hexagon is 10 base-pairs in length and the structure is color coded to reflect that the sequence of each side is unique. Connecting each side is a pair of un-base-paired thymines, which help to give the structure conformational flexibility. On the right is shown the 6 component single strands of the structure, and how they hybridize to form the ring-closed hexagon.

3.1.3   DNA ORIGAMI

A huge breakthrough in structural DNA nanotechnology arrived with the concept of DNA origami. As mentioned, creating ever larger non-repetitive structures by connecting a multitude of single strands becomes increasingly difficult as the number of strands increases. Entropic effects always tend to beat out the formation of the desired structure. To overcome this, the idea of employing a scaffold strand to increase the possible size of DNA objects was born. Here, one of the strands in the structure is extremely long, and all other strands assemble by base-pairing to this strand (Figure 13A).
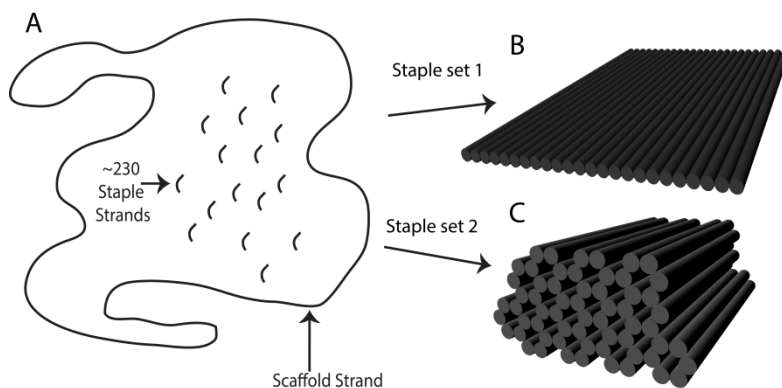

Figure 13. (A) The principle of DNA origami. A large viral single strand is annealed with a number of staple strands to form unique structures in (B) 2 dimensions or (C) 3 dimensions. It is the sequences of the staple strands which determine the final structure formed.

One of the first examples of a scaffold strand used in this way is Shih's work to create a 3.4 kilobase octahedron.[79] This quickly led to the work of Rothemund, and the first example of DNA origami.[80] For DNA origami, a naturally occurring virus strand is used as the scaffold. Different stretches of this long single strand are brought into close contact by hybridization with a short "staple" strand. 230 such staple strands come together to form the final structure. The scaffold strand is in this way folded back and forth unto itself, to fill the desired pattern. Depending on which sequences the staple strands have, different stretches of the scaffold are joined, thereby forming different structures (Figure 13B and C). This means that every 2D structure needs a specific set of staple strands with the correct sequences, otherwise the structure will not form. This allows for the creation of virtually any 2D shape with dimensions of roughly 100 nm × 100 nm. Each fold in the scaffold requires a series of crossovers to hold the two neighboring duplex stretches together. In the original 2D origami approach, crossovers between neighboring duplexes appear every 32 bases (slightly shorter than 3 turns of DNA). One duplex thereby has crossovers every 16 bases, first with the duplex below, then 16 bases further along with the duplex above. Neighboring helices are anti-parallel to increase stability as discussed in section 3.1.2. Since the distance between crossovers is not an integer number of half-turns of DNA, there is an inherent tension in the structure. Some of this tension is alleviated by including crossovers with opposing tension, yet the 2D origami rectangle used in paper 4 still adopts a curved instead of flat conformation in solution.[81] The formation of a 2D DNA structure entails a large amount of repulsion due to the proximity of neighboring negatively charged helical domains. This is overcome either by the addition of roughly molar amounts of Na^+ or ~10 mM Mg^{2+}.[80, 82]

Soon after the first example of DNA origami, other groups were quick to bring the concept into a 3D world. The first example was a box with a controllable lid, folded together on a single scaffold strand.[83] Each side of the box is flat 2D origami, meaning that the box is empty. The next important step for the field was the creation of "filled" 3D origami shapes. The principle is very similar to 2D origami, but the design is slightly different. 2D origami can be considered as a row of neighboring duplexes, where the height of each duplex determines the final shape (Figure 13B). 3D origami extends this concept by building origami not as a row of helices, but instead as an array of helices (Figure 13C). Several different arrays have been proposed, including square and hexagonal.[84, 85] Again, the shape is filled by the folding of a single scaffold strand, but crossovers are now placed between neighboring helices with a spacing of 21 bases (an integer number of helical half turns) for the hexagonal and 32 bases for the square array. By tuning the distance between crossovers to induce strain, twisted and curved 3D origami structures have been created. [86, 87] Due to the increased proximity of DNA duplexes and thereby strand repulsion, 3D origami structures generally require higher concentrations of counter-ions to form stable structures.[82]

As a final comment it is noteworthy that relatively large and complex structures have been formed solely by using small single stranded components, without the use of a scaffold strand. [88-90] This possibility is surprising due to the entropy effects described above, yet it seems that the formation of the structure is self-catalyzing in this case, making the desired structure kinetically more likely to form. Although the yields using

this approach are generally lower than for origami, it has the advantage that new sets of staple strands are not needed for each new structure. Instead a pool of unique stable strands can form a 3D cube in solution. Other structures are formed by removing strands from the pool before annealing. This principle is similar to the construction of marble statues where a desired form is created by chiseling away elements from an initial marble block.

3.2 FUNCTIONALIZING DNA

To give examples of all the possible functionalities imbued in DNA over the years is beyond this thesis. Instead, relevant modifications for the work presented in the papers will be considered.

3.2.1 FLUORESCENT DNA BINDING DYES AS LIGHT HARVESTERS

One of the simplest ways to functionalize DNA is by using DNA binding dyes to form self-assembled dye-DNA structures. Many of these dyes have been developed for labeling DNA inside cells for imaging purposes, or as quantifiable markers for electrophoresis.[91-94] There are generally three types of self-assembled dye-DNA interactions, which depend on the structure and size of the dye used. Some dyes tend to bind in either the minor or major grooves of DNA, although minor groove binding is more common for small organic molecules. These dyes often have the added bonus of sequence specific binding, which has the potential to be exploited for technological purposes, by allowing the specific positioning of different dyes along a stretch of DNA. In the work presented in this thesis dyes which self-assemble by binding between neighboring base-pairs of a DNA duplex were used, and this section will focus on the dye YO (YO-PRO-1) and its homo-dimer YOYO (YOYO-1), see Figure 14.[95] This binding mode is known as intercalation, and results in a structural change of the DNA to accommodate the invading dye. The chemical structure of YO and YOYO, as well as a solution NMR structure of the bis-intercalating dye TOTO bound to DNA are shown in Figure 14.[96] The binding of TOTO to DNA is expected to be very similar to that of YOYO. Intercalating dyes tend to be positively charged, and often stabilize DNA due to a reduction in strand repulsion and additional base stacking.

YO and YOYO were primarily developed as labels for electrophoresis,[97, 98] and the properties which make them suitable for this are strong binding to DNA and large oscillator strength, which also make them excellent candidates for light harvesting components. This use of the dyes is explored in papers 3 and 4. The structure and function of natural light harvesting antennae is presented in section 4. Briefly, a protein scaffold holds dye molecules at specific orientations and distances. The dyes have extremely high oscillator strengths, thereby allowing effective homo-FRET energy transfer (section 2.4.3). Intercalation of YO and YOYO results in an extension of the DNA by roughly the distance between two base-pairs (3.4 Å) per chromophore and unwinding of the helix by 26°. The chromophores bind with nearest neighbor exclusion, meaning that the distance between neighboring chromophores in DNA is 9.4 Å, based on the NMR structure of TOTO-DNA. The distance between

neighboring dyes in DNA is thereby comparable to the distance between chlorophyll molecules in the highly ordered light harvesting antennae LH1 and LH2 described in section 4.1, and intercalating dyes thereby represent interesting candidates for DNA based antenna complexes.
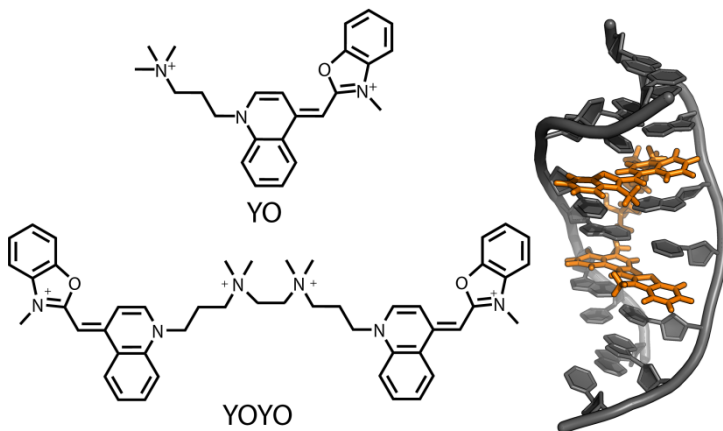

Figure 14. Chemical structure of the intercalating dye YO, and its bis-intercalating homo-dimer YOYO. To the right is shown the solution nuclear magnetic resonance (NMR) structure of the bis-intercalating dye TOTO bound to DNA. Unwinding and extension of the helix are clearly observed. Figure on right was made using pdb file 108D.

When bound to DNA the dyes display a 1000-3000 fold increase in fluorescence quantum yield due to a reduction in internal rotational motion.[95, 99] This has practical importance in that it eases fluorescence measurements, since unbound dyes aren't observed. The lifetime of the dyes also increases upon intercalation and reaches 3 ns, similar to chlorophylls in natural light harvesting systems. The absorption coefficient of each monomer is ~50 000 $M^{-1}cm^{-1}$ and the quantum yields are relatively high, making these dyes very bright. The close distance between dyes and spectral overlap between emission and absorption mean that homo-FRET between the dyes is effective. Another important aspect is the binding strength. The monomer association constant is roughly 10^6 M^{-1},[100] yet increases to ~10^{10} M^{-1} for the dimer.[101] The binding strength is dependent on the concentration of other positive ions in the solution, where a high concentration decreases the binding constant dramatically.[100] This is an especially important factor for DNA origami applications, where high ionic strength is needed for structure formation. In these cases, the dimer is more suitable to use than the monomer, as we demonstrate in paper 4.

3.2.2 COVALENT DNA MODIFICATIONS FOR DETECTION AND SURFACE ANCHORING

In addition to the many structures described in sections 3.1.2 and 3.1.3, there is another technological advantage which makes DNA interesting as a nano-scale construction material. This is the ability to covalently functionalize DNA by organic chemistry means. For example, each DNA origami staple strand is synthetically made and can be

modified in various ways, allowing for 230 unique strands each with modifications in predefined positions.

A relatively standard modification is the use of fluorescent dyes to label DNA. In this thesis fluorescent modifications are used to measure the placement of DNA structures on surfaces (paper 4), to determine the diffusion coefficients of DNA structures bound to lipid bilayers (papers 1 and 2), and as terminal acceptors in light harvesting complexes (paper 4). Many dye classes are commercially available, allowing a high level of control and tailoring of spectroscopic properties.

To date most work on DNA structures has been conducted in buffered solution. Although this is a great starting point for DNA nanotechnology, integration with existing technology will need surface attachment of the DNA. A few strategies for surface attachment are presented below; however, they often rely on strong coupling between the DNA and surface, yielding a static DNA structure. We wish to attach DNA to surfaces, yet in a fashion which keeps the DNA in as native a state as possible, as if it were in solution. Such surface attachment is considered in papers 1 and 2, and requires covalent modification of the DNA.

It is in many cases possible to attach DNA to positively charged surfaces without modification through Coulombic interactions, due to the overall negative charge of the DNA backbone. For example, charge inversion at highly negatively charged surfaces using Mg^{2+} has been employed to deposit DNA origami on plasma etched oxide.[102, 103] Another possibility is the use of positively charged self-assembled monolayers to form positively charged surfaces for DNA attachment.[104, 105] This is often sufficient for imaging purposes, but there are several drawbacks to this approach if other uses of the DNA are desired. Generally the DNA interacts so strongly with the surface that hybridization is hindered, making the DNA devoid of its inherent self-assembly properties. Covalent modifications of DNA can instead be used to remove the necessity of strong interactions between the DNA and surface. Instead it is the modification which interacts with the surface, potentially leaving the DNA in its native state.

Covalent modifications of DNA for surface attachment have mainly been explored for DNA sensor array applications. The interaction between gold surfaces and thiolated DNA has been the main method employed in this regard.[106-109] However, this technique generally positions the DNA perpendicular to the surface, something which is detrimental to many surface based applications. Furthermore, the surface density of DNA influences the rates and efficiencies of hybridization, and single stranded DNA can still interact slightly with the surface. Another such strategy relies on biotinilated DNA to attach to streptavidin modified surfaces, again with the DNA in a perpendicular arrangement to the surface.[35] Another drawback of these methods is that the structures are static on the surface, as they cannot be moved once they are bound. Recently, attachment of DNA to lipid surfaces has been shown using hydrophobic anchors consisting of lipid,[110, 111] cholesterol,[112] or porphyrin(see Figure 15).[113, 114] Lipid surfaces are generally dynamic in the sense that they behave as fluids with diffusing lipid components, and this mobility is conferred to anchored constituents.
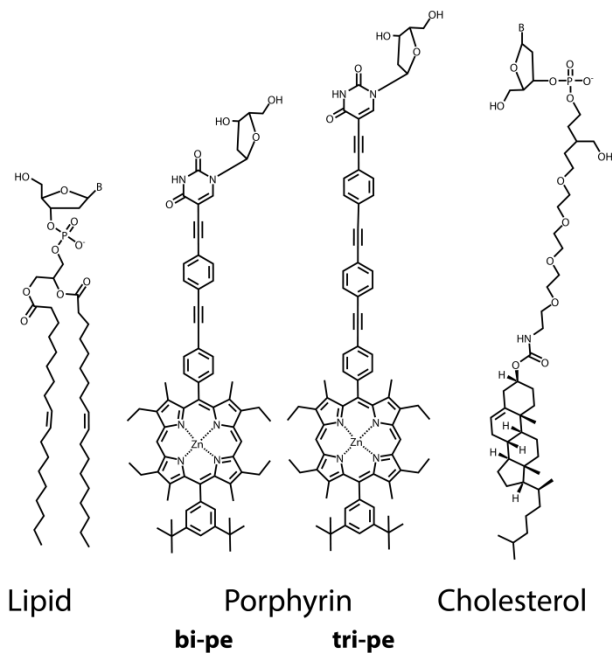
Figure 15. Chemical structure of two common covalent hydrophobic DNA modifications (lipid and cholesterol) and the two porphyrin anchors used in this thesis. The lipid anchor shown is based on DOPC where the DNA replaces the choline group. The porphyrin modifications used in this thesis are shown as their thymine nucleosides as zinc-porphyrins. The same anchors in free-base form are also used in this work. The length of the linker connecting the DNA to the porphyrin varies between two (**bi-pe**) and three (**tri-pe**) phenylethynylene units. On the right is shown a cholesterol anchor which functions similarly to the porphyrin anchor, although the binding strength to bilayers is weaker for the cholesterol.

In papers 1 and 2 porphyrin modified DNA is attached to lipid bilayers. An advantage of the porphyrin anchor (shown in Figure 15) compared to the cholesterol anchor is that the binding to the bilayer is much stronger, and that the porphyrin itself is a functional molecule able to partake in electron transfer reactions as explored in paper 5. The function and structure of self-assembled lipid bilayers is given below, followed by a description of systems wherein DNA is anchored to lipid bilayers. This latter part will focus on attachment schemes employed in our group, which lead to the original work presented in this thesis.

3.3   PHOSPHOLIPID BILAYERS

Many of the envisioned technological applications based on phospholipid bilayers derive from the biological role these structures play. In essence the bilayer acts as a container for cellular components, but also as a substrate for the organization of biological machinery in the form of proteins, for example for light harvesting and signal transduction. The latter is interesting as the bilayer functions as a node for communication between the cell and the extracellular environment. Similarly one could envision supported bilayers acting as substrates for communication between fluid

solutions and existing surface based technologies, mediated by functional DNA nanostructures. In the cell, organization of multi-protein units is mediated by the bilayer. The constituent lipids are mobile, and the 2D surface ensures diffusion behavior different from bulk, and allows higher concentrations of reacting species. Similarly one can envision the surface mediated step-wise organization of DNA origami building blocks, a goal within current DNA nanotechnology.[58]

Model lipid membranes are generally used in technological applications due to their simplicity of formation, well defined properties, and the inherent control over constituents they afford. They often consist of a single lipid constituent, and the phospholipid DOPC is used for the work presented in this thesis (chemical structure shown in Figure 16A). Phospholipids are amphiphilic molecules consisting of a polar headgroup and hydrocarbon tail. DOPC and many other lipids will spontaneously form bilayer structures in solution, to minimize interactions between the hydrophobic part and the aqueous environment. Other solution structures of lipid aggregates such as micelles exist, and the structure formed generally depends on simple size parameters of the lipid head-group and tail.[115, 116] DOPC dissolved in water will generally form particles with a distribution of sizes, composed of multiple layers of lipid bilayers, known as multilamellar vesicles. To increase the uniformity of the system, a technique known as extrusion is used to form spherical uni-lamellar vesicles (liposomes, Figure 16B). Liposomes can in turn be used for the spontaneous formation of supported lipid bilayers (Figure 16C). Generally hydrophilic surfaces such as SiO_2 facilitate this formation.[117-125] Lipid bilayers of DOPC are ~5 nm in height as measured by atomic force microscope.[126-128] In the case of the supported bilayer, there is an interstitial water layer between the bilayer and the surface, which is ~1-1.5 nm thick.[129-131]
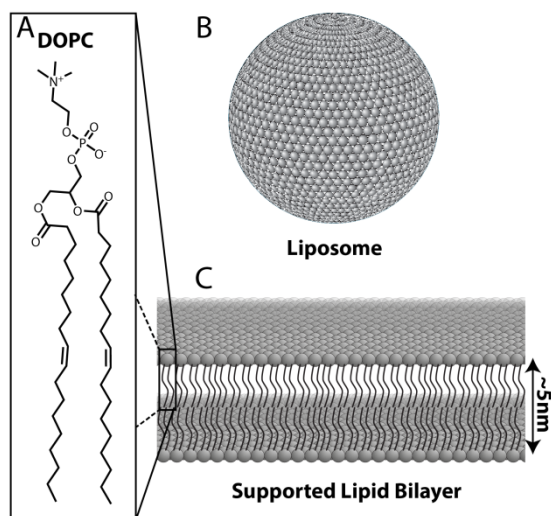

Figure 16. (A) The chemical structure of the lipid DOPC used in the work presented in this thesis. Also shown are self-assembled DOPC bilayers in the form of (B) a liposome consisting of a spherical bilayer with a cavity and (C) a supported lipid bilayer.

By incorporating other lipid types the structural properties of bilayers can be varied. For example, DOPC is in a fluid phase at room temperature allowing rapid diffusion of lipids. By increasing the length of the hydrocarbon chain, the phase transition temperature is changed, and gel phase lipids with greatly reduced lateral mobility can be formed.[132] Furthermore, lipids can be covalently modified much like DNA itself, allowing the bilayer to become a functional component of the system instead of a basic surface used only for anchoring. The lipid membrane constitutes a colloidal phase of hydrocarbon wedged between polar groups. In this way small hydrophobic molecules can partition into the bilayer, and potentially react with functional components placed on the DNA. This avenue is explored in paper 5.

3.3.1   DNA ANCHORED TO BILAYERS

Anchoring of DNA to bilayers through covalently modified hydrophobic groups is again an example of self-assembly. For example, porphyrin-DNA is an amphiphilic molecule and membrane binding results from the hydrophobic effect, whereby the porphyrin anchor avoids contact with the aqueous solution. The same effect is observed for cholesterol-DNA. Cholesterol anchors have been used for the attachment of DNA to bilayers, revealing that much stronger binding is observed using two anchors instead of one.[112, 133] Bi-cholesterol anchors on DNA have subsequently been employed to mimic the functioning of SNARE proteins, which mediate vesicle fusion to the cell membrane during exocytosis.[134-137] Cholesterol anchors have furthermore been used to bind hexagonal DNA structures similar to those presented in section 3.1.2.[138] Also DNA origami structures have been anchored to lipid bilayers.[139, 140] A very recent report showed the reversible formation of DNA origami dimers on mobile lipid bilayers using UV and visible light irradiation.

Porphyrins are less used as membrane anchors compared to cholesterol, yet have certain advantages. The larger hydrophobic area of porphyrins facilitates a stronger binding to the bilayer compared to cholesterol. Recently, a DNA based membrane pore, anchored to a supported phospholipid bilayer using porphyrins was demonstrated.[141] In our group DNA was anchored to liposomes via a porphyrin anchor, and the effect of linker length, number of porphyrins (Figure 17), and energy transfer to the porphyrin were investigated.[113, 114] The last is an important factor, which differentiates porphyrin anchors from for example cholesterol. The porphyrin is a chromophore absorbing light in the visible range, and can further act as an excellent electron donor in its excited state. This means that the porphyrin is a functional component able to perform photochemical reactions at the surface. It was further shown that the linker length between the DNA and porphyrin is important for reversible hybridization of liposome attached DNA. If the linker length is a single phenylethynylene unit, hybridization as examined through DNA melting curves and FRET measurements is hindered. However, linker lengths of two or three phenylethynylene units allowed the DNA to reversibly hybridize. The length of the DNA is also important. Longer DNA increases the solubility of the amphiphilic porphyrin-DNA molecule in buffered solution. It was further shown that the saturation density of anchored DNA on the liposome surface varied with the number of anchors. Two anchors showed lower binding density compared to one, indicating

that the second anchor helps to align the DNA in a perpendicular orientation compared to the bilayer surface. By attaching a fluorescent donor molecule to the DNA, energy transfer was measured, followed by an electron transfer to a membrane solubilized hydrophobic molecule. This functioning of energy transfer followed by electron transfer is similar to the functioning of light harvesting, and is further explored in papers 3 to 5. An introduction into light harvesting, and DNA based systems which mimic this process is given in section 4.
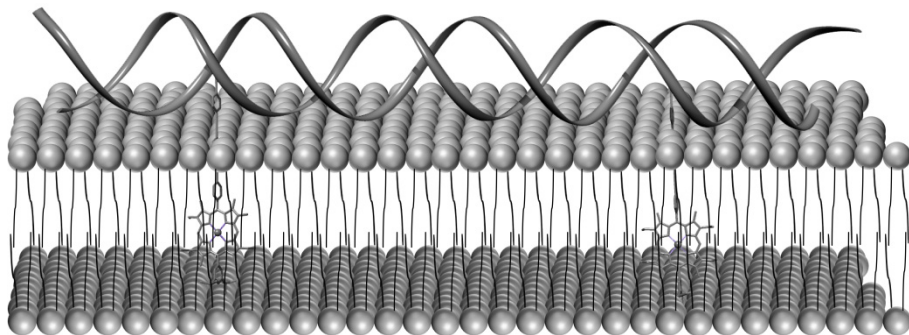

Figure 17. A model of a DNA duplex anchored to a liposomal membrane via two covalently attached porphyrin moieties. Each strand contains a single porphyrin, and it was shown that alignment to the liposome surface increased with two anchors compared to one.[114]

4   LIGHT HARVESTING

Any attempt to mimic nature requires an understanding of the underlying processes. In the case of photosynthesis, much work has been put into understanding the mechanisms which allow efficient and directed migration of energy, and a large portion of this is centered on available crystal structures of light harvesting complexes. Here, some general aspects of natural light harvesting will be discussed. The goal is to gain insight into the most important factors which allow the transfer of energy over large distances with high efficiency, in order to apply these to the artificial DNA based systems presented in papers 3 and 4. Furthermore, the structure of the electron transfer chain which allows the absorbed energy to be stored is of interest for the work presented in paper 5.

4.1   NATURAL SYSTEMS

The most heavily studied natural light harvesting systems are those of purple bacteria, due to the availability of high resolution crystal structures.[142-146] Well separated spectroscopic characteristics of their component dyes have also made them especially amenable to time-resolved photophysical characterization.[147, 148] As more crystal structures from various biological domains are being solved, the purple bacteria light harvesting system remains one of the most intuitive, and I have therefore chosen this as a primary example. The discussion is based primarily on the works of Schulten and Cogdell,[149-154] to which the interested reader is directed.
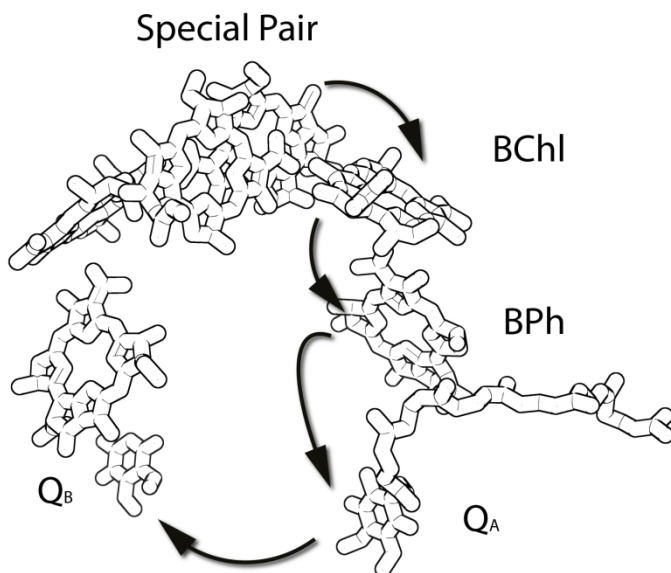

Figure 18. Main electron transport pathway from photoexcited "special pair" via BChl, BPh, and Q_A to Q_B in the reaction center of purple bacteria. Two reductions of Q_B occur before it leaves the system. Adapted from pdb file 1PYH.

The key element of photosynthesis is the reaction center (RC, shown in Figure 18). This is where energy is collected and temporarily stored through the reduction of a quinone Q_B to dihydroquinone. The reaction center consists of 4 chlorophyll molecules embedded in a protein matrix (the protein matrix is omitted for clarity), which itself is embedded in a phospholipid bilayer. Upon photoexcitation of the reaction center special pair (two electronically coupled chlorophylls in close proximity) an electron transfer chain reaction is activated. The first step is reduction of one of the remaining chlorophylls (BChl) which subsequently reduces a bacteriopheophytin (BPh) followed by reduction of a quinone (Q_A). The final step is the reduction of a loosely coupled quinone (Q_B) which can leave the system after two consecutive oxidations. The energy stored in the reduced quinone is used to maintain an energy gradient over the cell membrane.

Figure 19 shows the purple bacterial PSU consisting of the reaction center and two types of peripheral antenna complexes.[151] The first is known as LH1 and comprises 30 chlorophyll molecules in a protein matrix embedded in the phospholipid bilayer, arranged in an ellipsoidal formation around the central reaction center. Surrounding LH1 are several identical structures called LH2 which each contain two concentric rings of chlorophylls, also embedded in a protein matrix. The inner, compact, ring incorporates 18 chlorophylls ($LH2_I$), whereas the outer ring contains 9 ($LH2_O$). The ratio between LH1 and RC is always 1:1, whereas the ratio of LH2 to RC can vary depending on growth and light conditions,[155-158] ranging between 1:1 and 10:1. The protein matrix separates the dyes and prevents electron transfer reactions between them, which could otherwise result in unwanted photochemical reactions and thereby energy sinks.
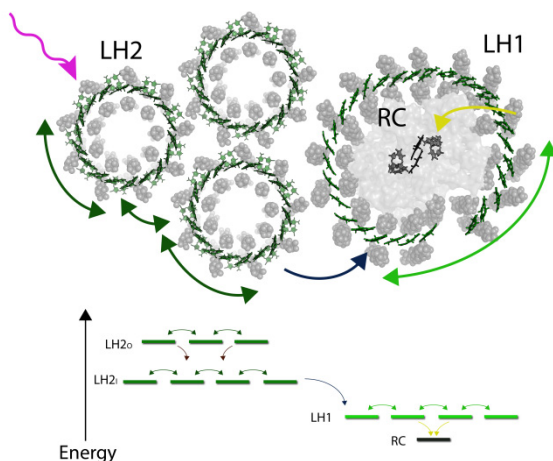

Figure 19. PSU of purple bacteria consisting of a RC, surrounded by the light harvesting antenna LH1. Surrounding LH1 are further antenna complexes (between 1 and 10 per RC) known as LH2. The system is embedded in a phospholipid bilayer in the plane of the paper, which is omitted for clarity. Chlorophyll pigments (green) are embedded in a protein matrix (gray). Excitation can occur on any pigment in the system and will travel to the reaction center via a series of homo-FRET (bidirectional arrows) and hetero-FRET (unidirectional arrows) energy transfer steps to the RC with 95 % efficiency. Lowe half of the figure shows the energy landscape of the various pigments, creating an energy gradient towards the RC. Made using pdb files 1PYH and KZU.

The chlorophyll molecules in each ring differ only in their connections to the protein matrix, and their excitonic coupling, giving rise to slightly shifted spectra in the three rings. The chlorophylls display very high absorption coefficients of $\sim 1\text{-}1.5 \times 10^5$ $M^{-1}cm^{-1}$ indicating large dipole strengths (see section 2.3),[159] and relatively long singlet excited state lifetimes of ~ 1 ns.[160] Furthermore, the Stokes shift (energy difference between absorption and emission) is small. This is a very important factor which means that there is spectral overlap between the emission and absorption spectra of these dyes, allowing effective homo-FRET transfer. In $LH2_I$ and LH1 the chromophores are electronically strongly coupled, with parallel aligned transition dipoles and a dye to dye spacing of ~ 10 Å. In $LH2_O$ the spacing is larger, and the coupling is weak. Due to the intervening protein matrix, the electronic coupling between adjacent rings is also weak. Although strong coupling is present, Förster theory can be used to understand many of the dynamics present in these systems. In this sense, homo-FRET is the mechanism of intra-ring transfer, and transfer between identical components of the LH2 rings, whereas hetero-FRET governs all other inter-ring transfers.

Even with the weak coupling, transfer between rings is much faster than the lifetime of the excitation, and transfer within each ring is faster still, allowing >95 % of excitations (absorbed photons) to end up at the reaction center.[161] The slowest transfer rate is between LH1 and RC, due to the comparably long distance between them. It is believed that the RC is shielded from the rest of the system in this way to avoid unwanted side reactions, which can completely quench the flow of energy transfer. The slight differences in environment between the various rings confers an energy gradient to the system where the energy of light absorbed follows the order $LH2_O$ (800 nm) > $LH2_I$ (850 nm)> LH1 (875 nm nm)> RC (960 nm). This is an important factor which helps to rapidly funnel the excitation energy to the RC, no matter where in the system excitation occurs. Recall that homo-FRET is a random walk process (2.4.3). The energy gradient thereby serves to direct the flow of excitation energy by incorporating a few unidirectional transfer steps.

Although this discussion has focused on purple bacteria light harvesting some general considerations from other systems are in order. Both green plants and cyanobacteria have evolved from species similar to the purple bacteria.[162, 163] This evolution has resulted in even tighter packing of the dyes.[164, 165] In these systems the transition dipole directions of the chlorophylls do not seem to play an important role.[166, 167] The conclusion is that if the dyes have sufficient dipole strengths and are placed sufficiently close together, the electronic coupling is so strong that alignment of the dipoles does not seem to be necessary for efficient transfer to the RC.

It seems that the most important features of natural light harvesting to emulate in synthetic systems are the photophysical properties of the dyes involved, and their relative distances. Having a scaffold able to position numerous dyes seems to be an important first step for artificial antenna systems. By employing the architecture presented above, the purple bacteria RC has an effective absorption coefficient between 4.5×10^6 $M^{-1}cm^{-1}$ and 45×10^6 $M^{-1}cm^{-1}$ depending on light conditions during growth, representing an increase in excitation energy of 30-300 times delivered to the RC due to the antennas.

4.2   ARTIFICIAL SYSTEMS

The ability to control the flow of energy in nano systems is an intriguing possibility, and one that has inspired a great deal of effort into creating artificial light harvesting systems. A plethora of approaches have been attempted, and inorganic systems are employed in photovoltaic cells today. Here focus will instead be placed on the attempts to use organic systems for light harvesting. Deeply entwined with this pursuit lies the field of organic based nano-photonics. These systems in turn aim to shuttle excitation energy over large distances, often using homo-FRET and energy gradients similar to natural light harvesting systems. These pursuits will lead to DNA based light harvesting and photonic structures, which will be given the most attention.

4.2.1   ORGANIC SYSTEMS

The first artificial organic systems relied on traditional organic synthesis to produce a single complex molecule consisting of light harvesting and reaction center units, coupled together via covalent bonds.[168-173] These systems generally require organic solvents, but their main drawback is the incredible amount of time each synthesis takes. For every new system, a new synthetic route is necessary. Furthermore, covalent coupling of ever larger systems becomes extremely challenging, and the largest complexes made could only incorporate 4 light harvesting chromophores. The field of nano-photonics has employed similar structures to create molecular wires able to shuttle excitation energy over relatively large distances with high efficiency.[174, 175] However, the same drawbacks are present in these systems as for the artificial photosynthetic systems described above. Instead focus has shifted towards dendrimers and self-assembled systems as alternatives. Dendrimers allow for the inclusion of a larger number of light harvesting chromophores, and have resulted in very efficient systems.[176-179] However, synthesis is still difficult, and the placement of the final acceptor at the core of a 3D shell is not advantageous for harnessing the transferred energy. Self-assembled organic systems show promise in that modularity is possible.[180-182] However, design of components to specifically self-assemble into pre-arranged patterns is extremely challenging. Some interesting work using virus-templated fluorophores seems promising in this regard.[183, 184]

4.2.2   DNA BASED SYSTEMS

There are many advantages to using DNA-based systems for artificial light harvesting.[185] DNA nanotechnology allows for the construction of modular components which can self-assemble through sticky-end cohesion, and DNA structures are generally water soluble. DNA can be modified at specific bases with organic dyes, either externally or as a modified base, and a wide range of dyes are commercially available for external modification.[186] In this way, design and synthesis of novel DNA light harvesting constructs can take as little as a few days.

There are two main aspects of natural light harvesting that have been transferred to DNA based systems. The first is the use of an energy cascade to directionally transfer excitation energy between different dyes via the hetero-FRET mechanism. This avenue

has mainly been pursued in the area of nano-photonics. DNA based energy cascades have been designed with various dyes along a linear scaffold reaching up to 4 directed transfer steps.[187-192] An example of this is shown in Figure 20 where the DNA is attached to a fluorescent quantum dot. The quantum dot has a very large absorption coefficient and is the initially excited dye in the system. The cascade consists of 4 covalently attached dyes on the DNA, with decreasing energy between ground and excited states the further from the quantum dot they are placed. In this way energy jumps from the quantum dot via the covalently attached dyes and ends at the terminal acceptor dye. Another example employed DNA origami to position covalently attached dyes on a 2D scaffold.[193] In this way an energy cascade was created where the direction of energy transfer could be controlled through the binding of a mediator dye. In our group a covalently attached dye was attached to DNA and transferred its excitation energy to a porphyrin acceptor. In the excited state the porphyrin could oxidize a quinone.
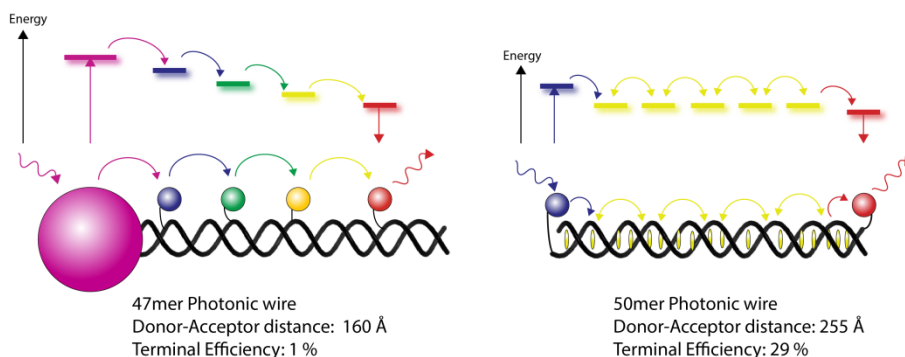

47mer Photonic wire
Donor-Acceptor distance: 160 Å
Terminal Efficiency: 1 %

50mer Photonic wire
Donor-Acceptor distance: 255 Å
Terminal Efficiency: 29 %

Figure 20. Comparison between a photonic wire employing only a series of hetero-FRET transfers to transfer excitation energy (left)[187] with a photonic wire employing both an energy cascade and mediating homo-FRET transfer reactions (right).[27] Although the systems use different configurations and dyes, it is clear that the terminal transfer efficiency is greatly enhanced through the series of homo-FRET transfers.

The second aspect of natural light harvesting that has been transferred to DNA based systems is the use of several identical dyes to transfer excitation energy over large distances via the homo-FRET mechanism. For effective homo-FRET, the dyes must be in close proximity. In our group a photonic wire and branched structure with selectable output were created using both an energy cascade and DNA intercalating dyes to take advantage of homo-FRET transfer steps.[27, 194] The wire is shown in Figure 20 as a comparison to the system employing purely an energy cascade. Although comparison between such differently constructed systems is difficult, it is clear that homo-FRET transfer steps greatly increase the terminal transfer efficiency. Intercalating dyes were also used by Armitage and co-workers as initial light harvesters able to transfer energy to specific covalently attached acceptors.[195, 196] This principle is very similar to natural light harvesting, and resembles the systems we use in paper 3 and 4. The first example of 3D DNA as a scaffold for light harvesting and energy transfer was a 7 helix bundle with 6 initial light harvesters, 6 intermediate dyes and a single acceptor (shown in Figure 21).[197] In this way energy could in principle be

transferred via both homo-FRET and hetero-FRET mechanisms, although energy transfer in this system proved to be ineffective, likely due to large distances between the dyes, and poor spectral overlap.
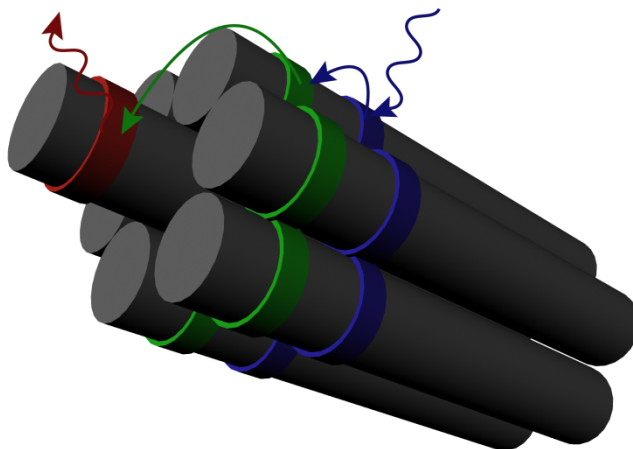

Figure 21. Cartoon of a DNA light harvesting and energy cascade structure based on a 7 helix bundle DNA scaffold.[197] Light is initially absorbed by the covalently attached dyes with highest absorption energy (blue) and is subsequently transferred to dyes with lower energy excited states (green) through hetero-FRET. A second hetero-FRET transfer occurs from the green to the red dyes.

5   ORIGINAL WORK

5.1   REVERSIBLE ASSEMBLY OF DNA CONSTRUCTS AT THE LIPID-AQUEOUS INTERFACE (PAPERS 1 AND 2)

The goal of this work was to investigate the self-assembly properties of DNA when anchored to phospholipid bilayers. The work is in many ways a natural extension from work in our group concerning the attachment of DNA to liposomes and investigations into dynamic DNA behavior at this interface, as presented in section 3.3.1. The work presented below was performed both in solution where lipids had been extruded to form unilamellar liposomes of 100 nm diameter, and on supported lipid bilayer surfaces. Two DNA structures were investigated, and are shown in Figure 22. The first is a simple 39mer duplex where one strand has been covalently modified with a zinc-porphyrin anchor. This structure was studied on supported bilayers using the QCM-D technique. The second structure is built from nine single strands, and forms a pseudo-hexagon. It consists of a central hexagon with 10 base-pairs per side (this motif is shown in Figure 12, section 3.1.2), and 3 protruding arms. Anchoring is provided by covalent porphyrin modification of one of the two strands in the arm duplex, and the anchoring strand is identical for both the pseudo-hexagon and the linear construct. In this way, 1-3 arms can be modified providing structures with anywhere between 1 and 3 anchors. The pseudo-hexagon structure was studied both in solution attached to liposomes and on supported bilayers.
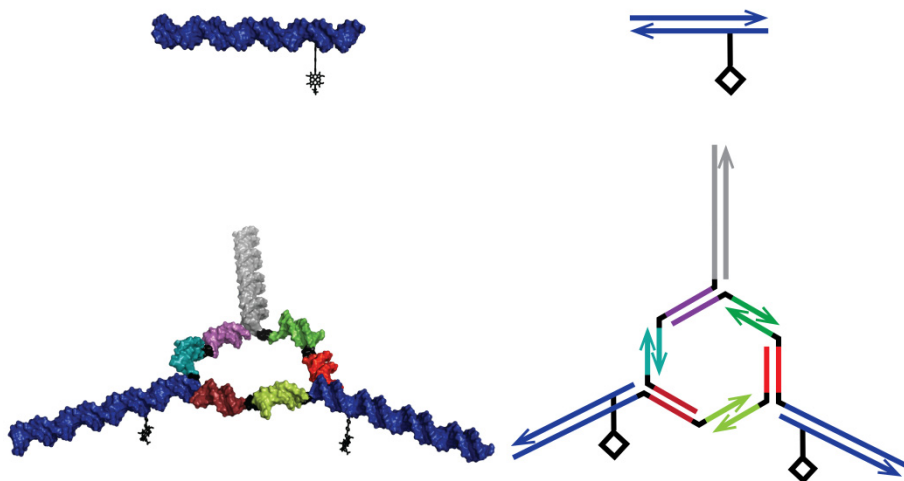
Figure 22. Top panel shows the 39mer duplex structure with one porphyrin anchor. The bottom panel shows one the three possible pseudo-hexagon structures. This structure has two porphyrins and is therefore named Hex2P. The structure is color coded so that complementary sequences have the same color. Arms containing porphyrins have different sequence than arms without porphyrin allowing for the specific placement of porphyrin modifications. The central hexagon has the same sequence for all constructs.

5.1.1   LINEAR CONSTRUCT (PAPER 1)

The main QCM-D experiments conducted for the 39mer duplex structure are shown schematically in Figure 23, and include binding to the bilayer, hybridization of a complementary strand to a surface anchored strand, and melting of the duplex while one strand is attached to the bilayer. Two linker lengths between the DNA and porphyrin were compared, containing either two (**bi-pe**) or three (**tri-pe**) phenylethynylene units. At room temperature the anchoring strand in single stranded form proved to bind very slowly to supported lipid bilayers, making it impossible to study hybridization at the surface. This was attributed to hydrophobic intramolecular interactions between the porphyrin and exposed DNA bases. The most important measurements were therefore conducted at 60 °C, where the higher temperature greatly increased the binding rate. Binding of ss **tri-pe** was still slow at this elevated temperature, so ss **bi-pe** was primarily studied. It should be noted that binding of both double strands, ds **bi-pe** and ds **tri-pe,** was efficient even at room temperature.
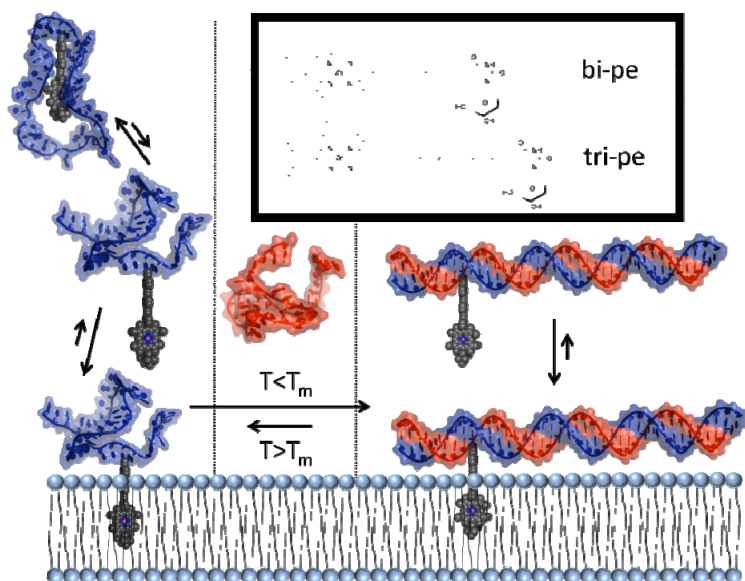

Figure 23. Schematic representation of the main experiments and results from studying the 39mer linear construct. The left panel shows that ss **bi-pe/tri-pe** bind strongly to the bilayer, although an increase in temperature is needed to overcome a kinetic barrier. The second panel shows hybridization of the anchored single strand with its complementary sequence (ss **comp**). The second panel also shows that hybridization is a reversible process, and that the duplex can be melted while the anchoring strand remains attached to the surface. The right panel shows strong binding of ds **bi-pe/tri-pe** to the bilayer.

Figure 24A and B compare QCM-D measurements of real-time binding of single (ss) and double stranded (ds) **bi-pe** to supported lipid bilayers at 60 °C. The 13th overtone is plotted, as this was least susceptible to air bubbles which had formed at this elevated temperature. In Figure 24A the frequency change (Δf) is plotted versus time, as a solution of either ss or ds **bi-pe** is made to flow over the bilayer, and Figure 24B shows

the concomitant dissipation change (ΔD). The decrease in frequency indicates an increase in surface mass (through the Sauerbrey equation, section 2.6) revealing that binding to the bilayer occurs for both structures. Furthermore, the frequency changes indicate that more single strands bind to the bilayer compared to double strands, at saturation. This behavior is expected based on the stiffness of the two adsorbing molecules. The single strand has a short persistence length allowing denser packing in the bilayer, whereas the duplex is relatively stiff and occupies a larger projected surface area.
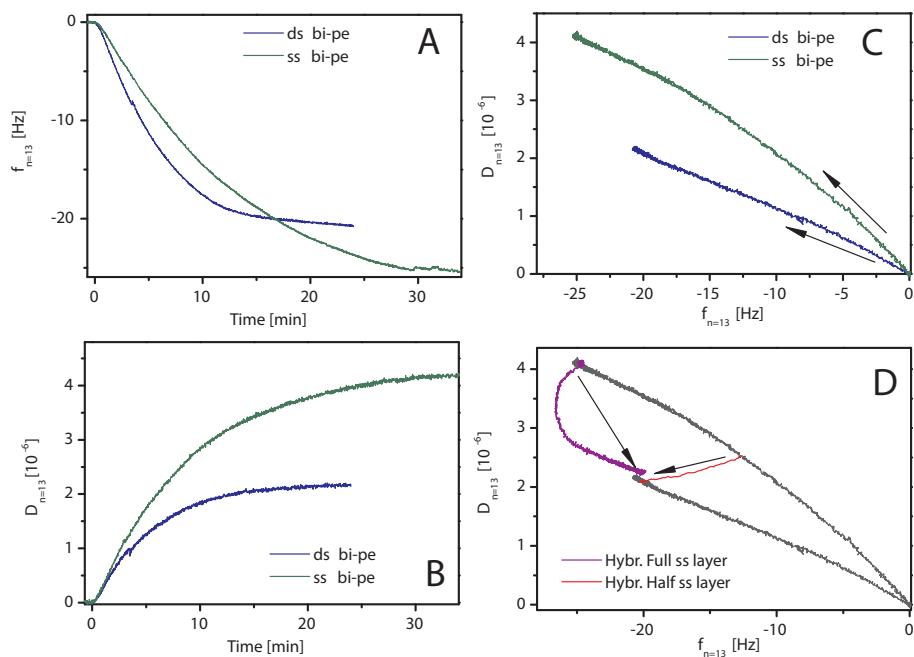

Figure 24. (A) Frequency changes obtained upon binding of ss and ds **bi-pe** to supported lipid bilayer at 60 °C. (B) Concomitant dissipation changes measured simultaneously with (A). (C) The dissipation data in (B) plotted versus the frequency data in (A), revealing fingerprints of the binding. (D) Hybridization of bound ss **bi-pe** with its complementary strand ss**comp** at half (red line) and full (purple line) surface coverage.

The viscoelastic properties of the adsorbed DNA films are related to the ratio between the changes in dissipation and frequency ($-\Delta D/\Delta f$, see section 2.6). From Figure 24A and B it is difficult to determine by eye whether ss **bi-pe** and ds **bi-pe** vary in this regard. Instead, a plot of the dissipation change versus frequency change (termed ΔD-Δf) reveals viscoelastic variations in the two films, as shown in Figure 24C, where the data from Figure 24A and B are replotted. The arrows indicate the progression in time. Such a plot can serve as a fingerprint of the binding as a function of increasing adsorbed mass if there is a difference in viscoelastic properties between the surface films formed (see section 2.6). Clear differences are observed between the ss **bi-pe** and ds **bi-pe** ΔD-Δf plots, indicating that the double strand forms a more rigid layer with lower ΔD values as Δf increases. This is expected based on the much longer persistence

length of duplex DNA compared to single stranded DNA (section 3.1.1). The obtained fingerprints can subsequently be used to study processes which transfer the system from single to double stranded form or vice versa (hybridization and denaturation). One can thereby see if the system is completely double stranded, completely single stranded, or in an intermediate state by comparing with the fingerprints in Figure 24C.

The effect of hybridization on the structural properties of the ss DNA film was studied at two different single strand surface densities by flowing a solution of the complementary strand, ss **comp**, over the surface, as shown in Figure 24D, where the two fingerprints from Figure 24C have been colored gray to aid in determining if hybridization is complete. At half coverage of ss **bi-pe** hybridization is observed as a decrease in frequency and dissipation (red curve), where the arrow indicates the direction the curves progress as a function of time. Although not shown in this plot, the process is rapid, taking only ~100 s before both the frequency and dissipation have ceased to change. Based on the fingerprints in Figure 24C it is clear that a complete layer of double stranded constructs is formed with ~100 % efficiency, since the values of ΔD and Δf correspond to a double stranded layer. The complementary strand must therefore be able to wrap around the site of the porphyrin modification to form the duplex. At full coverage of ss **bi-pe** the behavior is more complicated to interpret. One important observation is that there is an initial increase in adsorbed mass, followed by a decrease to a value very similar to that for hybridization at half coverage. During this process the dissipation steadily decreases, also to a value similar to that obtained for hybridization at half coverage of ss **bi-pe**, indicating that the layer formed has exactly the same fingerprint as a full layer of ds **bi-pe**. For this to happen, roughly half of the bound molecules must have desorbed from the surface, which is corroborated by the observed overall decrease in mass upon hybridization. Upon hybridization at full coverage of ss **bi-pe**, bound molecules are forced into solution by the hybridization process at the surface, in order to make room for the duplexes. It seems that there are two likely scenarios which could explain the ΔD-Δf plot. The initial increase in mass could indicate that the complementary strands initially bind rapidly to the surface-anchored strands, but only with a few base-pairs followed by zipping of the helix to form the complete duplex. It would then be this zipping which forced some molecules to desorb. Alternatively, there is room on the surface for some single strands to fully hybridize yielding an initial increase in mass. As more strands hybridize the surface eventually becomes saturated, and further hybridization results in desorption of some strands.

Both the rapid hybridization at half coverage and the expulsion of surface bound molecules upon hybridization at full coverage are a consequence of the unique properties of the lipid bilayer and the porphyrin anchor. It seems that the soft nature of the bilayer allows for rapid hybridization, even at the site of the porphyrin modification. Furthermore, the coupling between the porphyrin and the lipid bilayer is strong enough to allow binding without significant dissociation, but dynamic enough to allow adaptation of the binding density upon hybridization at high coverages.

Denaturation, the reverse process of hybridization, is energetically unfavorable due to the low free energy of the duplex compared to two single strands. To denature the duplex either energy is required, in the form of elevated temperatures, or other

conditions which decrease the stability of the duplex. Unfortunately, large changes in temperature greatly affect the frequency and dissipation, resulting in signal drifts and the fingerprints become impossible to follow. Instead, denaturation was monitored indirectly as re-hybridization of the duplex after denaturation at 80 °C, removal of unanchored single strands and cooling to room temperature. The binding of ds **tri-pe** to a bilayer and rehybridization following the above procedure is shown in Figure 25 through changes in frequency. The data is similar to hybridization at half coverage of single strand at 60 °C as expected, with both a similar frequency and dissipation shift (not shown). Heating and cooling are not shown in the figure, and the frequency response after the heating/cooling procedure has been adjusted to compensate for drifts in frequency during the procedure.
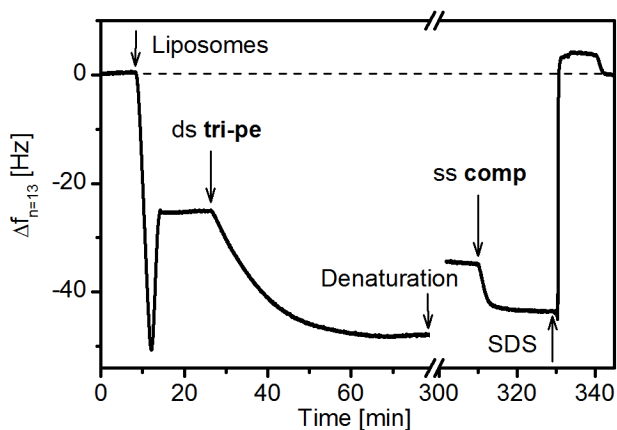

Figure 25. Frequency changes obtained upon rehybridization of surface anchored ss **tri-pe** with its complementary sequence ss **comp**. The figure shows the initial addition of liposomes and formation of the supported bilayer. This is followed by addition of ds **tri-pe** until saturation. The system is subsequently heated to 80 °C and unanchored strands are removed. This is followed by cooling to room temperature. Heating and cooling are not shown, but occur during the break in the Time axis. Finally ss **comp** is added resulting in hybridization and a decrease in frequency. The dotted line corresponds to the initial and final state of the system which is a SiO_2 surface in buffer. The frequency change after the whole procedure and following washing with SDS is shifted to match with that of the initial system.

To avoid the large frequency and dissipation changes associated with changes in temperature, denaturation of the anchored duplex was attempted by exchanging the bulk solution to purified water. This process should destabilize the helix and perhaps denature the duplex. However, this was not observed and instead duplexes were ejected into solution in a manner similar to hybridization at full coverage of ss **bi-pe**. This was attributed to increased repulsion between neighboring duplexes as the positively charged counter ions were removed by the purified water. Interestingly, not all duplexes desorbed from the bilayer; even after several tens of minutes of rinsing with purified water around 15% remained bound.

5.1.2   HEXAGONAL CONSTRUCT (PAPER 2)

Although hybridization and denaturation of anchored duplex DNA are good starting points to demonstrate the applicability of lipid bilayers as substrates for DNA nanoconstructs, we wished to study larger constructs and how they can be aligned to the membrane surface. Such alignment is important for communication with the surface through, for example, electron transfer reactions, and for the formation of larger structures by connecting lipid bound DNA modules. The studied structures are shown in Figure 26 and are based on the hexagon motif presented in Figure 12, section 3.1.2 where three of the strands have been extended by 39 bases. The sequences of these overhangs are identical, and designed to hybridize with the anchoring strand presented above (ss **tri-pe**). This allows the same anchoring strand to bind to the three protruding arms. Alternatively, the sequence protruding from the hexagon could be modified to instead bind a complementary strand lacking the porphyrin anchor. In this way the placement of porphyrin anchors could be controlled, with a total number of anchoring porphyrins of 1 (Hex1P), 2 (Hex2P), or 3 (Hex3P). The pseudo-hexagon shown in Figure 26 is color coded to reflect this, where the arms containing porphyrins are blue, whereas the arms without porphyrin are colored gray.
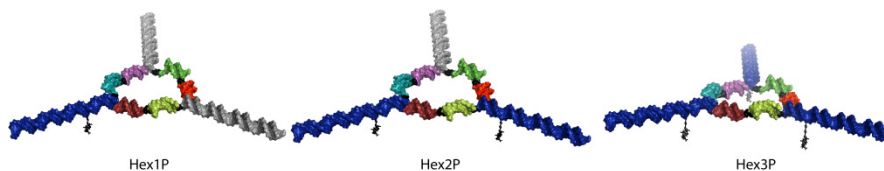

Figure 26. Pseudo-hexagonal structures with porphyrin anchors placed on the protruding arms. The number of arms modified with porphyrins could be varied between 1 (Hex1P), 2 (Hex2P), or 3 (Hex3P).

5.1.2.1   ANCHORED TO LIPOSOMES

The role of the number of porphyrins per construct on the binding density in the bilayer was investigated by titrating small amounts of each construct to a solution of liposomes. Changes in the fluorescence spectrum of the porphyrin were used to follow the fraction of membrane-bound porphyrin, and thereby obtain a binding curve. The binding curve was analyzed by fitting to equation 47,

$$[HexP]_{bound} = \frac{\frac{1}{K}+[HexP]_{tot}+[L_0]\cdot n}{2} - \sqrt[2]{\frac{\frac{1}{K}+[HexP]_{tot}+[L_0]\cdot n}{4} - [L_0]\cdot n \cdot [HexP]_{tot}} \quad (47)$$

where $[HexP]_{bound}$ is the concentration of bound construct, $[L_0]$ is the lipid concentration in solution, $[HexP]_{tot}$ is the total concentration of construct, K is the equilibrium constant, and n is the number of binding sites per lipid. The value of n was used to calculate the area occupied by the construct in units of Å², as shown in Figure 27a and b.
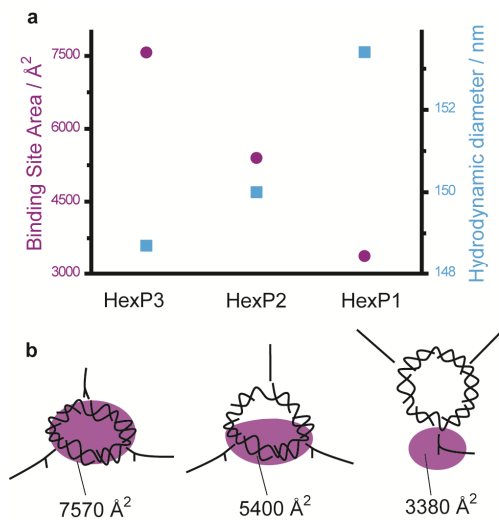
Figure 27. (a) Hydrodynamic diameter of DNA-liposome constructs and fitted binding area from spectrofluorometric titrations as a function of the number of porphyrin anchors per DNA construct. (b) Schematic drawing of the anchored DNA constructs where the fitted binding site area is displayed in purple.

The measurements revealed that the binding area increased with the number of anchors, meaning that fewer constructs could be anchored to the surface for Hex3P compared to Hex1P. This is likely an effect of the alignment of the structures to the surface. It is important for this discussion to remember that each side of the hexagon is connected by two thymines (TT) which are not base-paired. Also the three arms are coupled to the central hexagon in this way (see Figure 22 where black color indicates TT). For Hex1P the structure is very flexible since it is coupled to the surface with only a single anchor point, and can therefore protrude away from the surface, displaying a smaller projected surface area. The surface area of Hex3P obtained from the fitting procedure is much larger, due to anchoring of each arm to the bilayer surface. A similar fitted area was obtained for Hex3P as the area of the central hexagon, indicating that this structure is indeed aligned with the membrane surface.

To further investigate the role of the number of anchors on the alignment of the constructs to liposomes, hydrodynamic size measurements of the liposome-DNA diameter were performed using dynamic light scattering (DLS) at saturating amounts of each of the DNA constructs. There are two factors which are expected to influence the diameter of the liposomes upon binding of the DNA-porphyrin structures. The first is the effect of the anchor itself. Incorporation of the porphyrin into the liposomes adds a large amount of mass, and the liposomes are expected to swell. Since Hex3P contains three anchors, one would expect this effect to be largest for this construct. The second effect is from the DNA itself. Hex1P is expected to protrude away from the surface and therefore increase the hydrodynamic radius significantly compared to the membrane aligned Hex3P. Figure 27 shows that the hydrodynamic diameter follows the order Hex1P>Hex2P>Hex3P and corroborates the findings from the

spectrofluorometric titration wherein Hex1P was seen to occupy a smaller surface area by protruding away from the liposome surface.
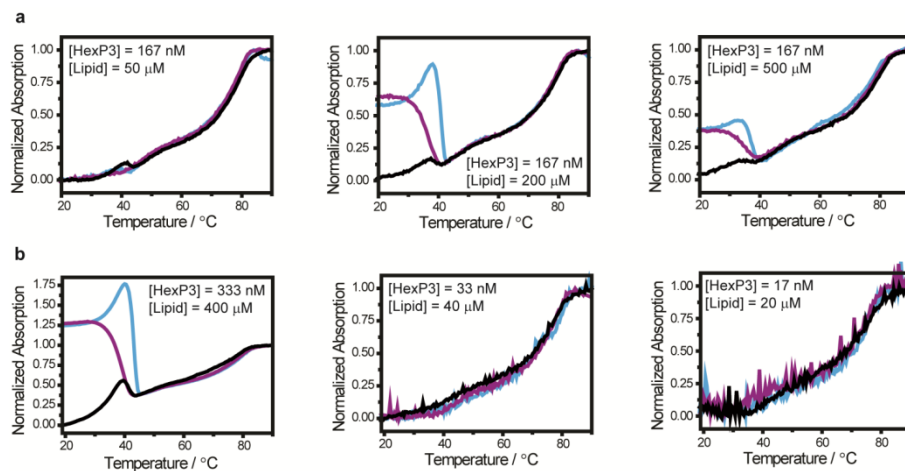

Figure 28. UV absorption melting curves of prehybridized Hex3P anchored to liposomes via 3 porphyrin anchors. Black curves represent the initial heating phase, purple curves are cooling, and light blue curves are a second heating cycle. Panel a shows melting curves upon variation of the lipid concentration at a constant concentration of Hex3P. At high ratios of Hex3P:Lipid, the DNA melts reversibly, in a similar manner to bulk solution. As the ratio decreases, reannealing forms aggregates of liposomes connected by the DNA, as seen through the higher absorption values. Panel b shows that this aggregation behavior is not only dependent on the Hex3P:Lipid ratio, but also on the total concentration of the two components in the solution. At low concentration aggregation is not observed.

Reversible formation of the DNA nanostructures when attached to lipid bilayers is paramount for self-healing applications. Completely reversible structure formation of prehybridized Hex1P and Hex2P anchored to liposomes was observed through UV DNA melting curves, which were identical to melting curves obtained without liposomes. For Hex3P the ratio between porphyrin-DNA and liposomes in solution and the total concentration of both liposomes and porphyrin-DNA play an important role for the reversible formation of the structures. UV melting curves of prehybridized Hex3P attached to liposomes are shown in Figure 28. The black curves are the initial heating and show two transitions corresponding to melting of the central hexagon (~40 °C) and melting of the arms (~80 °C). It is important to note that the anchoring strands remain bound to the liposome even at the elevated temperature, exactly as observed for the linear structure described above. Panel (a) shows the effect of increasing the concentration of lipids while keeping the concentration of Hex3P constant. There are two factors which are influenced by the increase in lipid concentration. The first is that the density of Hex3P attached to each liposome decreases. The second is that the concentration of liposomes in solution increases. At low lipid concentrations, reversible structure formation is observed. At higher lipid concentrations, melting results in large distances between anchors on the liposome surface. In this case cooling after denaturation can result in rehybridization between anchors attached to separate liposomes, which in turn induces liposome aggregation.

The liposome aggregates scatter UV-light efficiently and this is observed as large increases in OD (optical density) upon cooling (purple curves) to a temperature near the melting point of the hexagon part of the structure. The increase in liposome concentration is also expected to play a role in this effect, since the mean distance between liposomes decreases at high lipid concentrations, increasing the likelihood of hybridization between liposomes. It should be noted that the aggregates are easily dissolved by increasing the temperature again (light blue curves). To determine the influence of liposome concentration specifically, panel (b) shows a dilution series where the density of Hex3P per liposome is held constant, but the overall concentration of the sample is reduced. At high concentrations, liposome aggregation is observed, yet dilution results in larger distances between liposomes and aggregation does not occur.

5.1.2.2 ANCHORED TO SUPPORTED BILAYERS

5.1.2.2.1 MOBILITY IN BILAYER

To demonstrate that the lipid bilayer acts as a mobile surface able to transport anchored DNA constructs, the diffusion of ds **tri-pe**, Hex1P, Hex2P and Hex3P anchored to supported lipid bilayers was investigated using fluorescence recovery after photobleaching (FRAP) and the results are shown in Figure 29. Analysis of the FRAP data revealed that all structures diffused on the bilayer surface. As expected, the diffusion rate depended both on the mass of the anchored DNA, and on the number of anchors per construct. The fastest diffusion was observed for ds **tri-pe** with a diffusion coefficient similar to fluorescently labeled lipids.[30] Hex1P contains the exact same anchoring strand as ds **tri-pe** and differs only in the mass of the anchored DNA, and the diffusion coefficient for this construct is lower due to the higher load. The number of anchors is also important, with the diffusion coefficients of the pseudo-hexagonal structures following the order Hex1P>Hex2P>Hex3P.
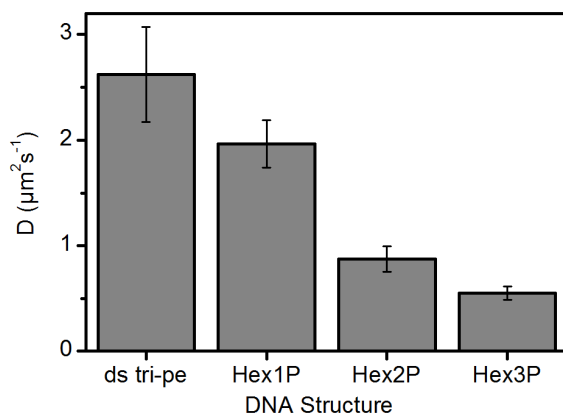

Figure 29. Diffusion coefficients of the porphyrin-DNA constructs anchored to lipid bilayers as obtained through FRAP measurements.

Although reversible formation of the constructs Hex1P, Hex2P and Hex3P on liposomal surfaces was observed based on UV melting curves, we wished to study if the same behavior could be observed on supported lipid bilayers. Furthermore, anchoring to the supported bilayer enables the exchange of bulk solution. In this way denatured strands can be removed from the system, and new strands added, greatly increasing the versatility of the system. This allows for not only the reversible formation of a single construct, but also the ability to change this construct into a new one, while using the same anchoring strand (*vide infra*, Figure 33).

QCM-D measurements were performed to study the binding of Hex1P, Hex2P, and Hex3P to supported lipid bilayers. We wished to study reversible structure formation based on the frequency and dissipation responses as was done for hybridization of anchored ss **bi-pe** in section 5.1.1 To follow reversible formation using this method clear differences between the ΔD-Δf curves are necessary. Such differences are expected based on the liposome solution data for two reasons. The first is that the total mass (frequency change) observed by QCM-D upon saturation binding should have the order Hex1P>Hex2P>Hex3P due to the decrease in surface densities along this sequence. More importantly, Hex1P is expected to be a less stiff structure and therefore have a higher dissipation per frequency, due to internal motion at the TT hinges which dissipates energy. Hex3P is anchored in three places and aligned to the surface, meaning that the degrees of freedom and possibility of intramolecular energy dissipation are heavily reduced, and Hex3P is expected to show the lowest ΔD values as Δf decreases (surface mass increases).

Figure 30A shows the ΔD-Δf plots for binding of the three constructs to supported lipid bilayers. The three structure types are clearly distinguishable from each other at binding densities corresponding to a frequency shift of at least -10 Hz. The trend is as expected with Hex1P forming the softest film, followed by Hex2P, and Hex3P showing the stiffest film. The curve for the 39mer ss **tri-pe** hybridized to its 63mer complementary strand (ds **arm**) which has sequences which form two sides of the hexagon (see Figure 22) is shown for comparison, and displays an even stiffer film.

Again we wished to demonstrate reversible assembly of the structures at the interface between the bilayer and buffered solution. Furthermore, the attachment to supported bilayers allowed us to determine if this was possible without annealing the structures, by removing unanchored strands after denaturation and subsequently performing the reassembly at room temperature. Two methods of denaturation were attempted, and both resulted in selective disassembly of the hexagon, leaving the arms, consisting of 39mer anchoring strands hybridized to their 63mer complementary strands, on the surface (these constructs are termed ds **arm**). The first denaturation method was to increase the temperature to a value between the melting of the hexagon and the arms (45 °C was chosen). The second was to exchange the bulk fluid pH from 8 to 10.3, resulting in weakened hydrogen bond interactions between the DNA base-pairs.
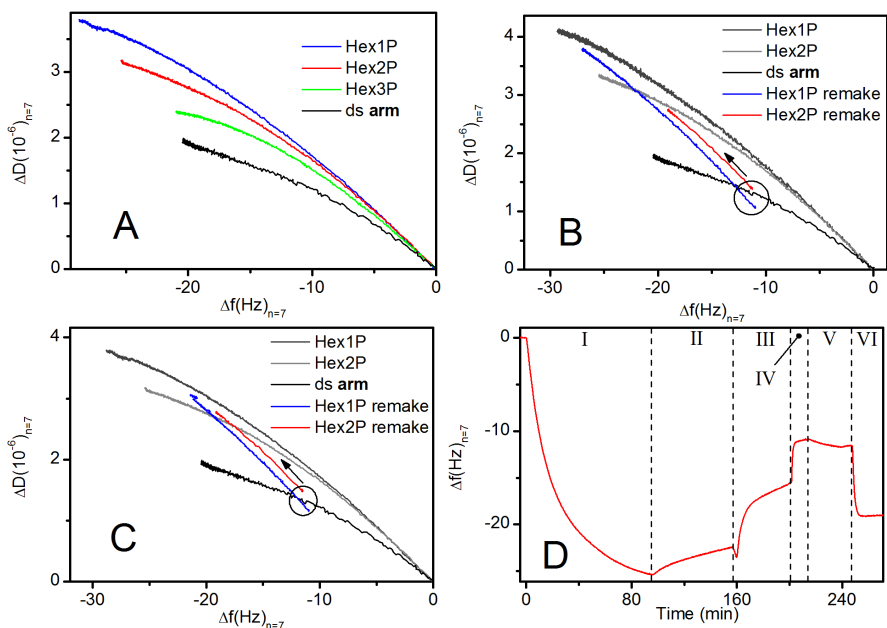
Figure 30. Binding of pseudo-hexagonal structures to supported lipid bilayers and reversible formation of bound structures at the lipid/aqueous interface. (A) ΔD-Δf plots of Hex1P, Hex2P and Hex3P upon binding to supported lipid bilayers. Binding of ds **arm** is shown for comparison. (B) Re-formation of pseudo-hexagonal structures (Hex1P and Hex2P) after denaturation of the central hexagon by heating to 45 °C. The gray curves show the initial binding of the structures, and the circle indicates the values of ΔD and Δf after heating, removal of dissociated strands, and subsequent cooling. From this point the missing strands are added to reform the initial structure, as indicated by the arrow. (C) As (B), but denaturation of the central hexagon was accomplished by flowing a solution with pH = 10.3 (compared to the buffer pH = 8) over the surface. (D) The frequency response of Hex2P in (C) plotted versus time showing (I) binding to the bilayer, (II) washing with buffer, (III) exchange to pH = 10.3 solution, (IV) exchange to buffer, (V) addition of connecting strand and (VI) addition of prehybridized missing strands (see Figure 31).

The ΔD-Δf responses upon reversible formation of the central hexagon at the bilayer-aqueous interface after heating to 45 °C is shown in Figure 30B and after exchanging the bulk to high pH solution is shown in Figure 30C. The responses look very similar in the two cases. The figures show the initial binding of Hex1P and Hex2P in gray and ds **arm** is shown in black for comparison. The denaturation process and removal of unanchored strands is not shown due to the large shifts in frequency and dissipation this entails. Addition of the missing strands is shown in blue for Hex1P and in red for Hex2P, and the arrows indicate the progression of the signal in time. After the denaturation procedure and return to normal buffer at room temperature, only ds **arm** is left on the surface (marked with a circle). For a perfect system where there is no drift in the QCM-D signal upon exchange of the bulk solution, and where a perfect layer of ds **arm** is formed, the blue and red curves should intersect the curve for ds **arm**. Although this is not the case, the ΔD-Δf values are very similar to that of ds **arm** for both constructs. The red and blue curves progress to ΔD-Δf values similar to the initial

constructs Hex1P and Hex2P indicating that reversible formation is indeed occurring. For Hex3P (not shown) this was not the case. The structure could be disassembled, but reassembly showed ΔD-Δ*f* values differing from the initial binding curve.

To help understand the reversible assembly process in detail, the frequency shifts for the complete process for Hex2P; (I) initial binding, (II) buffer rinse, (III) pH denaturation, (IV) return to normal pH, and (V-VI) subsequent reassembly, are shown in Figure 30D. A schematic diagram of the same process is shown in Figure 31. The initial binding results in an increase in surface mass (decrease in frequency). Rinsing then removes some constructs from the layer and the frequency increases slightly. The change to high pH solution initially results in a small decrease in frequency followed by a relatively large frequency increase. The small decrease is due to the bulk liquid change, but is not easily observed due to the almost immediate onset of dissociation of denatured strands from the surface, which decreases the sensed mass (increased Δ*f*). After stabilization, the bulk fluid is returned to normal buffer resulting in a further increase in Δ*f*. Finally the reassembly is performed in a two-step procedure. This was done to increase the probability of hybridization resulting in ring-closed structures as opposed to large chains of ds **arm** hybridized to each other. The surface contains two types of ds **arm** diffusing freely. The first step hybridizes these pair-wise using a short strand from the hexagon which contains two stretches and a TT bridge; each stretch able to attach to one type of ds **arm** (see Figure 31). The last step is the addition of the prehybridized remaining strands, which ring-closes the structure.
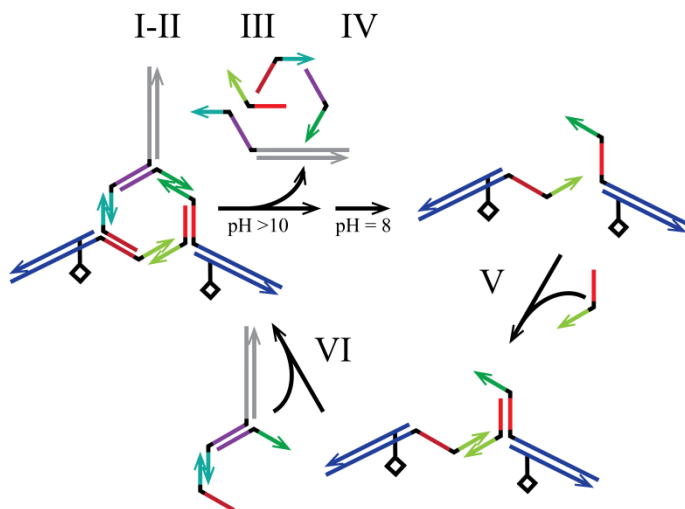
Figure 31. The process of reversible structure formation of Hex2P attached to the lipid bilayer via two porphyrin anchors, at room temperature. The six steps (I-VI) correspond to the steps shown in Figure 30D.

The intermediate state (between IV and V) with only ds **arm** on the surface allows a more versatile route to structure formation than previously shown, through the use of strand displacement. Each ds **arm** consists of the 39mer ss **tri-pe** hybridized to a 63mer complementary sequence, yielding a 24mer overhang. This overhang can act as a toehold for strand displacement where a third strand (ss **fc**) is added which is fully

complementary to the 63mer strand attached to ss **tri-pe**. The duplex formed between the two 63mer strands is thermodynamically more stable than the duplex ds **arm**. When ss **fc** is added to a bilayer containing ds **arm** hybridization of the 24mer toehold region is expected, followed by strand displacement due to the lower free energy of the 63mer duplex. The resulting frequency changes due to this process are shown in Figure 32A where (I) ds **arm** is added to the bilayer, followed by (II) buffer rinse, (III) addition of ss **fc**, and (IV) addition of the 63mer sequence which was previously removed. The frequency increases upon addition of ss **fc** (decrease in mass) as expected, and the process is fully reversible since hybridization with the 63mer sequence results in a layer with similar mass as the initial ds **arm** construct.

So how does strand displacement yield a versatile route to structure formation? The key is the layer of ss **tri-pe**, the anchoring strand in single stranded form, which is formed in step III. Such a layer could not be created by simply flowing the strand over an empty bilayer, due to intramolecular hydrophobic interactions (see section 5.1.1). From a layer filled with ss **tri-pe** any of the structures discussed up to this point can be created by simply adding the prehybridized missing strands. In fact, any DNA structure with a complementary sequence to ss **tri-pe** could be anchored in this way. We demonstrate this in Figure 32B which shows the frequency changes upon adding the prehybridized missing strands needed to form Hex1P, Hex2P, and Hex3P to a layer of ss **tri-pe** formed using the strand displacement method. A difference in bound mass is expected depending on the number of anchoring strands each construct binds. For example, Hex1P binds a single anchor strand and the frequency shift is expected to be three times larger than for Hex3P, which binds three anchor strands per construct. The ratio between the obtained frequency shifts exactly matches the expected trend.
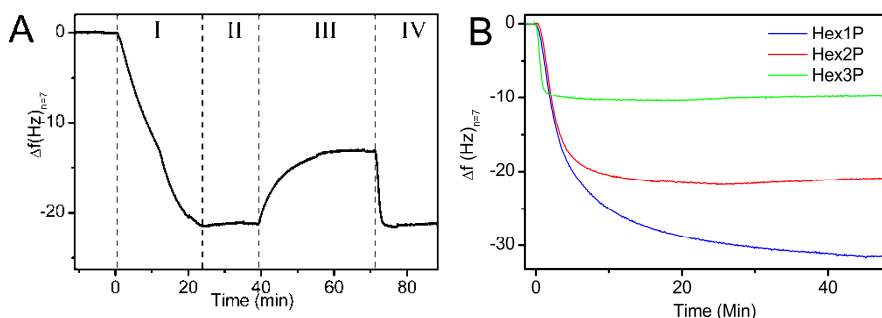
Figure 32. (A) Strand displacement reaction followed by rehybridization. (I) The structure ds **arm** is bound a lipid bilayer, followed by (II) buffer rinse, (III) strand displacement using ss **fc**, and (IV) rehybridization using the strand which was displaced. (B) Formation of the three structures Hex1P, Hex2P and Hex3P following a strand displacement reaction.

In summary, we have demonstrated that it is possible to start with any of the structures Hex1P, Hex2P, or Hex3P, and obtain a surface consisting solely of the anchoring strand by first denaturing the central hexagon followed by competitive strand displacement. From the resulting ss **tri-pe** layer it is possible to come full circle, since any of the three structures can be formed from a layer of anchoring strands. This whole process, starting from one structure and finishing with another is demonstrated in Figure 33. (I-II) Two layers with equal amounts of Hex3P are formed, and (III) the

central hexagon is denatured using a high pH solution where the unanchored strands are removed. (IV) The solution is returned to normal buffer, followed by (V) strand displacement using three versions of ss **fc**. Finally, (VI) either Hex1P or Hex2P is formed by addition of prehybridized missing strands, resulting in clearly different frequency changes, indicating that Hex1P and Hex2P are formed at the surface.
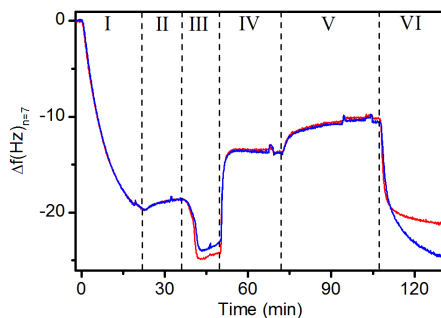

Figure 33. The reversible formation of any of the hexagonal structures on the bilayer membrane demonstrated where two layers of Hex3P are denatured and reassembled to form a layer of Hex1P and a layer of Hex2P. (I) Initial binding of Hex3P (II) buffer rinse (III) exchange to high pH solution (IV) return to normal buffer (V) strand displacement using ss **fc** (VI) formation of Hex1P (blue) or Hex2P (red).

5.2   DNA BASED PHOTOSYNTHETIC COMPONENTS (PAPERS 3-5)

Here we approach the subject of photosynthesis by developing both DNA based light harvesting components as well as a simple reaction center. Focus will be placed on the development of the light harvesting antennae and the simple reaction center will be presented last. Furthermore we have developed a surface attachment technique for DNA origami using porphyrin anchors and surfaces consisting of the amorphous fluoropolymer Teflon AF, which is compatible with fluorescence microscopy imaging and with the components required for our light harvesting systems.

5.2.1   DNA BASED LIGHT HARVESTING ANTENNAE (PAPERS 3 AND 4)

Our approach to light harvesting is very similar to the DNA based systems developed by Armitage and coworkers, employing intercalating YO dyes as initial light absorbers, although they did not study their systems in this context.[195, 196] The DNA constructs we have investigated as scaffolds are drawn to scale in Figure 34 to allow for comparison of their sizes. For ease of reference they have been designated the wire, the pseudo-hexagon (or hexagon for short) and the 2D DNA origami (origami for short). All these systems employ DNA as a scaffold able to hold intercalating YO dyes, which are the light harvesting and energy donor constituents. YO chromophores generally bind to DNA with nearest neighbor exclusion potentially allowing 20 dyes in the wire construct, 50 dyes in the pseudo-hexagon and 3500 dyes in the origami. Covalent modifications of the DNA allow for the specific placement of acceptors in the system,

and the placement of the acceptors in our structures are marked with orange stars in the figure.
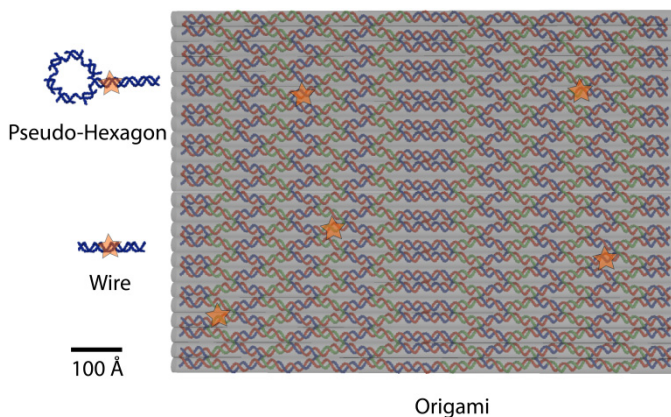

Figure 34. Size comparison between the DNA based light harvesting systems employed in this thesis. The intercalated YO donor dyes have been omitted for clarity, and their incorporation would result in extension and unwinding of the DNA helices. Each structure is drawn to scale. Gray cylinders have been added to the origami structure to aid in visualization. Positions of acceptor dyes are marked with orange stars, and consist of porphyrin modifications for the pseudo-hexagon and wire and the dye ATTO-565 attached to specific staple strands for the DNA origami system.

Already at this stage it is insightful to compare our systems with those found in nature. As was discussed in section 4.1, the main factor which enables efficient light harvesting in natural systems is many light absorbing dye molecules which are able to transfer excitation energy via the homo-FRET mechanism. The chlorophylls are great examples of this, embodying very large oscillator strengths, small Stokes shift, an excited singlet state lifetime in the ns range, and dense packing in protein scaffolds. In section 3.2.1 we considered the intercalation of YO dyes between DNA bases. These dyes have large oscillator strengths when bound to DNA (although smaller than the chlorophylls), small Stokes shift and ns excited singlet state lifetimes. Furthermore, the DNA scaffold ensures that the distance between neighboring YO chromophores is ~10 Å at saturation, and homo-FRET between YO dyes should therefore be efficient. The 10 Å spacing of YOs in DNA is almost identical to the spacing between chlorophylls in the highly ordered $LH2_I$ and LH1 antenna rings in purple bacteria. In terms of antenna size, the pseudo-hexagon ring structure resembles the ring structure of LH1, and both are able to contain ~30 chromophores at saturation. The origami on the other hand is a much larger 2D sheet of connected duplexes. Binding of light harvesting dyes in flat 2D origami resembles the architecture of PS1 (photosystem 1) from higher plants and cyanobacteria,[164, 165] although the origami is a great deal larger. PS1 is known to have evolved later than purple bacteria light harvesting systems, incorporating a higher density of dyes.[162, 163] In many ways the origami system we employ is an evolution of the wire and pseudo-hexagon structures, also allowing higher dye densities which should increase the amount of light harvested by increasing the number of absorbers and by facilitating homo-FRET.

5.2.1.1   WIRE AND PSEUDO-HEXAGON (PAPER 3)

The wire and pseudo-hexagon systems will be presented separately from the origami due to differences in the number and type of terminal energy acceptor used. The wire and pseudo-hexagon contain a covalently attached porphyrin molecule, the same as described in section 5.1 (**tri-pe**), which acts as energy acceptor. There is spectral overlap between the emission of YO and absorption of the porphyrin, allowing hetero-FRET energy transfer. For these light harvesting constructs the porphyrin is free-base, which means it is lacking the central coordinated Zn^{2+} ion. The lack of the metal ion ensures increased fluorescence and ease of detection, yet is not fundamentally necessary.

There are several advantages to using a porphyrin compared to a conventional dye as terminal energy acceptor. Firstly, the porphyrin allows anchoring of the structure to lipid bilayers as described for the systems studied in section 5.1 and discussed in section 3.3.1. In this way the porphyrin is protected from possible hydrophobic interactions with the YO dyes. A clear increase in fluorescence from the porphyrin was observed when in the bilayer compared to in aqueous solution, making detection of the sensitized emission possible. This fluorescence may otherwise be drowned out by the strong fluorescence from YO. Secondly, the porphyrin can act as an electron donor in its excited state, as briefly discussed in sections 3.2.2 and 3.3.1. In this way it may be possible to harness the energy which is harvested and perform electron transfer reactions, similar to those found in photosynthetic systems. This role for the porphyrin is studied further at the end of this section. The assembled light harvesting wire structure bound to liposomes is shown schematically in Figure 35, which also shows a possible energy transfer pathway from an initially excited absorber, via homo-FRET energy transfer to a neighboring dye, and finally through hetero-FRET transfer to the acceptor.
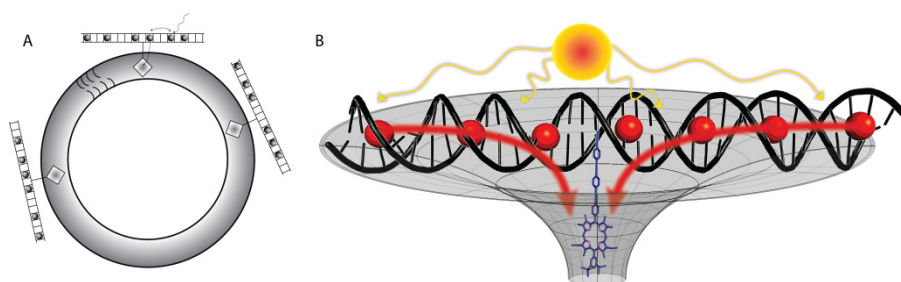
Figure 35. (A) Schematic drawing of the light harvesting assembly consisting of the wire construct anchored to liposomes (not drawn to scale). Porphyrin anchors bind the DNA wires to the liposome, and YO (spheres) binds between DNA bases. The functioning of the system as a light harvesting antenna is shown for the construct bound at the top of the liposome. Energy is initially absorbed by a YO chromophore and subsequently shuttled along the wire via homo-FRET energy transfer until it is transferred to the porphyrin from a nearby YO via the hetero-FRET mechanism. (B) Schematic drawing of a single wire construct with intercalated YO (the membrane is not shown for clarity). The funneling of excitation energy towards the reaction center is depicted with red arrows, and a funnel.

To quantify the functioning of the system in terms of light harvesting ability three parameters were determined. The overall transfer efficiency, E, is the ratio between the quanta of energy transferred to the acceptor and the total number of energy quanta absorbed by the antenna. The antenna effect, AE, is an acceptor specific parameter which is the increase in excitation of the acceptor due to the presence of the antenna (see section 2.4.5). Finally, the related parameter the effective absorption coefficient, ε_{eff}, is the absorption coefficient of the acceptor due to the presence of the antenna. It is proportional to the number of photons harvested by the antenna and transferred to the acceptor. This parameter is therefore independent of the type of acceptor used, and is a good parameter to compare various systems. Unfortunately this parameter is seldom used in the literature, making comparison between different systems and architectures difficult.

Fluorescence emission spectra of the complete wire antenna system upon excitation of the YO energy donor dyes at 480 nm were collected at YO:porphyrin mixing ratios of 2, 5, 10 and 20. The emission spectrum at a ratio of 5 YO:porphyrin is shown in Figure 36A. The sensitized porphyrin emission is clearly evident as the peak at 700 nm. A fluorescence spectrum of the YO-DNA system without an acceptor is also shown displaying higher fluorescence intensity. The YO emission peak decreases when the acceptor is present in the system, since some of the excitation energy transfers to the acceptor instead of being emitted by the donors. The quenching of donor fluorescence can therefore be used to calculate the overall transfer efficiency, E (equation 31). Based on quenching of the donor fluorescence, E was ~50 % for the wire and almost independent of the concentration of YO (Figure 36B). This was at first surprising to us; the increased dye density should increase homo-FRET among the YO dyes due to shorter inter-dye distances, and thereby increase the likelihood of excitation energy being located on a dye close enough to the acceptor for hetero-FRET to occur. This should in turn lead to an increase in transfer efficiency. However, YO self-quenches slightly upon increased density in DNA, thereby also decreasing the probability of homo-FRET (equation 27). In this system the two effects seem to completely balance each other, and constant energy transfer efficiency is observed. The pseudo-hexagon structure displayed E of ~20 %, again irrespective of the density of YO. Fluorescence spectra of the pseudo-hexagon look similar to the wire spectra, but the porphyrin peak is less evident, due to less energy being transferred to the acceptor.

To corroborate the hypothesis that YO self-quenching balances the expected increase in homo-FRET for these systems, simulations of energy transfer were performed for both the wire and the hexagon, based on a Markov chain model. The model is described in detail in section 2.4.4, but briefly it requires the transfer probabilities between every single dye in the system to be applicable. Initially the excitation energy is located on a randomly excited dye. The model subsequently evaluates the probability of excitation being located on each dye in the system after an infinite number of transfer steps. The transfer probabilities are calculated using Förster theory (section 2.4.3), and a probability of the excitation energy leaving the system through other pathways of excited state deactivation is included. To calculate a transfer probability between a pair of dyes in the system, their relative orientations and distances as well as spectroscopic
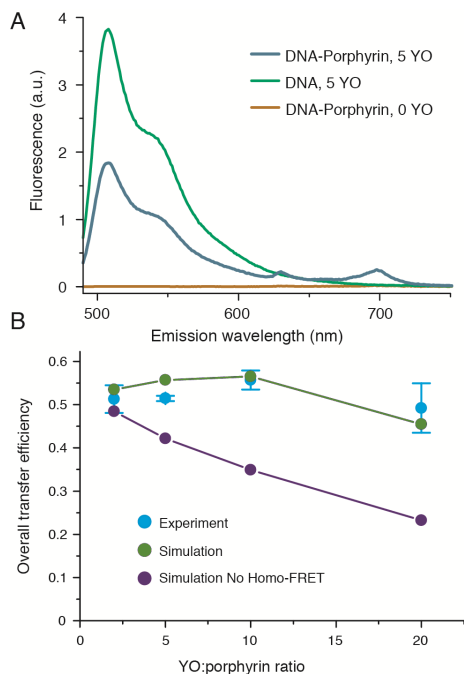
Figure 36. (A) Emission spectra of the wire system with 5 YO:porphyrin without acceptor present (green curve) and with acceptor present (blue curve) upon excitation at the donor absorption wavelength of 480 nm. The brown curve is obtained upon excitation of the DNA-porphyrin system without any YO present. (B) Measured (light blue) and simulated (green) energy transfer efficiency of the wire as a function of YO:porphyrin ratio. Also shown is the simulated transfer efficiency for a system where the probability of homo-FRET is set to zero (purple).

properties are required. In the case of YO the lifetime is known to decrease upon higher binding densities and this is included in the model. Due to the stiffness of the wire construct, the relative positions of all binding sites and distances to the porphyrin from these are well defined, as well as the relative orientation between each site. To simulate the energy transfer efficiency, 10 000 simulations were performed for each mixing ratio. For each of these simulations the actual number of dyes bound to the wire was randomly chosen based on a Poisson distribution around the mixing ratio. Furthermore each dye was allowed to bind randomly in the DNA with nearest neighbor exclusion and the extension and unwinding of the DNA at this site was included. Each simulation starts by randomly choosing an initially excited dye, and the probability that excitation energy ends at the acceptor site is evaluated. The transfer probability to the acceptor is collected for the 10 000 simulations and the average value corresponds to E. The simulated data fit remarkably well with the experiments, likely due to the constrained dynamics of the wire system and the applicability of Förster theory to calculate transfer probabilities (Figure 36B). The pseudo-hexagon was also simulated using a model where the DNA was constrained to a 2D plane, the orientation factor between dyes was set to 2/3, and unwinding of the DNA helices was not included in this case. The simulation still yielded good fits with experimental data,

particularly at low binding densities. It was possible to isolate the effect homo-FRET has on the efficiency of energy transfer in the wire system using the simulation. By setting the rate constant for homo-FRET to 0, E was markedly decreased at higher binding densities, indirectly revealing the effect of homo-FRET. At saturation the simulated system transferred double the amount of energy to the acceptor when homo-FRET was allowed. This shows that homo-FRET among donor dyes is an important mechanism in this system, exactly as it is in natural antenna systems.

It was briefly touched upon in section 2.4.2.2 that when a donor and acceptor are within FRET distance yet are moving in relation to each other, the distribution of donor-acceptor distances can be obtained through fitting of time-resolved fluorescence data. A slightly different, yet related, approach was used here to directly observe the role of homo-FRET. Time-resolved fluorescence data were collected for the wire system both with and without the presence of the acceptor, at the YO:porphyrin ratios already mentioned. The expected fluorescence lifetime for each donor position along the wire in the presence of the acceptor can be calculated from Förster theory based on the donor-acceptor distance, the lifetime of the donor in the absence of the acceptor (obtained at each mixing ratio), and the spectral properties discussed in section 2.4.3. The measured fluorescence decay is then expected to follow equation 48,

$$I_{DA}(t) = irf(t) \otimes \int_{R_{min}}^{R_{max}} \sum_i P(R)\alpha_i \exp[(-t/\tau_i)(1 + \{R/R_0^{DA}\}^6)]dR \qquad (48)$$

where *irf(t)* is the instrument response function, R denotes the donor-acceptor distance, R_{min} and R_{max} are the minimum and maximum donor-acceptor separations respectively, where $R_{min} = R_L$ (the linker length), *P(R)* is the apparent distance distribution function, α_i and τ_i are the intrinsic donor amplitudes and lifetimes respectively (without the presence of acceptor), and R_0^{DA} is the Förster distance. A one-dimensional Lorentzian distribution was used to describe the donor-acceptor distances,

$$P(R) = \frac{2I}{\pi}\left[\frac{\gamma^2}{4(R-R_L)^2+\gamma^2}\right] \qquad (49)$$

where I and γ are the height and width of the distribution, respectively.

The distribution function *P(R)* is obtained through the fitting procedure. YO binds randomly so that no matter which binding ratio is used, the probability that a given site is occupied is equal for all sites. *P(R)* is expected to be flat at very low YO concentrations because the YOs do not interact and every position contributes the same amount to the decay due to the random binding. As the concentration of YO increases, *P(R)* is expected to contain larger contributions from dyes in close proximity to the acceptor (small values of R), and smaller contributions from dyes further away from the acceptor (large values of R), due to the advent of homo-FRET. Homo-FRET allows excitation energy to jump between the dyes. Thereby an excited dye far away from the acceptor has a probability of transferring its excitation energy to a site near the acceptor, where the probability of hetero-FRET is larger. This means that a portion of the excitation energy which would normally dissipate without energy transfer to the acceptor instead participates in hetero-FRET and quenches the donor fluorescence.

P(R) should therefore weigh smaller values of *R* more than larger values of *R* as the YO density increases. The experimentally obtained values of *P(R)* are shown in Figure 37 showing this exact trend.
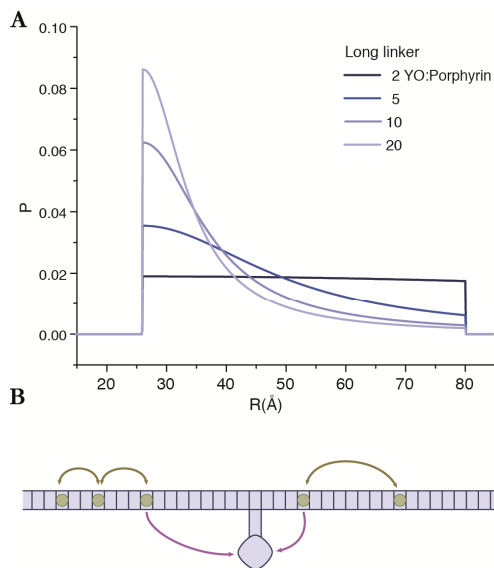

Figure 37. (A) Apparent donor-acceptor distance distribution shown as the probability P versus donor-acceptor spacing R, at the YO:porphyrin mixing ratios of 2, 5, 10, and 20. (B) Schematic diagram of the homo- and hetero-FRET processes which give rise to the observed changes in P(R) as a function of YO:porphyrin mixing ratio.

Although the measured transfer efficiencies of the wire and pseudo-hexagon systems were constant irrespective of the concentration of YO dyes, this does not mean that the light harvesting ability of the constructs was independent of YO concentration. As the dye density increases there are more light absorbers per acceptor and more light is therefore absorbed. Subsequently more energy is transferred to the acceptor even if the transfer efficiency does not change. This is demonstrated through calculation of *AE* and ε_{eff}. These values were obtained by studying the excitation spectra of the constructs while monitoring the emission from the porphyrin at 700 nm (Figure 38). The fluorescence intensity of the acceptor increases with the concentration of YO when excitation occurs in the donor area of the spectrum (480-530 nm), since more energy is absorbed by the donors and consequently more energy is transferred to the acceptor. In the region of the spectrum where only the porphyrin absorbs (530-600 nm) no changes are observed as the YO concentration increases, since this does not result in increased light absorption at these wavelengths. At saturation binding densities, *AE* for the wire reached a value of 12, meaning that 12 times more emission from the porphyrin is observed upon excitation of YO, compared to when the porphyrin is directly excited at its peak absorption. For the pseudo-hexagon *AE* reaches 17 at saturation. It is interesting to note that the pseudo-hexagon clearly performed better than the wire in terms of the amount of energy harvested, although the transfer efficiency was lower. This is of course a consequence of the higher number of donor

dyes in the hexagon system, which allows more energy to be absorbed, although a lower percentage of this energy reaches the acceptor compared to the wire construct. The effective absorption coefficients were determined to be 2.6×10^5 $M^{-1}cm^{-1}$ and 3.7×10^5 $M^{-1}cm^{-1}$ for the wire and pseudo-hexagon respectively, and allow comparison of the performance of the wire and pseudo-hexagon with DNA origami in terms of amount of light harvested.
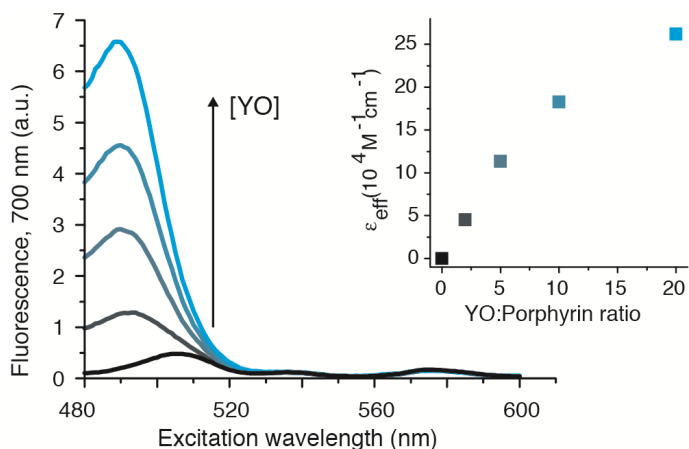

Figure 38. Excitation spectra measured at the porphyrin emission wavelength (700 nm) upon increasing YO:porphyrin ratio (2, 5, 10, and 20 YO:porphyrin). Inset shows the corresponding increase in effective absorption coefficient.

5.2.1.2   DNA ORIGAMI (PAPER 4)

Compared to the wire and hexagon, the DNA origami system is enormous. In terms of YO chromophores, roughly 3500 can bind at saturation (assuming nearest neighbor intercalation binding). The fluorescence signal from YO is therefore staggering, and a ratio of porphyrin:YO similar to those used for the wire would be necessary to harvest enough energy for a clear sensitized emission signal, due to the poor fluorescence properties of the porphyrin. This translates to hundreds of porphyrins and was not feasible, so we instead turned to the dye ATTO-565 as acceptor. This dye has a very high absorption coefficient of 1.2×10^5 $M^{-1}cm^{-1}$, which is nearly an order of magnitude higher than for the porphyrin, thereby directly increasing the rate constant for hetero-FRET transfer. ATTO-565 also has a high fluorescence quantum yield which eases the detection of sensitized emission. Even so, as shown in Figure 34, 5 acceptors were placed on the origami to ensure a clear signal. The drawback is of course that binding to liposomes is not possible, nor is the dye a good electron donor in its excited state. The bis-intercalating homo-dimer YOYO was used instead of YO to increase the binding constant to DNA. This was necessary due to the high ionic strength of the buffer used with the origami. Again E, AE, and ε_{eff} were used as parameters to quantify the light harvesting process. When bound to DNA, the two chromophores of YOYO are electronically only weakly coupled as supported by the unperturbed

absorption spectrum, and can be treated as two separate YO chromophores. This is done below in analyzing the results and modeling the transfer.

Normalized fluorescence spectra of the origami antenna upon excitation of the YOYO donors are shown in Figure 39A. Again the sensitized emission from the acceptors is clearly observed, now as a peak at 590 nm. At a mixing ratio of 3500 YOYO:origami (~ 7000 chromophores per origami) the fluorescence was suddenly heavily quenched and shifted to longer wavelengths (inset in the figure) accompanied by changes in the absorption spectrum which indicated that a large amount of free dye was present. This was attributed to the integrity of the origami system being compromised at high YOYO densities. It was not possible to calculate E based on the donor quenching as was done for the wire and hexagon due to problems in controlling the concentration of origami in the samples. E was instead calculated directly from the emission spectra using the quantum yields of the donor and acceptor, and the ratio between the integrated emission corresponding to each emitting species (equation 38). As for the wire and pseudo-hexagon, E was relatively independent of the density of donor chromophores. Values of E in the range of 13 % were obtained, which is surprisingly high considering the large number of donors and relatively few acceptors present in the system.
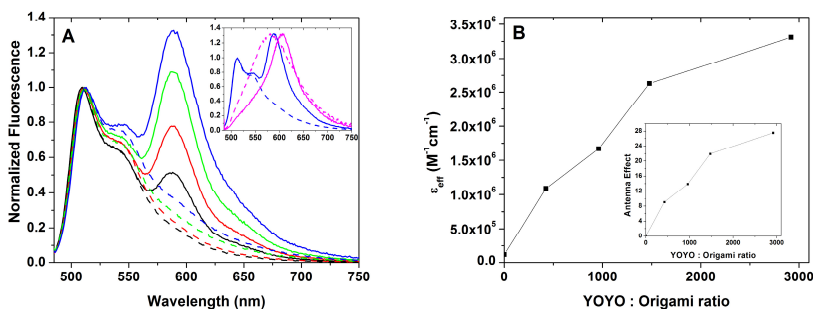

Figure 39. (A) Normalized fluorescence spectra of the YOYO-origami-ATTO-565 system with increasing YOYO: origami mixing ratio (black: 380, red: 980, green: 1500, and blue: 2960). Dotted lines are measurements without the acceptor ATTO-565 and full lines are obtained with the acceptor. Inset shows a comparison between the YOYO:origami mixing ratios of 2960 and 3500 (blue). (B) Effective absorption coefficient at the same YOYO:origami mixing ratios as shown in (A). Inset shows the corresponding antenna effect.

As for the wire and hexagon, AE and ε_{eff} were calculated and are shown as a function of YOYO:origami mixing ratio in Figure 39B. AE reached a value of 28 at saturation, around twice as high as for the wire and hexagon. It is important to note that each acceptor displays an increase in excitation by 28 times. This may still not seem very impressive compared to the values obtained for the wire and hexagon, but we must remember that AE is the increase in acceptor excitation due to the antenna, and the acceptor is different for the origami compared to the wire and pseudo-hexagon. In this case the much lower absorption coefficient of the porphyrin compared to ATTO-565 means that only a small amount of energy transfer to the porphyrin results in large values of AE. To compare the two systems one should instead use ε_{eff}, which reached a

value of 3.2×10^6 M^{-1}cm^{-1} at YOYO saturation, roughly an order of magnitude larger than for the wire and pseudo-hexagon structures. The effective absorption coefficient for each ATTO-565 acceptor is thereby comparable to the effective absorption coefficient of purple bacteria light harvesting systems grown under high light conditions (see section 4.1). The origami system could therefore in principle supply a reaction center similar to the one found in purple bacteria with enough excitation energy to optimize its turnover under high light conditions, based on its absorption coefficient. When one takes into account the area of the solar spectrum where YOYO absorbs (~500 nm) compared to the purple bacteria systems (~800 nm) the actual amount of light absorbed increases by 1.5 times, since the irradiance from the sun is 1.5 times as intense at 500 nm compared to 800 nm.

The value of ε_{eff} in combination with the measured transfer efficiency of 13 % can be used to gauge the actual density of donor dyes bound to the origami at saturation. From the mixing ratios it is clear that not all dyes are binding to the origami, since the mixing ratio of 2960 corresponds to 5920 individual YO chromophores, and is higher than the number of binding sites per origami, indicating that at least some YOYO are free in solution. The total ε_{eff} for all five acceptor dyes is 16×10^6 M^{-1}cm^{-1}. Based on the measured transfer efficiency this value is 13 % of the total absorption coefficient of all the YO chromophores in a single origami, which then must be 123×10^6 M^{-1}cm^{-1}. Each YO chromophore has an absorption coefficient of 5×10^4 M^{-1}cm^{-1} meaning that roughly 2460 YO chromophores are bound to the origami at the highest mixing ratio before its structural integrity is compromised, which translates to ~500 chromophores per acceptor. This is a large number considering that the origami is constrained due to crossovers. Elongation and unwinding due to intercalation should therefore be hindered. In contrast, the wire and hexagon can more easily accommodate intercalating dyes by helix expansion and unwinding.

Again the transfer of energy was simulated to gain a better understanding of the underlying mechanisms and specifically to investigate the effect homo-FRET has on the terminal transfer efficiency (efficiency of transfer to any acceptor). To model the DNA origami as was done for the wire is not feasible since the 3D structure of the origami and the effect caused by intercalation is not well established. Furthermore the origami is expected to be relatively flexible in solution, yielding further parameters which must be accounted for. Instead, a very simple model of the YOYO-origami-ATTO-565 system at saturation was performed, setting the orientation factor between donor dyes to 2/3. Nearest neighbor binding was assumed for simplicity. The origami itself was modeled as 24 parallel duplexes with an inter-duplex spacing of 31 Å (termed the Y direction) as shown in Figure 40. Each duplex contains a row of 144 evenly spaced YO chromophores with a spacing of 9.4 Å due to nearest neighbor exclusion (termed the X direction). This results in origami dimensions which are 1344 Å in the X direction by 713 Å in the Y direction (see Figure 40) with a total of 3456 YO chromophores. The extension of the origami due to intercalation has thereby been restricted mainly to the X direction. The placement of the acceptors in X and Y direction is also shown in Figure 40 as green spheres, and they were placed 2 nm from the plane of the origami due to the linker used. At saturation there is only a single configuration of dyes, and the system is completely determined. The Markov chain

model was used to evaluate the probability of terminal energy transfer as the initial excitation was moved to each individual YO chromophore in the system (Figure 40). Initially excited donor dyes in close proximity to an acceptor display terminal transfer probabilities of ~58 %, whereas initially excited donor dyes far away from any acceptors display terminal transfer probabilities as low as 4 %. The average transfer efficiency from all donors yielded E, which was simulated to be 16 %, in good agreement with the measured value of 13%.

By studying excitation of dyes far away from the acceptors we can get a sense of the effect of homo-FRET on the terminal transfer efficiency, since transfer from these dyes requires many homo-FRET steps to reach an acceptor. For a single YO donor and ATTO-565 acceptor without the presence of other dyes, a (hetero-FRET) transfer efficiency of 4 % is reached at a distance of ~70 Å. In the origami system, where homo-FRET is possible, a transfer efficiency of 4 % is reached from dyes which are 240 Å away from an acceptor, demonstrating that homo-FRET allows the excitation to probe the 2D space of the origami, and subsequently transfer to an acceptor if the intervening distance becomes sufficiently small. Also, the average number of homo-FRET steps from each initially excited dye is obtained from the modeling. This revealed that each excitation takes between 1500 and 3300 homo-FRET transfer steps. This value is likely exaggerated since the measured origami contained only ~2500 bound donor dyes, not 3500. However, it still demonstrates that homo-FRET is an integral part of the system ensuring relatively large transfer efficiencies over large distances.
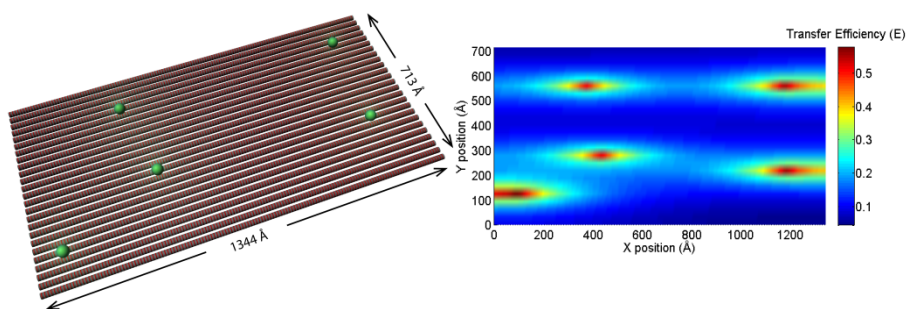
Figure 40. Simulation of DNA origami light harvesting antenna. To-scale cartoon of the modeled system is shown on the left where origami is represented as gray cylinders, YO chromophores are red and acceptors are green spheres. On the right is shown the simulated terminal transfer efficiency from every YO chromophore position in the system.

5.2.1.2.1   SURFACE ATTACHMENT OF DNA ORIGAMI

Anchoring of DNA origami to lipid bilayers using porphyrin modified staple strands was attempted but revealed that the DNA origami itself associates strongly with supported lipid bilayers, and induces aggregation of liposomes in solution. This effect is likely a consequence of the divalent Mg^{2+} ions in solution creating bridges between the origami and lipid layers. Instead we focused on binding DNA origami to hydrophobic Teflon AF (an amorphous fluoroplast of Teflon) and nano-patterned Teflon AF, again

using porphyrin modified staple strands as anchor. The porphyrins were placed on the same bases as the ATTO-565 acceptors used above in Figure 40, resulting in anywhere from 1-5 anchors depending on which staple strands were added. Each porphyrin is thereby placed on the same side of the origami, protruding perpendicularly from the surface. The system was mainly investigated using single molecule TIRF microscopy to study the placement and number of DNA origami attached to the surface. For these measurements five staple strands modified with the fluorescent dye ATTO-647N were added. Staple strands near the porphyrin modifications were chosen as sites for the fluorescent labels, and anywhere between 1 and 5 fluorescent labels could thus be applied at a time.

The effect of the number of porphyrin anchors on the binding of DNA origami to Teflon AF was probed by allowing a 40 pM solution of origami with varying number of porphyrins to bind to the surface for 1 minute. The surface was subsequently rinsed for 20 seconds and then re-immersed in buffer for imaging. The number of bound porphyrins per 40 μm × 40 μm area was counted, and the data for 0, 1, 3, and 5 porphyrins are shown in Figure 41. Without the porphyrin anchor present only a few structures adhere to the surface, proving that the origami does not itself interact strongly with the surface. As the number of anchors increases a non-linear increase in the number of bound origamis is observed, reaching ~600 with 5 anchors. The binding was strong, and no surface desorption was observed after several hours in buffer, even with only a single anchor. The effect of incubation time was studied by allowing a solution with a single anchor to bind for up to 3 hours, revealing a surface density of constructs approaching that obtained with five anchors. The observed difference in binding density between structures with different number of anchors was therefore mainly attributed to an increased binding rate.
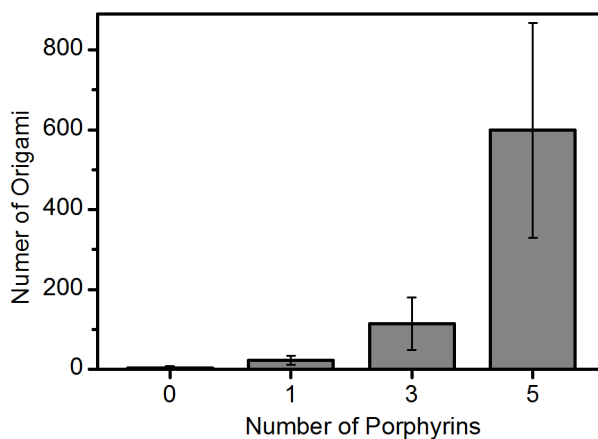

Figure 41. Number of DNA origami bound per 40 μm × 40 μm Teflon AF surface area, as a function of the number of porphyrin anchors per origami. Standard deviations based on three measurements.

In addition to the strong binding to Teflon AF the bound origami did not diffuse on the surface which allowed for a determination of the positioning of the fluorescent

dyes using STORM (stochastic optical reconstruction microscopy). Origamis with 5 porphyrins and 1-3 fluorescent modifications were investigated, and the inter-dye distances obtained from the analysis matched well with the expected distances obtained from a model of the 2D DNA origami provided by the SARSE program.[31] This demonstrates the possibility provided by DNA origami to selectively modify features at the resolution of a single DNA base. However, the structures themselves are still randomly distributed over the surface.

In addition to the molecular scale modifications afforded by the origami we also demonstrated that the origamis themselves, as well as origami based light harvesting constructs, could be placed at predetermined positions on the surface. To accomplish this, nano-scale patterning of the surface was required. As discussed in section 3.2.2 DNA origami has previously been attached to nano-patterned positively charged surfaces. The drawback with these techniques is that it is the DNA itself which interacts, meaning that it is difficult to select which face binds to the surface, and that high concentrations of divalent ions are often require. These ions interfere with intercalation which is a drawback for forming light harvesting constructs on the patterned surface. The Teflon AF is a good alternate surface to use. It can be patterned using electron beam lithography allowing feature sizes down to 50 nm. Teflon AF which has not been exposed to the e-beam treatment is subsequently washed away, leaving only the patterned areas. The pattern consisted of islands with dimensions similar to those of the origami, designed so that each island should bind one origami. The origami was again modified with porphyrin anchors to allow specific binding. The pattern and island dimensions are shown in Figure 42. Each island was patterned with a distance of 1000 nm to its nearest neighbor to ensure that each island is clearly resolvable using diffraction limited fluorescence microscopy. Figure 43A shows AFM micrographs of the nano-patterned surface.
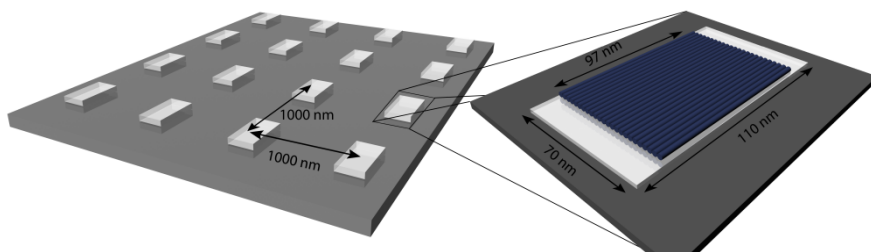
Figure 42. Schematic drawing of the Teflon AF nano-patterned surface showing the dimensions of the surface features, and inter-feature distance (not drawn to scale). Enlargement shows a single Teflon AF island with bound DNA origami.

A fluorescence micrograph of DNA origami with 5 fluorophores, bound to the nano-patterned islands via 5 porphyrin anchors, is shown in Figure 43B. The origami bound selectively to the patterned islands when porphyrin anchors were incorporated but no binding was observed without the porphyrin anchors present. Based on the fluorescence micrographs obtained using 5 porphyrin anchors and 5 fluorophores, 85 ± 10% of the islands contained bound porphyrins. The red rings in the figure indicate positions which did not have a bound origami.
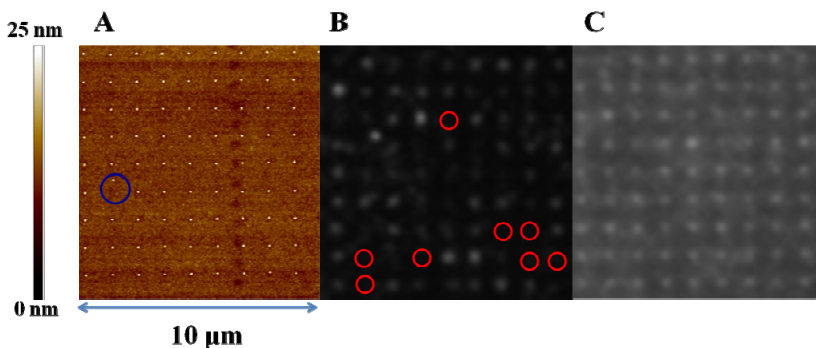
Figure 43. (A)AFM micrograph of nano-patterned Teflon AF islands on glass. (B) TIRF micrograph of ATTO-647N fluorescently labeled DNA origami attached to Teflon AF islands. The area shown is the same size as in (A). (C) Similar area as in (B) after addition of YOYO solution. It is the YOYO fluorescence which is shown in the micrograph.

The ability of Teflon AF nano-patterned islands to act as substrates for binding DNA origami based light harvesting constructs was investigated. The principle requirement for this is that the porphyrin must be able to anchor DNA origami to the Teflon AF, even in the presence of YOYO. Binding of pre-incubated DNA origami and YOYO to Teflon AF islands yielded less bound structures based on ATTO-647N fluorescence compared to when the origami was allowed to bind first, followed by addition of YOYO. Using the latter procedure no origami desorbed from the surface, showing that the binding remained intact. By monitoring the fluorescence from YOYO as shown in Figure 43C, it was revealed that YOYO bound to all islands, not only to islands containing origami. There is likely competition between the YOYO and porphyrin for surface binding sites, explaining why DNA origami pre-incubated with YOYO bound less to the surface. However, it was shown that all the necessary components for a DNA based light harvesting system including YOYO and covalently attached fluorophores could be collected at predefined surface positions.

5.2.2   BIO-INSPIRED "REACTION CENTER" (PAPER 5)

As discussed in section 4.1 the photosynthetic reaction center is comprised of a series of precisely positioned bacteriochlorophylls and bacteriopheophytins allowing rapid electron transfer processes and charge separation. We have developed a bis-porphyrin binding pocket consisting of two DNA strands which precisely position the porphyrin modifications relative to each other (Figure 44). The modifications are identical to those described in section 5.1.1 and termed **tri-pe**. One porphyrin is covalently coupled to each strand, and in duplex form there is a single base-pair between the two modifications. In this way the two porphyrins are reminiscent of the "special pair" chlorophylls found in photosynthetic reaction centers. Indeed, intermediate electronic coupling was observed for these species, where the dimer has a clearly different emission spectra compared to the monomer.
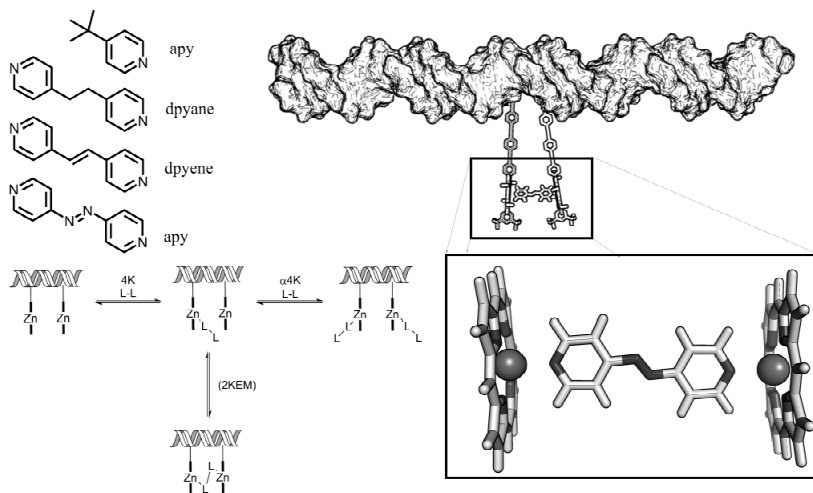
Figure 44. (Top left) Chemical structure of ligands. (Right) Bis-porphyrin binding pocket with bound bidentate molecule apy. (Bottom left) Possible states of the bis-porphyrin system as the concentration of ligand increases, and equilibrium constants for the processes which transfer the system between states.

The bis-porphyrin reaction center was developed to selectively bind bidentate ligands in-between the two porphyrins. Inspiration is not only drawn from photosynthetic reaction centers, but also from enzymes and their ability to catalyze reactions by binding substrates in specific orientations. Upon photoexcitation of the porphyrin dimer, reduction of the ligand is possible if the driving force for electron transfer is sufficient ($\Delta G^0 < 0$, equation 42). A successful system should therefore be able to both bind the ligands in-between the porphyrins as well as oxidize ligands if the driving force is sufficient. To demonstrate the latter, three ligands were chosen with varying reduction potentials, apy which should be easily reduced, dpyene with close to zero driving force, and dpyane which should not be reduced (Table 1). Both binding between the porphyrins and photoinduced electron transfer were probed using a spectrofluorometric titration wherein the ligand is added in small aliquots to a solution of the dimeric porphyrin pocket, see Figure 45. Fluorescence quenching is expected for ligands where photoinduced electron transfer is operating. Furthermore, changes in the fluorescence spectrum of the porphyrin dimer are expected upon coordination of the ligand to the zinc ion.

The results from the titration are plotted in Figure 45 for all the ligands, and the degree of fluorescence quenching is collected in Table 1. As expected based on the reduction potentials, no quenching is observed for py and dpyane, whereas apy is heavily quenched. For dpyene intermediate quenching is observed, although the driving force is positive. This is likely due to the simplified calculation of the driving force which assumes a spherical shape for the electron donor and acceptor. Furthermore, there is likely strong electronic coupling between the porphyrins and the ligand which mediates the electron transfer.

To probe if the ligands are preferentially binding between the porphyrins, the data from the titration were fitted to equation 50 which is based on a model of coupled equilibria between four solution species as shown in Figure 44. The simplest of these species is the pocket without any ligand bound. This species is in equilibrium with an intermediate species where one end of the ligand is bound, but the other is still free (PP-L). From this intermediate, either another ligand can bind, yielding a species with two porphyrins and two ligands (L-PP-L), or the ligand can also bind with the other site, creating the desired species of the porphyrin pocket with the ligand bound in-between (P-L-P). The allosteric effect α in equation 50 relates the binding strength of the ligand to the first site to the binding strength to the second site, and was obtained for the monodentate ligand py and assumed to have the same value for the bidentate ligands. The most important factor to consider from equation 50 is the effective molarity (EM) defined in equation 51, which is related to the additional binding strength obtained from forming the doubly bound species as compared to the singly bound species and collected for the various ligands in Table 1.

$$\theta = \frac{2KL+8K^2EML+16K^2\alpha L^2}{1+4KL+8K^2EML+16K^2\alpha L^2} \tag{50}$$

$$2K \times EM = \frac{[P-L-P]}{[PP-L]} \tag{51}$$

In the above equations θ is the fraction of coordinated porphyrin, K is the equilibrium for binding of the ligand to single porphyrin, and L is the concentration of free ligand in solution.
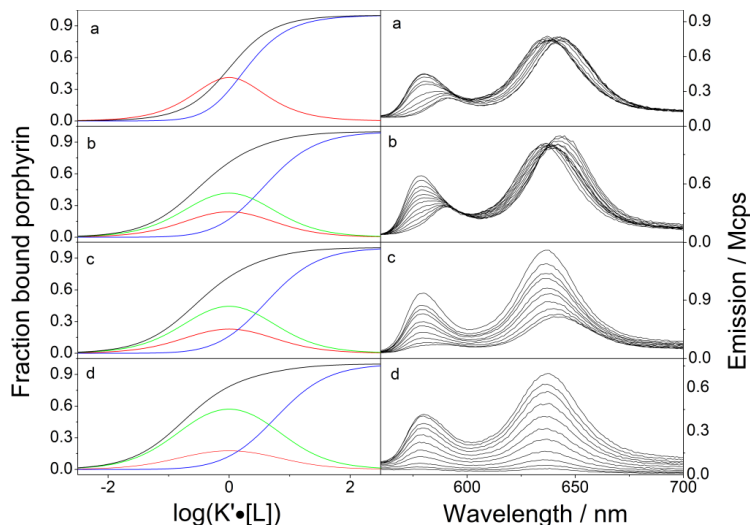
Figure 45. Left panel shows the fraction of each of the three (two in a) porphyrin-ligand species as the concentration of ligand is increased for the ligands (a) py (b)dpyane (c) dpyene and (d) apy. The black curve shows the total fraction of porphyrin sites with bound ligands. The red curve represents PP-L, the blue curve represents L-PP-L and the green curve represents the ligand bound between the two porphyrins P-L-P. Right panel shows corresponding fluorescence emission spectra for the titrations.

From the analysis of the titration data the fraction of the three ligand bound species, PP-L, P-L-P and L-PP-L are obtained as a function of ligand concentration and have been plotted in Figure 45. Although the effective molarities are relatively low, the analysis reveals that the species where the ligand is bound in-between the two porphyrins, P-L-P, is the major species over a wide range of ligand concentrations. As the ligand concentration increases the dominating species will be the pocket with two bound ligands.

Table 1. Reduction potentials, driving force for electron transfer, fluorescence quenching and effective molarity for the ligands py, dpyane, dpyene and apy.

Ligand	Reduction potential vs SHE (V)[a]	ΔG^0 (eV)	Fluorescence quenching (%)	EM (M)
py	-2.86[198, 199]	1.515	0 %	-
dpyane	-2.86[198, 199]	1.515	0 %	0.029
dpyene	-1.69[199]	0.435	60 %	0.024
apy	-0.59[200]	-0.755	95 %	0.045

6 CONCLUDING REMARKS

The field of DNA nanotechnology is progressing from one of novel structure formation and design to one of functional constructs. In this endeavor it can be useful to think of the functionalized structures as self-assembled machines. In the long run, DNA based machines could have a number of different modifications allowing them to perform specific functions. DNA origami offers a platform where such functional groups can be placed with molecular precision, on ~230 modifiable staple strands. In this context surface attachment of the machines will be necessary for many applications, and for integration with current surface based micro-circuitry.

In this thesis several modifications of DNA constructs were presented which added functionality to the DNA. A porphyrin anchor allowed strong binding to lipid bilayers, while keeping the DNA in buffered solution. The bilayers could either be in the form of liposomes in solution or surface supported. Once attached to the bilayer DNA structures were shown to disassemble and reassemble upon external stimuli, just as they would in buffered solution, opening a pathway for the exchange of structural and functional components. Furthermore, the lipid environment imparts mobility to the surface attached structures, yielding diffusing DNA machines. One could imagine a surface based machine performing several consecutive operations with different functional groups at different surface sites, or one could image reforming structures which had degraded, through a self-healing process. The porphyrin could also anchor the DNA to hydrophobic surfaces, as exemplified through binding of DNA origami to Teflon AF surfaces. This allows for the irreversible positioning of DNA structures on the macro scale, with molecular positioning of functional components.

The porphyrin moiety is not only an anchor; it also possesses a more direct functionality through its favorable property as a reduction agent in its excited state. We demonstrated this using two porphyrins, placed at specified positions on a DNA duplex scaffold. The distance between the porphyrins was designed to accommodate a bidentate ligand. It was the molecular precision afforded by DNA modification which allowed this construction to be made. Depending on the reduction potential of the ligand it was either reduced or not when a porphyrin was excited. We showed that the doubly bound species consisting of the ligand between the porphyrins was the major species over a wide range of ligand concentrations. Electron transfer reactions as demonstrated here are important also in biological contexts, as they provide a means to store energy to be used later to power cellular functions. They could equally provide power for DNA-based nano-machines. In this context extremely long lived charge separated states are desired. Our design proved insufficient in this regard, since there was a rapid back-electron transfer. However, a great deal of research is focused on synthesizing components which generate true charge separation over long time scales, and there is no reason to suspect that these cannot be integrated into DNA based systems in the future.

A final DNA modification we demonstrated was the use of DNA intercalating pigments to mimic photosynthetic light harvesting. The pigments are spaced in the DNA similarly to pigments in natural light harvesting protein scaffolds. We showed

that the transfer of energy from the pigments to a covalently attached acceptor molecule on the DNA is efficient, and that homo-FRET transfer among the intercalated pigments plays an important role in increasing the overall number of excitations transferred to the acceptor. By using DNA origami as the scaffold we showed that a staggering number of pigment chromophores could be incorporated, and the amount of excitation energy transferred to an acceptor was comparable to some natural light harvesting systems. Using the DNA itself to accommodate light harvesting pigments is an intriguing avenue to pursue to provide power for DNA based machines. The light absorbed by the pigments is transferred to positions which are placed with molecular accuracy on the DNA. Functional groups which use this energy could be placed at these positions, for example in the form of photo-catalytic moieties. In this way the DNA machine is self-powered through the use of solar energy.

It is always difficult to predict the future course of research. However, there are several concrete goals related to this research which would greatly improve the applicability of these structures. One such goal is to control the diffusion of the DNA constructs in the lipid membrane both in terms of speed and direction. Thermo-responsive lipid bilayers may provide an avenue to the former. These bilayers have phase transitions above room temperature, providing a static gel phase and dynamic liquid crystalline phase depending on temperature.[201] DNA constructs anchored to such lipid bilayers could therefore be switched from a mobile to immobile state, simply by changing the temperature. To change the direction of DNA diffusion in the lipid bilayer may prove more difficult, but it has been shown that the bulk spreading of supported lipid bilayers can be controlled using a viscous shear force.[202, 203]

In section 4 the notion of an energy cascade to funnel excitation energy towards desired acceptor sites was discussed. In the work on light harvesting constructs presented in this thesis (section 5.2.1) such a gradient is not present, other than the single step between the donor pigments and the acceptor. Incorporating further steps into the gradient will increase the directionality of the energy flow, and provide an increase in transfer efficiency. Recent unpublished work in our group has shown that the use of two different types of intercalating dyes, providing an energy gradient through predefined positioning on a DNA scaffold, is extremely difficult to accomplish due to the labile nature of intercalative binding. Instead, future research should attempt to incorporate other self-assembled light harvesting components, not based on DNA. Another general lesson from natural systems is that dense packing of donor dyes allows for more efficient terminal energy transfer due to increases in homo-FRET. For DNA origami systems one can envision moving to 3D scaffolds to increase the density of intercalating sites. In this approach it is likely that the structural changes wrought by the intercalation process must be considered explicitly as demonstrated recently.[204] In this work the DNA origami was made under torsional strain which stabilized the structure upon intercalation. DNA origami staple strands also allow for the positioning of photo-catalytic groups on staple strands. It would be interesting to combine these with our light harvesting constructs, thereby yielding increased catalytic turnover.

No matter what the future brings, the progression of DNA nanotechnology looks to be a bright one.

7 ACKNOWLEDGEMENTS

I would like to thank the following people:

My supervisor **Bo Albinsson** – For great inspiration and for providing interesting projects

My co-supervisor **Sofia Svedhem** – You have been a good support and inspiration, always ready with new ideas, and helpful suggestions

My co-authors for their contributions to the various papers, especially

Karl – For introducing me to the lab and the porphyrin-DNA system

Jonas – For your out-of-the-box thinking and ideas

Patrik, **Mehrnaz** and **Aldo** – For good discussions and new areas of research

Everyone at physical chemistry – It has been a fun five years!

Anke – for great friendship over the years, and for reading my thesis

Søren – for your friendship, and of course, the ping-pong games

My office-mates **Nisse**, **Lisha**, **Lulu**, and **Masoumeh** – for giving the work-place a good atmosphere

All of my family

Kristian and **Øyvind** for reading this thesis

And most of all **Mari** – For all your love and support!

8 REFERENCES

1.   Ferain, I.; Colinge, C. A.; Colinge, J. P. *Nature* **2011,** *479*, 310-316.
2.   Feynman, R. P. *Microelectromechanical Systems, Journal of* **1992,** *1*, 60-66.
3.   Lee, C. C.; MacKay, J. A.; Frechet, J. M. J.; Szoka, F. C. *Nat. Biotechnol.* **2005,** *23*, 1517-1526.
4.   Seeman, N. C. *Nano Lett.* **2010,** *10*, 1971-1978.
5.   Lakowicz, J. R., *Principles of Fluorescence Spectroscopy.* 3 ed.; Springer: New York, 2006.
6.   Parson, W. W., *Modern Optical Spectroscopy.* Springer-Verlag: Heidelberg, 2007.
7.   Jablonski, A. *Nature* **1933,** *131*, 839-840.
8.   Dirac, P. A. In *The quantum theory of the emission and absorption of radiation*, Proc. Royal Soc. London, Series A, 1927; 1927; p 243.
9.   Condon, E. U. *American Journal of Physics* **1947,** *15*, 365-374.
10.   Franck, J. *Transactions of the Faraday Society* **1926,** *21*, 0536-0542.
11.   Condon, E. U. *Physical Review* **1928,** *32*, 0858-0872.
12.   Kasha, M. *Discussions of the Faraday Society* **1950**, 14-19.
13.   Strickler, S. J.; Berg, R. A. *J. Chem. Phys.* **1962,** *37*, 814-&.
14.   Ross, R. T. *Photochem. Photobiol.* **1975,** *21*, 401-406.
15.   Seybold, P. G.; Gouterma.M; Callis, J. *Photochem. Photobiol.* **1969,** *9*, 229-&.
16.   Einstein, A. *Physikalische Zeitschrift* **1917,** *18*, 121-128.
17.   Haas, E.; Wilchek, M.; Katchalskikatzir, E.; Steinberg, I. Z. *Proc. Natl. Acad. Sci. U. S. A.* **1975,** *72*, 1807-1811.
18.   Dexter, D. L. *J. Chem. Phys.* **1953,** *21*, 836-850.
19.   Forster, T. *Annalen Der Physik* **1948,** *2*, 55-75.
20.   Forster, T. *Naturwissenschaften* **1946,** *33*, 166-175.
21.   Beljonne, D.; Curutchet, C.; Scholes, G. D.; Silbey, R. J. *The Journal of Physical Chemistry B* **2009,** *113*, 6583-6599.
22.   Engel, G. S.; Calhoun, T. R.; Read, E. L.; Ahn, T.-K.; Mancal, T.; Cheng, Y.-C.; Blankenship, R. E.; Fleming, G. R. *Nature* **2007,** *446*, 782-786.
23.   Panitchayangkoon, G.; Hayes, D.; Fransted, K. A.; Caram, J. R.; Harel, E.; Wen, J.; Blankenship, R. E.; Engel, G. S. *Proc. Natl. Acad. Sci. U. S. A.* **2010,** *107*, 12766-12770.
24.   Collini, E.; Wong, C. Y.; Wilk, K. E.; Curmi, P. M. G.; Brumer, P.; Scholes, G. D. *Nature* **2010,** *463*, 644-U69.
25.   Hildner, R.; Brinks, D.; Nieder, J. B.; Cogdell, R. J.; van Hulst, N. F. *Science* **2013,** *340*, 1448-1451.
26.   Carlsson, C. L., A.; Björkman, M.; Jonsson, M.; Albinsson, B. *Biopolymers* **1997,** *41*, 481-494.
27.   Hannestad, J. K.; Sandin, P.; Albinsson, B. *J. Am. Chem. Soc.* **2008,** *130*, 15889-15895.
28.   McNaught, A. D.; Wilkinson, A., *IUPAC. Compendium of Chemical Terminology.* 2 ed.; Blackwell Scientific Publications: Oxford, 1997.
29.   Cussler, E. L., *Mass Transport in Fluid Systems.* Cambridge University Press: Cambridge, UK, 1997.
30.   Jönsson, P.; Jonsson, M. P.; Tegenfeldt, J. O.; Höök, F. *Biophys. J.* **2008,** *95*, 5334-5348.

31.   Andersen, E. S.; Dong, M.; Nielsen, M. M.; Jahn, K.; Lind-Thomsen, A.; Mamdouh, W.; Gothelf, K. V.; Besenbacher, F.; Kjems, J. *ACS Nano* **2008,** *2*, 1213-1218.

32.   Heilemann, M.; van de Linde, S.; Schuttpelz, M.; Kasper, R.; Seefeldt, B.; Mukherjee, A.; Tinnefeld, P.; Sauer, M. *Angewandte Chemie-International Edition* **2008,** *47*, 6172-6176.

33.   Wolter, S.; Schuettpelz, M.; Tscherepanow, M.; Van de Linde, S.; Heilemann, M.; Sauer, M. *Journal of Microscopy-Oxford* **2010,** *237*, 12-22.

34.   Höök, F.; Kasemo, B.; Nylander, T.; Fant, C.; Sott, K.; Elwing, H. *Anal. Chem.* **2001,** *73*, 5796-5804.

35.   Larsson, C.; Rodahl, M.; Höök, F. *Anal. Chem.* **2003,** *75*, 5080-5087.

36.   Reviakine, I.; Johannsmann, D.; Richter, R. P. *Anal. Chem.* **2011,** *83*, 8838-8848.

37.   Sauerbrey, G. *Z. Physik* **1959,** *155*, 206-222.

38.   Homola, J.; Yee, S. S.; Gauglitz, G. *Sensors and Actuators B-Chemical* **1999,** *54*, 3-15.

39.   Swann, M. J.; Peel, L. L.; Carrington, S.; Freeman, N. J. *Anal. Biochem.* **2004,** *329*, 190-198.

40.   Bingen, P.; Wang, G.; Steinmetz, N. F.; Rodahl, M.; Richter, R. P. *Anal. Chem.* **2008,** *80*, 8880-8890.

41.   Voinova, M. V.; Rodahl, M.; Jonson, M.; Kasemo, B. *Phys. Scr.* **1999,** *59*, 391.

42.   Watson, J. D.; Crick, F. H. C. *Nature* **1953,** *171*, 737-738.

43.   Watson, J. D.; Crick, F. H. C. *Nature* **1953,** *171*, 964-967.

44.   McGrath, C. L.; Katz, L. A. *Trends in Ecology & Evolution* **2004,** *19*, 32-38.

45.   Dickerson, R. E.; Drew, H. R. *J. Mol. Biol.* **1981,** *149*, 761-786.

46.   Wing, R.; Drew, H.; Takano, T.; Broka, C.; Tanaka, S.; Itakura, K.; Dickerson, R. E. *Nature* **1980,** *287*, 755-758.

47.   Wang, J. C. *Proc. Natl. Acad. Sci. U. S. A.* **1979,** *76*, 200-203.

48.   Stofer, E.; Lavery, R. *Biopolymers* **1994,** *34*, 337-346.

49.   Hagerman, P. J. *Biopolymers* **1981,** *20*, 1503-1535.

50.   Diekmann, S.; Hillen, W.; Morgeneyer, B.; Wells, R. D.; Porschke, D. *Biophys. Chem.* **1982,** *15*, 263-270.

51.   Tinland, B.; Pluen, A.; Sturm, J.; Weill, G. *Macromolecules* **1997,** *30*, 5763-5765.

52.   Kallenbach, N. R.; Ma, R. I.; Seeman, N. C. *Nature* **1983,** *305*, 829-831.

53.   Seeman, N. C. *J. Theor. Biol.* **1982,** *99*, 237-247.

54.   Seeman, N. C. *J. Biomol. Struct. Dyn.* **1985,** *3*, 11-34.

55.   Seeman, N. C. *Journal of Molecular Graphics* **1985,** *3*, 34-39.

56.   Seeman, N. C.; Kallenbach, N. R. *Biophys. J.* **1983,** *44*, 201-209.

57.   Modi, S.; Bhatia, D.; Simmel, F. C.; Krishnan, Y. *Journal of Physical Chemistry Letters* **2010,** *1*, 1994-2005.

58.   Pinheiro, A. V.; Han, D.; Shih, W. M.; Yan, H. *Nat. Nanotechnol.* **2011,** *6*, 763-772.

59.   Seeman, N. C. *Annu. Rev. Biophys. Biomol. Struct.* **1998,** *27*, 225-248.

60.   Seeman, N. C. *Trends Biotechnol.* **1999,** *17*, 437-443.

61.   Seeman, N. C. *Mol. Biotechnol.* **2007,** *37*, 246-257.

62.   Seeman, N. C. *Chem. Biol.* **2003,** *10*, 1151-1159.

63.   Gothelf, K. V.; LaBean, T. H. *Org. Biomol. Chem.* **2005,** *3*, 4023-4037.

64.   Holliday, R. *Genetical Research* **1964,** *5*, 282-&.

65.   Cohen, S. N.; Chang, A. C. Y.; Boyer, H. W.; Helling, R. B. *Proc. Natl. Acad. Sci. U. S. A.* **1973,** *70*, 3240-3244.
66.   LaBean, T. H.; Yan, H.; Kopatsch, J.; Liu, F. R.; Winfree, E.; Reif, J. H.; Seeman, N. C. *J. Am. Chem. Soc.* **2000,** *122*, 1848-1860.
67.   Li, X. J.; Yang, X. P.; Qi, J.; Seeman, N. C. *J. Am. Chem. Soc.* **1996,** *118*, 6131-6140.
68.   Fu, T. J.; Seeman, N. C. *Biochemistry* **1993,** *32*, 3211-3220.
69.   Sa-Ardyen, P.; Vologodskii, A. V.; Seeman, N. C. *Biophys. J.* **2003,** *84*, 3829-3837.
70.   Winfree, E.; Liu, F. R.; Wenzler, L. A.; Seeman, N. C. *Nature* **1998,** *394*, 539-544.
71.   Liu, F. R.; Sha, R. J.; Seeman, N. C. *J. Am. Chem. Soc.* **1999,** *121*, 917-922.
72.   Lu, M.; Guo, Q.; Seeman, N. C.; Kallenbach, N. R. *J. Mol. Biol.* **1991,** *221*, 1419-1432.
73.   Tumpane, J.; Sandin, P.; Kumar, R.; Powers, V. E. C.; Lundberg, E. P.; Gale, N.; Baglioni, P.; Lehn, J. M.; Albinsson, B.; Lincoln, P.; Wilhelmsson, L. M.; Brown, T.; Nordén, B. *Chem. Phys. Lett.* **2007,** *440*, 125-129.
74.   Sandin, P.; Lincoln, P.; Albinsson, B. *J. Phys. Chem. C* **2008,** *112*, 13089-13094.
75.   Aldaye, F. A.; Sleiman, H. F. *Angewandte Chemie-International Edition* **2006,** *45*, 2204-2209.
76.   Tumpane, J.; Kumar, R.; Lundberg, E. P.; Sandin, P.; Gale, N.; Nandhakumar, I. S.; Albinsson, B.; Lincoln, P.; Wilhelmsson, L. M.; Brown, T.; Nordén, B. *Nano Lett.* **2007,** *7*, 3832-3839.
77.   Lundberg, E. P.; El-Sagheer, A. H.; Kocalka, P.; Wilhelmsson, L. M.; Brown, T.; Norden, B. *Chem. Commun. (Cambridge, U. K.)* **2010,** *46*, 3714-3716.
78.   Lundberg, E. P.; Plesa, C.; Wilhelmsson, L. M.; Lincoln, P.; Brown, T.; Norden, B. *ACS Nano* **2011,** *5*, 7565-7575.
79.   Shih, W. M.; Quispe, J. D.; Joyce, G. F. *Nature* **2004,** *427*, 618-621.
80.   Rothemund, P. W. K. *Nature* **2006,** *440*, 297-302.
81.   Kim, D.-N.; Kilchherr, F.; Dietz, H.; Bathe, M. *Nucleic Acids Res.* **2012,** *40*, 2862-2868.
82.   Martin, T. G.; Dietz, H. *Nature Communications* **2012,** *3*.
83.   Andersen, E. S.; Dong, M.; Nielsen, M. M.; Jahn, K.; Subramani, R.; Mamdouh, W.; Golas, M. M.; Sander, B.; Stark, H.; Oliveira, C. L. P.; Pedersen, J. S.; Birkedal, V.; Besenbacher, F.; Gothelf, K. V.; Kjems, J. *Nature* **2009,** *459*, 73-U75.
84.   Douglas, S. M.; Dietz, H.; Liedl, T.; Hoegberg, B.; Graf, F.; Shih, W. M. *Nature* **2009,** *459*, 414-418.
85.   Ke, Y.; Douglas, S. M.; Liu, M.; Sharma, J.; Cheng, A.; Leung, A.; Liu, Y.; Shih, W. M.; Yan, H. *J. Am. Chem. Soc.* **2009,** *131*, 15903-15908.
86.   Dietz, H.; Douglas, S. M.; Shih, W. M. *Science* **2009,** *325*, 725-730.
87.   Han, D. R.; Pal, S.; Nangreave, J.; Deng, Z. T.; Liu, Y.; Yan, H. *Science* **2011,** *332*, 342-346.
88.   Yin, P.; Hariadi, R. F.; Sahu, S.; Choi, H. M. T.; Park, S. H.; LaBean, T. H.; Reif, J. H. *Science* **2008,** *321*, 824-826.
89.   Wei, B.; Dai, M.; Yin, P. *Nature* **2012,** *485*, 623-626.
90.   Ke, Y.; Ong, L. L.; Shih, W. M.; Yin, P. *Science* **2012,** *338*, 1177-1183.

91. Armitage, B. A., Cyanine dye-DNA interactions: Intercalation, groove binding, and aggregation. In *DNA Binders and Related Subjects*, Waring, M. J.; Chaires, J. B., Eds. 2005; Vol. 253, pp 55-76.

92. Carrondo, M.; Coll, M.; Aymami, J.; Wang, A. H. J.; Vandermarel, G. A.; Vanboom, J. H.; Rich, A. *Biochemistry* **1989,** *28*, 7849-7859.

93. Cosa, G.; Focsaneanu, K. S.; McLean, J. R. N.; McNamee, J. P.; Scaiano, J. C. *Photochem. Photobiol.* **2001,** *73*, 585-599.

94. Kapuscinski, J. *Biotechnic & Histochemistry* **1995,** *70*, 220-233.

95. Carlsson, C.; Larsson, A.; Jonsson, M.; Albinsson, B.; Norden, B. *J. Phys. Chem.* **1994,** *98*, 10313-10321.

96. Spielmann, H. P.; Wemmer, D. E.; Jacobsen, J. P. *Biochemistry* **1995,** *34*, 8542-8553.

97. Carlsson, C.; Jonsson, M.; Akerman, B. *Nucleic Acids Res.* **1995,** *23*, 2413-2420.

98. Rye, H. S.; Yue, S.; Wemmer, D. E.; Quesada, M. A.; Haugland, R. P.; Mathies, R. A.; Glazer, A. N. *Nucleic Acids Res.* **1992,** *20*, 2803-2812.

99. Larsson, A.; Carlsson, C.; Jonsson, M.; Albinsson, B. *J. Am. Chem. Soc.* **1994,** *116*, 8459-8465.

100. Petty, J. T.; Bordelon, J. A.; Robertson, M. E. *J. Phys. Chem. B* **2000,** *104*, 7221-7227.

101. Glazer, A. N.; Rye, H. S. *Nature* **1992,** *359*, 859-861.

102. Kershner, R. J.; Bozano, L. D.; Micheel, C. M.; Hung, A. M.; Fornof, A. R.; Cha, J. N.; Rettner, C. T.; Bersani, M.; Frommer, J.; Rothemund, P. W. K.; Wallraff, G. M. *Nat. Nanotechnol.* **2009,** *4*, 557-561.

103. Hung, A. M.; Micheel, C. M.; Bozano, L. D.; Osterbur, L. W.; Wallraff, G. M.; Cha, J. N. *Nat. Nanotechnol.* **2010,** *5*, 121-126.

104. Gao, B.; Sarveswaran, K.; Bernstein, G. H.; Lieberman, M. *Langmuir* **2010,** *26*, 12680-12683.

105. Penzo, E.; Wang, R. S.; Palma, M.; Wind, S. J. *Journal of Vacuum Science & Technology B* **2011,** *29*.

106. Peterlinz, K. A.; Georgiadis, R. M.; Herne, T. M.; Tarlov, M. J. *J. Am. Chem. Soc.* **1997,** *119*, 3401-3402.

107. Wong, E. L. S.; Chow, E.; Gooding, J. J. *Langmuir* **2005,** *21*, 6957-6965.

108. Herne, T. M.; Tarlov, M. J. *J. Am. Chem. Soc.* **1997,** *119*, 8916-8920.

109. Steel, A. B.; Herne, T. M.; Tarlov, M. J. *Anal. Chem.* **1998,** *70*, 4670-4677.

110. Hannestad, J. K.; Brune, R.; Czolkos, I.; Jesorka, A.; El-Sagheer, A. H.; Brown, T.; Albinsson, B.; Orwar, O. *ACS Nano* **2013,** *7*, 308-315.

111. Chan, Y. H. M.; Lenz, P.; Boxer, S. G. *Proc. Natl. Acad. Sci. U. S. A.* **2007,** *104*, 18913-18918.

112. Pfeiffer, I.; Höök, F. *J. Am. Chem. Soc.* **2004,** *126*, 10224-10225.

113. Börjesson, K.; Tumpane, J.; Ljungdahl, T.; Wilhelmsson, L. M.; Nordén, B.; Brown, T.; Mårtensson, J.; Albinsson, B. *J. Am. Chem. Soc.* **2009,** *131*, 2831-2839.

114. Börjesson, K.; Wiberg, J.; El-Sagheer, A. H.; Ljungdahl, T.; Mårtensson, J.; Brown, T.; Nordén, B.; Albinsson, B. *ACS Nano* **2010,** *4*, 5037-5046.

115. Israelachvili, J. N., *Intermolecular and Surface Forces*. 2 ed.; Academic Press: London, 1991.

116. Bhattacharya, S.; Biswas, J. *Langmuir* **2009,** *26*, 4642-4654.

117. Cremer, P. S.; Boxer, S. G. *J. Phys. Chem. B* **1999,** *103*, 2554-2559.

118. Hook, F.; Stengel, G.; Dahlin, A. B.; Gunnarsson, A.; Jonsson, M. P.; Jonsson, P.; Reimhult, E.; Simonsson, L.; Svedhem, S. *Biointerphases* **2008,** *3,* FA108-FA116.

119. Jass, J.; Tjärnhage, T.; Puu, G. *Biophys. J.* **2000,** *79,* 3153-3163.

120. Nissen, J.; Gritsch, S.; Wiegand, G.; Radler, J. O. *European Physical Journal B* **1999,** *10,* 335-344.

121. Reimhult, E.; Hook, F.; Kasemo, B. *Langmuir* **2002,** *19,* 1681-1691.

122. Reimhult, E.; Hook, F.; Kasemo, B. *Physical Review E* **2002,** *66,* 4.

123. Richter, R. P.; Berat, R.; Brisson, A. R. *Langmuir* **2006,** *22,* 3497-3505.

124. Sackmann, E. *Science* **1996,** *271,* 43-48.

125. Seantier, B.; Kasemo, B. *Langmuir* **2009,** *25,* 5767-5772.

126. Jass, J.; Tjarnhage, T.; Puu, G. *Biophys. J.* **2000,** *79,* 3153-3163.

127. Franz, V.; Loi, S.; Muller, H.; Bamberg, E.; Butt, H. H. *Colloids and Surfaces B-Biointerfaces* **2002,** *23,* 191-200.

128. Muller, D. J.; Engel, A. *Biophys. J.* **1997,** *73,* 1633-1644.

129. Zwang, T. J.; Fletcher, W. R.; Lane, T. J.; Johal, M. S. *Langmuir 26,* 4598-4601.

130. Koenig, B. W.; Kruger, S.; Orts, W. J.; Majkrzak, C. F.; Berk, N. F.; Silverton, J. V.; Gawrisch, K. *Langmuir* **1996,** *12,* 1343-1350.

131. Doshi, D. A.; Dattelbaum, A. M.; Watkins, E. B.; Brinker, C. J.; Swanson, B. I.; Shreve, A. P.; Parikh, A. N.; Majewski, J. *Langmuir* **2005,** *21,* 2865-2870.

132. Mabrey, S.; Sturtevant, J. M. *Proc. Natl. Acad. Sci. U. S. A.* **1976,** *73,* 3862-3866.

133. Pfeiffer, I.; Höök, F. *Anal. Chem.* **2006,** *78,* 7493-7498.

134. Simonsson, L.; Jonsson, P.; Stengel, G.; Höök, F. *ChemPhysChem* **2010,** *11,* 1011-1017.

135. Simonsson, L.; Kurczy, M. E.; Trouillon, R.; Hook, F.; Cans, A. S. *Scientific Reports* **2012,** *2.*

136. Stengel, G.; Simonsson, L.; Campbell, R. A.; Hook, F. *J. Phys. Chem. B* **2008,** *112,* 8264-8274.

137. Stengel, G.; Zahn, R.; Hook, F. *J. Am. Chem. Soc.* **2007,** *129,* 9584-+.

138. Bombelli, F. B.; Betti, F.; Gambinossi, F.; Caminati, G.; Brown, T.; Baglioni, P.; Berti, D. *Soft Matter* **2009,** *5,* 1639-1645.

139. Langecker, M.; Arnaut, V.; Martin, T. G.; List, J.; Renner, S.; Mayer, M.; Dietz, H.; Simmel, F. C. *Science* **2012,** *338,* 932-936.

140. Czogalla, A.; Petrov, E. P.; Kauert, D. J.; Uzunova, V.; Zhang, Y. X.; Seidel, R.; Schwille, P. *Faraday Discuss.* **2013,** *161,* 31-43.

141. Burns, J. R.; Gopfrich, K.; Wood, J. W.; Thacker, V. V.; Stulz, E.; Keyser, U. F.; Howorka, S. *Angewandte Chemie-International Edition* **2013,** *52,* 12069-12072.

142. Allen, J. P.; Feher, G.; Yeates, T. O.; Komiya, H.; Rees, D. C. *Proc. Natl. Acad. Sci. U. S. A.* **1987,** *84,* 5730-5734.

143. McDermott, G.; Prince, S. M.; Freer, A. A.; Hawthornthwaitelawless, A. M.; Papiz, M. Z.; Cogdell, R. J.; Isaacs, N. W. *Nature* **1995,** *374,* 517-521.

144. Koepke, J.; Hu, X. C.; Muenke, C.; Schulten, K.; Michel, H. *Structure* **1996,** *4,* 581-597.

145. McLuskey, K.; Prince, S. M.; Cogdell, R. J.; Isaacs, N. W. *Biochemistry* **2001,** *40,* 8783-8789.

146. Roszak, A. W.; Howard, T. D.; Southall, J.; Gardiner, A. T.; Law, C. J.; Isaacs, N. W.; Cogdell, R. J. *Science* **2003,** *302,* 1969-1972.

147. Fleming, G. R.; vanGrondelle, R. *Curr. Opin. Struct. Biol.* **1997,** *7,* 738-748.

148. Sundstrom, V.; Pullerits, T.; van Grondelle, R. *J. Phys. Chem. B* **1999,** *103*, 2327-2346.
149. Damjanovic, A.; Ritz, T.; Schulten, K. *Physical Review E* **1999,** *59*, 3293-3311.
150. Hu, X. C.; Damjanovic, A.; Ritz, T.; Schulten, K. *Proc. Natl. Acad. Sci. U. S. A.* **1998,** *95*, 5935-5941.
151. Hu, X. C.; Ritz, T.; Damjanovic, A.; Autenrieth, F.; Schulten, K. *Q. Rev. Biophys.* **2002,** *35*, 1-62.
152. Hu, X. C.; Ritz, T.; Damjanovic, A.; Schulten, K. *J. Phys. Chem. B* **1997,** *101*, 3854-3871.
153. Hu, X. C.; Schulten, K. *Physics Today* **1997,** *50*, 28-34.
154. Law, C. J.; Gardiner, A. T.; Southall, J.; Roszak, A. W.; Howard, T. D.; Isaacs, N. W.; Cogdell, R. J., How Purple Bacteria Harvest Light Energy. In *Energy Harvesting Materials*, Andrews, D. L., Ed. World Scientific Publishing & Co. Pte. Ltd.: Singapore, 2005; pp 65-95.
155. Aagaard, J.; Sistrom, W. R. *Photochem. Photobiol.* **1972,** *15*, 209-&.
156. Cogdell, R. J.; Durant, I.; Valentine, J.; Lindsay, J. G.; Schmidt, K. *Biochim. Biophys. Acta* **1983,** *722*, 427-435.
157. Stadtwalddemchick, R.; Turner, F. R.; Gest, H. *FEMS Microbiol. Lett.* **1990,** *71*, 117-121.
158. Halloren, E.; McDermott, G.; Lindsay, J. G.; Miller, C.; Freer, A. A.; Isaacs, N. W.; Cogdell, R. J. *Photosynth. Res.* **1995,** *44*, 149-155.
159. Clayton, R. K.; Clayton, B. J. *Proceedings of the National Academy of Sciences of the United States of America-Biological Sciences* **1981,** *78*, 5583-5587.
160. Bopp, M. A.; Jia, Y. W.; Li, L. Q.; Cogdell, R. J.; Hochstrasser, R. M. *Proc. Natl. Acad. Sci. U. S. A.* **1997,** *94*, 10630-10635.
161. Hu, X. C.; Damjanovic, A.; Ritz, T.; Schulten, K. *Proc. Natl. Acad. Sci. U. S. A.* **1998,** *95*, 5935-5941.
162. Blankenship, R. E. *Trends Plant Sci.* **2001,** *6*, 4-6.
163. Xiong, J.; Fischer, W. M.; Inoue, K.; Nakahara, M.; Bauer, C. E. *Science* **2000,** *289*, 1724-1730.
164. Ben-Shem, A.; Frolow, F.; Nelson, N. *Nature* **2003,** *426*, 630-635.
165. Jordan, P.; Fromme, P.; Witt, H. T.; Klukas, O.; Saenger, W.; Krauss, N. *Nature* **2001,** *411*, 909-917.
166. Sener, M. K.; Lu, D. Y.; Ritz, T.; Park, S.; Fromme, P.; Schulten, K. *J. Phys. Chem. B* **2002,** *106*, 7948-7960.
167. Yang, M.; Damjanovic, A.; Vaswani, H. M.; Fleming, G. R. *Biophys. J.* **2003,** *85*, 140-158.
168. Gust, D.; Moore, T. A.; Moore, A. L. *Acc. Chem. Res.* **2001,** *34*, 40-48.
169. Gust, D.; Moore, T. A.; Moore, A. L. *Acc. Chem. Res.* **1993,** *26*, 198-205.
170. Kuciauskas, D.; Liddell, P. A.; Lin, S.; Johnson, T. E.; Weghorn, S. J.; Lindsey, J. S.; Moore, A. L.; Moore, T. A.; Gust, D. *J. Am. Chem. Soc.* **1999,** *121*, 8604-8614.
171. Moore, T. A.; Gust, D.; Mathis, P.; Mialocq, J. C.; Chachaty, C.; Bensasson, R. V.; Land, E. J.; Doizi, D.; Liddell, P. A.; Lehman, W. R.; Nemeth, G. A.; Moore, A. L. *Nature* **1984,** *307*, 630-632.
172. Steinberg-Yfrach, G.; Liddell, P. A.; Hung, S. C.; Moore, A. L.; Gust, D.; Moore, T. A. *Nature* **1997,** *385*, 239-241.
173. Van Patten, P. G.; Shreve, A. P.; Lindsey, J. S.; Donohoe, R. J. *J. Phys. Chem. B* **1998,** *102*, 4209-4216.

174. Kim, D.; Osuka, A. *J. Phys. Chem. A* **2003,** *107*, 8791-8816.
175. Wagner, R. W.; Lindsey, J. S. *J. Am. Chem. Soc.* **1994,** *116*, 9759-9760.
176. Adronov, A.; Frechet, J. M. J. *Chem. Commun.* **2000**, 1701-1710.
177. Balzani, V.; Ceroni, P.; Juris, A.; Venturi, M.; Campagna, S.; Puntoriero, F.; Serroni, S. *Coord. Chem. Rev.* **2001,** *219*, 545-572.
178. Brousmiche, D. W.; Serin, J. M.; Frechet, J. M. J.; He, G. S.; Lin, T. C.; Chung, S. J.; Prasad, P. N.; Kannan, R.; Tan, L. S. *J. Phys. Chem. B* **2004,** *108*, 8592-8600.
179. Kawa, M.; Frechet, J. M. J. *Chem. Mater.* **1998,** *10*, 286-296.
180. Wasielewski, M. R. *Chem. Rev. (Washington, DC, U. S.)* **1992,** *92*, 435-461.
181. Wasielewski, M. R. *J. Org. Chem.* **2006,** *71*, 5051-5066.
182. Katterle, M.; Prokhorenko, V. I.; Holzwarth, A. R.; Jesorka, A. *Chem. Phys. Lett.* **2007,** *447*, 284-288.
183. Nam, Y. S.; Shin, T.; Park, H.; Magyar, A. P.; Choi, K.; Fantner, G.; Nelson, K. A.; Belcher, A. M. *J. Am. Chem. Soc.* **2010,** *132*, 1462-+.
184. Miller, R. A.; Presley, A. D.; Francis, M. B. *J. Am. Chem. Soc.* **2007,** *129*, 3104-3109.
185. Albinsson, B.; Hannestad, J. K.; Börjesson, K. *Coord. Chem. Rev.* **2012,** *256*, 2399-2413.
186. Teo, Y. N.; Kool, E. T. *Chem. Rev. (Washington, DC, U. S.)* **2012,** *112*, 4221-4245.
187. Spillmann, C. M.; Ancona, M. G.; Buckhout-White, S.; Algar, W. R.; Stewart, M. H.; Susumu, K.; Huston, A. L.; Goldman, E. R.; Medintz, I. L. *ACS Nano* **2013,** *7*, 7101-7118.
188. Boeneman, K.; Prasuhn, D. E.; Blanco-Canosa, J. B.; Dawson, P. E.; Melinger, J. S.; Ancona, M.; Stewart, M. H.; Susumu, K.; Huston, A.; Medintz, I. L. *J. Am. Chem. Soc.* **2010,** *132*, 18177-18190.
189. Su, W.; Schuster, M.; Bagshaw, C. R.; Rant, U.; Burley, G. A. *Angewandte Chemie-International Edition* **2011,** *50*, 2712-2715.
190. Su, W.; Bonnard, V.; Burley, G. A. *Chemistry-a European Journal* **2011,** *17*, 7982-7991.
191. Garo, F.; Häner, R. *Angew. Chem. Int. Ed.* **2012,** *51*, 916-919.
192. Brun, A. M.; Harriman, A. *J. Am. Chem. Soc.* **1994,** *116*, 10383-10393.
193. Stein, I. H.; Steinhauer, C.; Tinnefeld, P. *J. Am. Chem. Soc.* **2011,** *133*, 4193-4195.
194. Hannestad, J. K.; Gerrard, S. R.; Brown, T.; Albinsson, B. *Small* **2011,** *7*, 3178-3185.
195. Benvin, A. L.; Creeger, Y.; Fisher, G. W.; Ballou, B.; Waggoner, A. S.; Armitage, B. A. *J. Am. Chem. Soc.* **2007,** *129*, 2025-2034.
196. Özhalıcı-Ünal, H.; Armitage, B. A. *ACS Nano* **2009,** *3*, 425-433.
197. Dutta, P. K.; Varghese, R.; Nangreave, J.; Lin, S.; Yan, H.; Liu, Y. *J. Am. Chem. Soc.* **2011,** *133*, 11985-11993.
198. Chandran, R. S.; John, S. E.; Amit, M. *The Journal of Chemical Physics* **2005,** *123*, 224708.
199. Tabner, B. J.; Yandle, J. R. *J. Chem. Soc.* **1968**, 381-388.
200. Nakagawa, M.; Rikukawa, M.; Watanabe, M.; Sanui, K.; Ogata, N. *Bull. Chem. Soc. Jpn.* **1997,** *70*, 737-744.
201. Jing, Y.; Trefna, H.; Persson, M.; Kasemo, B.; Svedhem, S. *Soft Matter* **2014,** *10*, 187-195.

202. Jonsson, P.; Beech, J. P.; Tegenfeldt, J. O.; Hook, F. *J. Am. Chem. Soc.* **2009,** *131*, 5294-5297.
203. Jonsson, P.; Jonsson, M. P.; Hook, F. *Nano Lett.* **2010,** *10*, 1900-1906.
204. Ke, Y.; Bellot, G.; Voigt, N. V.; Fradkov, E.; Shih, W. M. *Chemical Science* **2012,** *3*, 2587-2597.